

Directed self-assembly of oligo(dimethylsiloxane) liquid crystals for sub-5 nm patterning

Citation for published version (APA):

Nickmans, K. (2017). *Directed self-assembly of oligo(dimethylsiloxane) liquid crystals for sub-5 nm patterning*. [Phd Thesis 1 (Research TU/e / Graduation TU/e), Chemical Engineering and Chemistry]. Technische Universiteit Eindhoven.

Document status and date:

Published: 30/10/2017

Document Version:

Publisher's PDF, also known as Version of Record (includes final page, issue and volume numbers)

Please check the document version of this publication:

- A submitted manuscript is the version of the article upon submission and before peer-review. There can be important differences between the submitted version and the official published version of record. People interested in the research are advised to contact the author for the final version of the publication, or visit the DOI to the publisher's website.
- The final author version and the galley proof are versions of the publication after peer review.
- The final published version features the final layout of the paper including the volume, issue and page numbers.

[Link to publication](#)

General rights

Copyright and moral rights for the publications made accessible in the public portal are retained by the authors and/or other copyright owners and it is a condition of accessing publications that users recognise and abide by the legal requirements associated with these rights.

- Users may download and print one copy of any publication from the public portal for the purpose of private study or research.
- You may not further distribute the material or use it for any profit-making activity or commercial gain
- You may freely distribute the URL identifying the publication in the public portal.

If the publication is distributed under the terms of Article 25fa of the Dutch Copyright Act, indicated by the "Taverne" license above, please follow below link for the End User Agreement:

www.tue.nl/taverne

Take down policy

If you believe that this document breaches copyright please contact us at:

openaccess@tue.nl

providing details and we will investigate your claim.

Directed Self-Assembly of Oligo(dimethylsiloxane) Liquid Crystals for Sub-5 nm Patterning

PROEFSCHRIFT

ter verkrijging van de graad van doctor aan de Technische Universiteit Eindhoven, op gezag van de rector magnificus prof.dr.ir. F.P.T. Baaijens, voor een commissie aangewezen door het College voor Promoties, in het openbaar te verdedigen op maandag 30 oktober 2017 om 16:00 uur

door

Koen Nickmans

geboren te Bonheiden, België

Dit proefschrift is goedgekeurd door de promotoren en de samenstelling van de promotiecommissie is als volgt:

voorzitter:	prof.dr.ir. R.A.J. Janssen
1 ^e promotor:	prof.dr. A.P.H.J. Schenning
2 ^e promotor:	prof.dr. D.J. Broer
leden:	dr. C. Sánchez Somolinos (ICMA)
	prof.dr.ir. J. Huskens (Universiteit Twente)
	prof.dr. E.W. Meijer
adviseurs:	dr. S.F. Wuister (ASML)
	dr. R. Gronheid (KLA-Tencor)

Het onderzoek of ontwerp dat in dit proefschrift wordt beschreven is uitgevoerd in overeenstemming met de TU/e Gedragscode Wetenschapsbeoefening.

“Good judgement comes from experience, experience comes from bad judgement”

Lord Karan Bilimoria
Founder & CEO of Cobra Beer

A catalogue record is available from the Eindhoven University of Technology Library

ISBN: 978-94-92679-16-1

This research was made possible by a grant of Technology Foundation STW

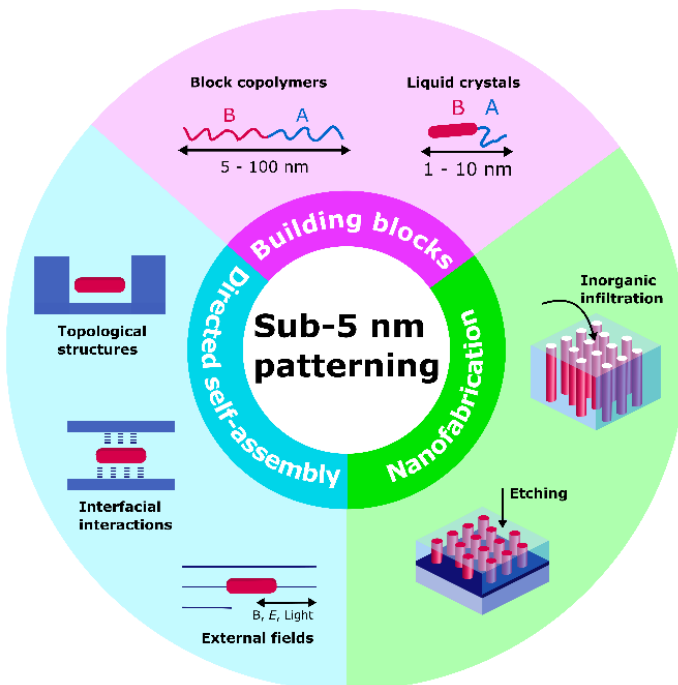
Table of Contents

Chapter 1	Introduction	1
Chapter 2	Thin film directed self-assembly of columnar oligo(dimethylsiloxane) liquid crystals	33
Chapter 3	Smectic oligo(dimethylsiloxane) liquid crystal for sub-5 nm patterning	51
Chapter 4	Three-dimensional orientational control in self-assembled thin films with sub-5 nm features by light	61
Chapter 5	Reactive oligo(dimethylsiloxane) mesogens and their micropatterned nanostructured thin films	85
Chapter 6	Vertically aligned, hybrid organic/inorganic sub-5 nm structured thin films by hydrogen bonded oligo(dimethylsiloxane) liquid crystals and polymers	101
Chapter 7	Epilogue	125
Summary		137
Acknowledgements		141
Curriculum Vitae		143

Chapter 1

Introduction

Abstract. The thin film directed self-assembly of molecular building blocks into oriented nanostructure arrays will enable next-generation nanomaterials for organic electronics, nanoporous membranes, and ultra-fine nanolithography. A collective research effort is being undertaken by chemists, physicists, material scientists, and engineers alike; from the design of individual molecules to access increasingly dense features, to their directed self-assembly into highly organized periodic nanoarrays, and importantly, the application of the nanostructures for device fabrication. Here we highlight recent progress towards functional thin film nanostructures at the sub-5 nm length scale and outline the steps made in this thesis towards the “directed self-assembly of oligo(dimethylsiloxane) liquid crystals for sub-5 nm patterning.”



This chapter is based on:

K. Nickmans, A. P. H. J. Schenning, *Adv. Mater* (accepted)

1.1. General introduction

The last half-century has witnessed a systematic exponential increase in the density of transistors on integrated circuits. This trend, commonly referred to as “Moore’s law”,^[1] has enabled the onset of personal computers and the advent of today’s powerful mobile devices (Figure 1). With the onset of human-level artificial intelligence, a data-driven society, and the internet-of-things, the hunger for further scaling beyond the current state of the art remains insatiable.

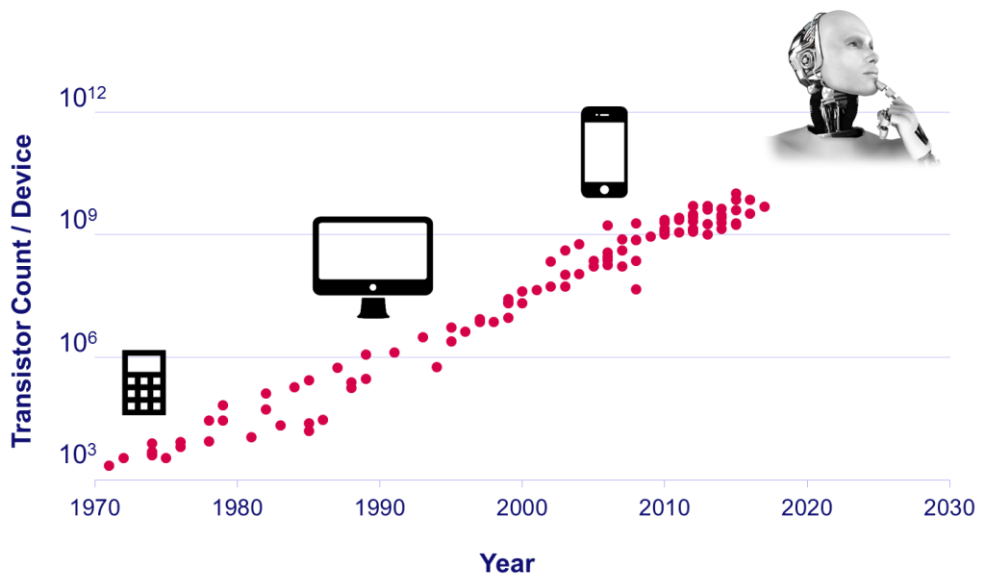


Figure 1. Graphical representation of exponential scaling of transistor count per device over time according to Moore’s law. Data obtained from [2].

Photolithography has been the prevalent patterning method applied by the semiconductor industry. In this process, a stack consisting of a substrate, oxide, and photoresist is exposed to a specific wavelength of UV light through a mask (Figure 2). The latent image in the resist is then developed, for example by rinsing in an appropriate solvent, and etched for transfer of the pattern into the underlying substrate. To create a circuit, these basic steps are repeated multiple times in a layered manner. Each new pattern printed on the wafer is aligned above the previous patterns to systematically build up the final device, which consists of conductors, insulators, and selectively doped regions. In this way, complex structures such as

transistors and the many wires connecting the transistors to make a circuit can be created.

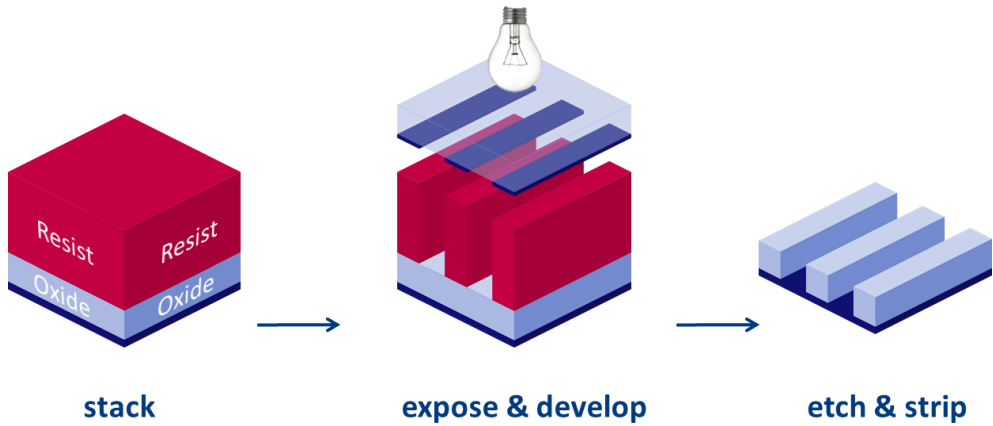


Figure 2. General scheme of pattern creation by photolithography.

Traditionally, advances in photolithography have been the driver behind the ability to print increasingly smaller features at a lower cost. According to the Rayleigh criterion, the smallest feature that can be patterned with acceptable control, i.e. the resolution, is proportional to the wavelength of the light used for imaging (λ), and inversely proportional to the numerical aperture (NA) of the projection lens. Over time, there has been a continuous shift to shorter wavelengths, from visible wavelengths (436 nm), to UV (365 nm), and deep-UV (248 nm & 193 nm). At the same time, the NA has increased dramatically by placing a liquid medium in the air gap between the lens and the wafer. Today, using a 193 nm immersion tool, minimum feature sizes have shrunk down to approximately 36 nm^[3] (Figure 3). In order to facilitate the production of even smaller features, extreme-UV (EUV) lithography, utilizing radiation of wavelength 13.5 nm, is currently being pursued on a global scale, even though it is tremendously complex and expensive.^[4,5]

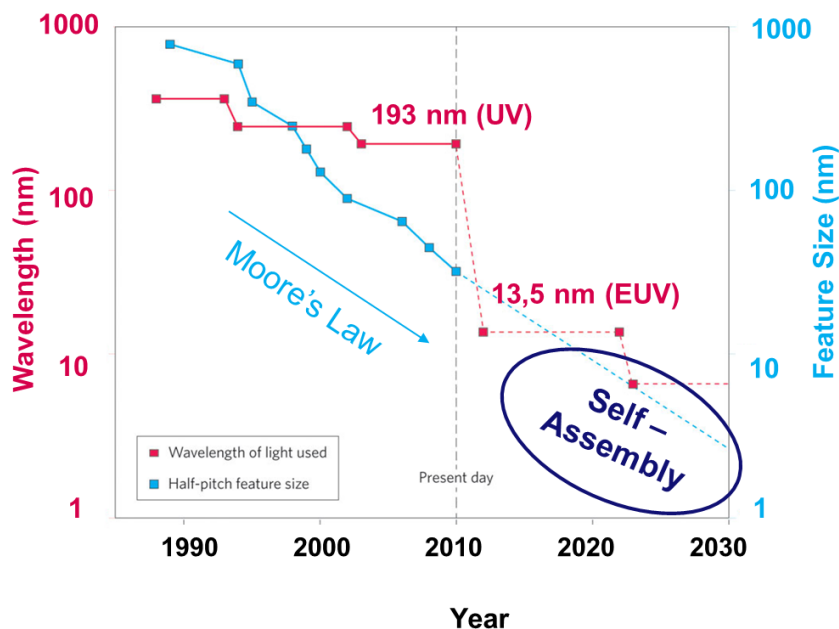


Figure 3. Adapted with permission from [4]. Copyright 2010, Nature Publishing Group

Considering the rising cost of optical lithography tools, alternative patterning technologies must be considered to enable the manufacturing of next generation integrated circuits. Electron beam lithography (EBL), which involves scanning a beam of electrons in a controlled fashion across a resist, is not constrained by the optical diffraction limit. Unfortunately, it is considered prohibitively slow and expensive. Nanoimprint technology (NIL) is a contact rather than a projection-based technology in which features are replicated directly onto surfaces using a stamp process. However, the economical creation of an imprint template remains a challenge, in addition to concerns associated with the physical contact process such as alignment and contamination.^[6]

The length scales attainable by top-down lithography are approaching that of bottom-up self-assembly found in polymers and small molecules (Figure 3). For this reason, bottom-up patterning technologies based on self-assembly are becoming increasingly attractive.^[7-11] The utilization of organic building blocks as self-assembled etch masks is particularly attractive since the lithographic information is contained in the self-assembling material itself, rather than provided in an exposure step.

The International Technology Roadmap for Semiconductors (ITRS) has identified the directed self-assembly (DSA) of block copolymers (BCPs) as a candidate for next generation nanopatterning. BCPs form nanostructures through microphase separation of incompatible blocks. Depending on the relative volume fractions of the blocks (f_A), lamellae, gyroid networks, hexagonally packed cylinders, and spheres can be obtained (Figure 4). The periodicity of the features is typically in the 10-100 nm regime.

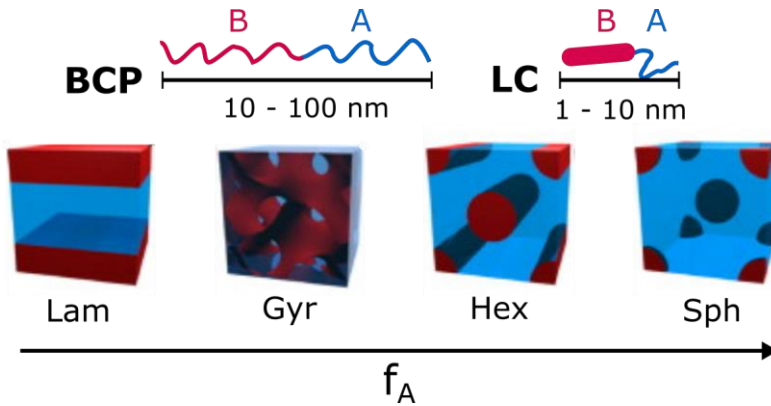


Figure 4. Mesophase morphologies formed by diblock copolymers and rod-coil liquid crystalline (LC) molecules. Abbreviations: Lam = lamellae, Gyr = bicontinuous gyroid, Hex = hexagonally packed cylinders, Sph = spheres. 3D renders reproduced from ^[12], Copyright 2007, Elsevier Ltd.

In block copolymer DSA, the morphologies are guided in thin films using top-down processes, resulting in a regular and oriented nanostructure array^[11,13,14] (Figure 5). DSA is typically achieved using topological^[13] or chemical^[14] guiding patterns, known as graphoepitaxy and chemoepitaxy, respectively. The major advantage of DSA techniques involving patterned surfaces, is that they allow the generation of addressable features (i.e. the circuit elements) by precisely placing the nanostructures across the wafer. Figure 5 depicts the process of graphoepitaxy. In this process, a BCP thin film is deposited on a wafer inside topological guiding channels of predetermined width and position. When the width of the channels corresponds to a discrete multiple of the BCP lattice spacing, oriented features are obtained at a multiple of the original spacing, otherwise known as a density multiplication. Other alignment techniques, such as solvent annealing,^[15,16] electric fields,^[17] and magnetic fields,^[18] have also been applied. In recent years, BCP DSA has emerged as a well-developed field, as exemplified by the appearance of numerous recent review articles.^[10-12,19,20]

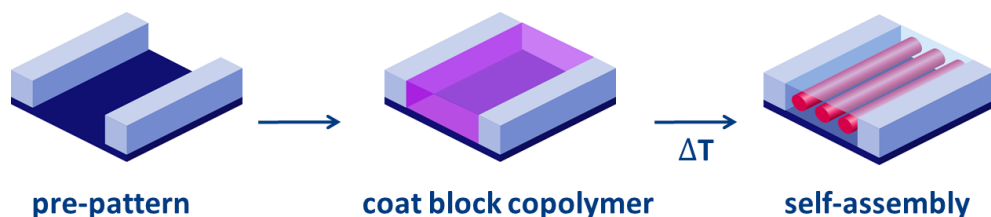


Figure 5. General scheme of pattern creation by directed self-assembly.

In order to fabricate circuit components such as inorganic nanowires^[21,22] or nanodots,^[7] a BCP pattern must be confined in a monolayer and aligned (Figure 5). Subsequently the layer is used as an etch mask to convert the organic pattern into an inorganic one. For pattern transfer, ‘wet’ and ‘dry’ processes have been applied. In the wet approach, one of the BCP blocks is degraded and removed by rinsing in a selective solvent.^[14,23,24] In contrast to wet etching processes, ‘dry’ plasma etching makes use of reactive gaseous species or physical ion bombardment to degrade polymers into volatile segments. The etch contrast arises from the difference in etch rates between constituent blocks to an appropriate plasma treatment, and the key to obtaining a high etching contrast is the incorporation of inorganic components into one of the blocks. There are two methods to achieving this. The first method consists of selectively incorporating inorganic material after assembly. Different approaches have been reported on the selective infiltration and controlled deposition of inorganic materials into neat self-assembled BCP films.^[25] The second method relies on the use of hybrid organic inorganic building blocks with inherent etch contrast. These materials are of particular interest since they can yield patterned inorganic nanostructures in a single etching step.^[19,26,27] Among hybrid organic-inorganic BCPs, poly(styrene)-*b*-poly(dimethylsiloxane) (PS-*b*-PDMS), is the most widely investigated.^[15,28-33] For example, Ross and coworkers demonstrated the fabrication of nanowires using a cylinder-forming PS-*b*-PDMS template. A monolayer of planar PDMS cylinders in a PS matrix was deposited within topological guiding features to provide a uniaxial planar alignment. In a subsequent plasma etching process, the PS domains were degraded while the PDMS domains were oxidized, resulting in an array of parallel lines of oxidized PDMS with a feature size of 8 nm (Figure 6a). By sputtering tungsten onto the oxidized PDMS template, and subsequently removing the oxidized PDMS, a nanostructured tungsten array of 9 nm features was fabricated with the reverse image (Figure 6b). Since this process is applicable to other metals including titanium, platinum, tantalum, cobalt, and nickel,^[34] these PDMS based materials are excellent materials for device fabrication.

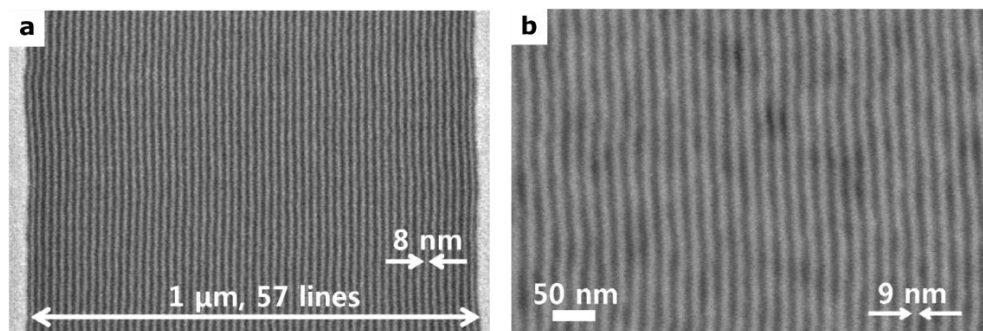


Figure 6. a) SEM image of an oxidized PS-b-PDMS array in topological guiding channel of 1 μm . b) Tungsten nanowires with 9 nm line width prepared using the PS-b-PDMS template. Reproduced with permission.^[30] Copyright 2010, American Chemical Society.

According to the ITRS, there are several issues currently preventing the integration of DSA with microelectronics fabrication processes. The first is related to concerns regarding the extendibility of the DSA process to smaller feature sizes. For BCPs, the characteristic dimensions are controlled by the molecular weight of the polymer. The inverse relationship between molecular weight and the Flory–Huggins interaction parameter (χ) required for self-assembly places a lower limit of approximately 10 nm on the minimum periodicity that can be realized through typical BCP self-assembly.^[10] Second, an immediate challenge for DSA is to show low enough levels of defects for manufacturing use ($< 0.01 \text{ cm}^2$). In contrast to top-down fabrication methods, soft organic building blocks have the tendency to form arbitrarily oriented poly-domain structures when left unguided, prohibiting their use in the fabrication of addressable media. To date, work has been published showing defect levels for pilot line processes ($< 100 \text{ cm}^2$),^[35,36] but defect levels are not yet low enough for manufacturing.

The use of patterning materials consisting of liquid crystalline (LC) small molecules could address both of the aforementioned challenges, which caused it to recently attract attention of the scientific community.^[37–39] LC phases are formed by rod-coil molecules and are driven by a combination of molecular shape and noncovalent interactions.^[40–43] Similar morphologies to BCPs, but with significantly smaller characteristic dimensions, can be achieved with these materials (Figure 4). Most well-known for their use in the display industry,^[44] LC materials are now finding applications as functional nanostructured materials^[45–47] for lab-on-a-chip systems,^[48] responsive coatings,^[49] actuators,^[50] nanoporous membranes,^[51–55] templated synthesis,^[56,57] organic semiconductors,^[58,59] and photovoltaic devices.^[60–62] In addition to self-assembly at smaller length scales, LCs are highly

customizable with regard to morphology and chemical functionality. Moreover, due to their low molecular weight, LCs show a fast response to stimuli,^[63] and a straightforward alignment over device length scales.^[64] Importantly, the “soft” nature of LCs makes them amenable to DSA processes involving (1) tailored interfacial interactions, (2) topologically structured interfaces, and (3) external fields (Figure 7).

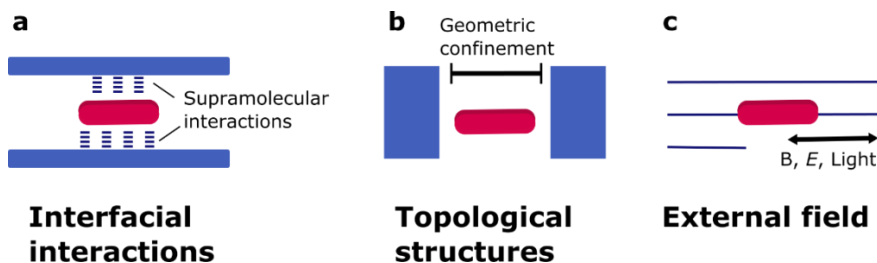


Figure 7. Schematic representation of directed self-assembly of LC small molecules, involving a) tailored interfacial interactions, b) topologically structured interfaces, and c) external fields.

In this chapter, we discuss recent progress, opportunities, and challenges in the field of sub-5 nm patterning using small molecules as building blocks. First, different strategies in the preparation of organic building blocks which form sub-5 nm patterns are discussed. Next, alignment techniques are highlighted which have contributed significantly towards the directed self-assembly of LC patterns. Examples are chosen from fields of organic electronics and nanoporous membranes, and their implications for nanolithography are discussed. Finally, suitable fabrication techniques for the conversion of organic sub-5nm patterns into inorganic nanostructured arrays are considered.

1.2. Organic building blocks for sub-5 nm patterning

1.2.1. Limits of high- χ block copolymers

While reservations were expressed in the introduction regarding the feature size limitations of typical block copolymer self-assembly,^[10] novel BCPs with high interactions parameters are emerging that offer self-assembly beyond the current scaling barriers, i.e. the sub-10 nm regime.^[39,65,66] So-called “high- χ ” BCPs with highly incompatible blocks typically consist of highly immiscible components, such as inorganic and organic segments.^[24,27,66–69] In principle, a large supramolecular toolbox is available to augment the block incompatibility through orthogonal non-

covalent interactions that enhance phase separation.^[70] For example, BCPs can be doped with small molecules which interact selectively with one of the domains via hydrogen bonding,^[71–76] or ionic interactions.^[9] Self-attractive non-covalent interactions may also be engineered directly into the polymer blocks, which omits the use of additives. For example, ABC triblock polymers have been synthesized in which two of the blocks (eg. A and B) interact favorably through π - π stacking^[77] or hydrogen bonding,^[78] resulting in a single nanodomain. The second domain is formed by the remaining non-interacting block (eg. C). Shape anisotropy, for example through the incorporation of rod-like carbohydrate blocks, is another powerful means to access ultra-dense BCP nanopatterns.^[67,79]

Through the development of high- χ BCPs, it is estimated that features as small as 2 nm can be obtained.^[39] At this length scale, the borderlines between polymers and small molecules are convoluted. The molecules can no longer be considered BCPs,^[39] but rather co-oligomers, the properties of which more closely resemble small molecules such as low molecular weight lyotropic ^[80,81] or thermotropic liquid crystals.^[82,83]

1.2.2. Small molecule self-assembly

Further lowering the molar mass of the soft building block brings one into the field of small molecule self-assembly, where the intrinsic length scale is the molecular length, between 2 - 10 nm. Remarkably, the phase behavior of lyotropic and thermotropic liquid crystals is similar to that of AB diblock BCPs (Figure 4, Figure 8), albeit at a smaller length scale. Amphiphilic molecules ^[37,84] spontaneously form lyotropic liquid crystalline phases of varying geometry depending on the solvent concentration. It is noteworthy that only dense lyotropic phases, ^[37] in which limited amounts of solvent are present, provide the necessary morphologies for long range nanostructured materials (lamellae, cylinders). Molecules based on a rigid-flexible motif ^[41–43] form thermotropic LC phases in bulk. In thermotropic phases, the distinct molecular shape in combination with supramolecular interactions such as electrostatic interactions, π - π stacking, and hydrogen bonding, results in thermodynamically stable structures.^[44] In contrast to BCPs, phase separation is no longer a prerequisite. The degree of order varies; from nematic phases with orientational order only, to higher order phases in which the periodicity of the nanopattern is approximate to the molecular length.^[85] The nematic phase does not provide the necessary bulk morphologies for nanolithography.

Rod-like molecules (calamitics), classically consisting of an aromatic core and a flexible tail, have the tendency to form lamellar structures (smectic mesophases, Sm). However, bicontinuous gyroidal, columnar, cubic, and other three-dimensionally ordered phases can be obtained by successively increasing the volume fraction of the alkyl chains in calamitics,^[40,41,86,87] similar to varying the relative volume fractions in a diblock BCP (Figure 4). Disc-like molecules (discotics) tend to stack perpendicular to the disc plane, generally resulting in columnar structures (columnar mesophases, Col). Discotic compounds are also known to exhibit lamellar and cubic phases.^[43]

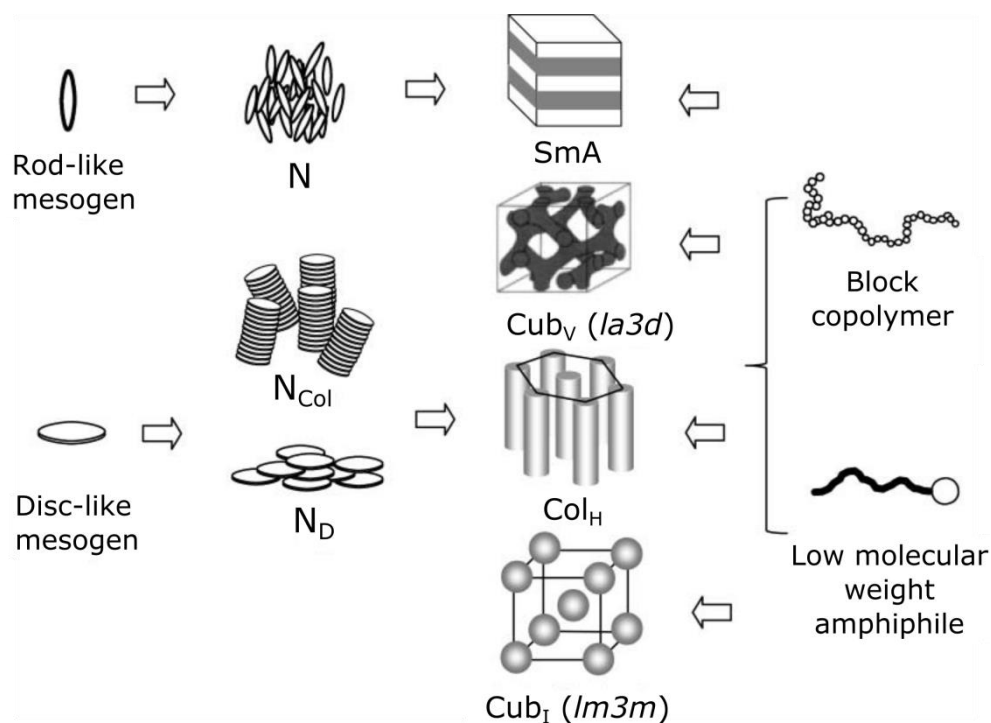


Figure 8. Mesophase morphologies formed by the self-assembly of rod-like and disc-like molecules, low molecular weight amphiphiles, and AB diblock copolymers. Abbreviations: N = nematic mesophase formed by rod-like molecules (N), disc-like molecules (N_D) or columnar aggregates (N_{Col}), SmA = smectic A phase, Cub_V = bicontinuous cubic phase, Col_H = hexagonal columnar mesophase and Cub_I = discontinuous (micellar) cubic mesophase. Reproduced with permission from ^[40]. Copyright 2001, Royal Society of Chemistry.

A distinct feature of LCs compared to BCPs is that their molecular shape can lead to molecular order within the lamellar or columnar structures. Many subtypes of Sm and Col phases have been allocated depending on the lattice and degree of

positional and orientational order of the molecules. Figure 8 represents the most simple Sm phase in which the rod-like molecules are on average perpendicular to the lamellar structures (SmA), and the most simple Col phase (Col_{hex}) in which the disc-like molecules are on average perpendicular to the columnar structure and the columns are packed in a hexagonal lattice. Higher order phases that include more complex 2D lattices (eg. Col_{rec}, Col_{squ}, Col_{obl}), and well-defined molecular tilt and spatial organization (eg. SmC, SmB, SmE) can be achieved through specific molecular design. Such complex phase morphologies are unobtainable by amorphous BCP self-assembly,^[40,41] and they may offer both improved design flexibility and an improved pattern fidelity from a nanopatterning perspective.

1.2.3. Small molecules based on hybrid organic/inorganic motifs

Owing to their small feature size and ease of alignment, small molecules make excellent candidates for the extension of BCP DSA processes to enable sub-5 nm patterning, provided they bear the necessary etching contrast. Since hybrid organic/inorganic small molecules with high etch contrast have emerged only very recently, an overview is provided below.

1.2.3.1. Polyhedral oligomeric silsesquioxanes (POSS)

Polyhedral oligomeric silsesquioxane (POSS) is a popular building block for the preparation of hybrid organic/inorganic small molecules. POSS consists of a 3-dimensional crystalline silicon-oxygen cage with the formula (RSiO_{3/2})_n. The cubic POSS cage has a size of 0.53 nm, and there are 8 available vertices on which to place substituents. Wang *et. al.* obtained hybrid organic/inorganic layered structures by mono-substituting a POSS cage with a varying number and length of alkyl tails (Figure 9a).^[88,89] These materials showed various crystal-crystal and crystal-isotropic phase transitions, and formed crystalline structures at room temperature. By varying the amount of alkyl tails and their lengths, lamellar structures were obtained in the range of 3.4 – 5.3 nm, as shown by XRD (Figure 9b). Long range order was promoted by slowly decreasing the temperature from the isotropic state to 30 °C at the rate of 0.1 °C min⁻¹. Under these thermal annealing conditions, long-range ordered lamellar structures with sharp boundaries were observed (Figure 9c). The length of this long-range ordered structure formed within a single grain was around 200 nm.^[88] Unfortunately, the crystalline nature of the reported phases will make the application of DSA processes extremely challenging, for the tendency of crystalline materials to nucleate and grow in into arbitrarily oriented domains. In order to grow single crystal films in an epitaxial process, the substrate would require the same crystal structure

as the layer and a close match of lattice parameters. [90] For this reason, smectic and discotic LC phases would be preferred for their mobility in combination with their high order.

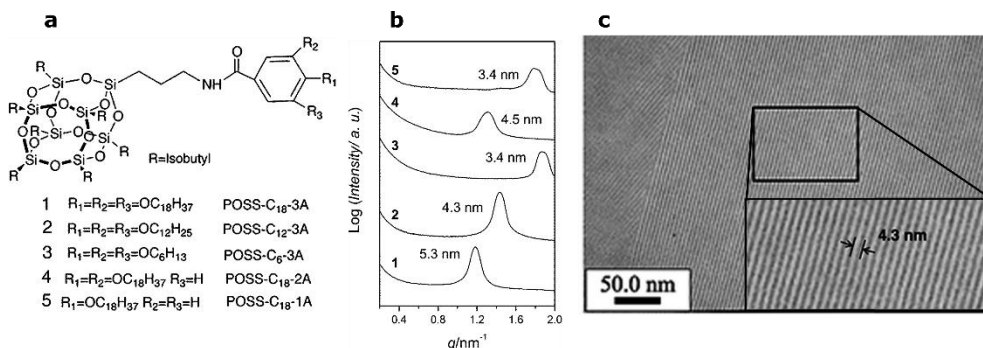


Figure 9. a) Chemical structures of alkylated POSS derivatives (1-5). b) XRD profiles showing first order d -spacings. c) TEM image of a thermally annealed sample (2). Reproduced with permission. [89] Copyright 2014, Royal Society of Chemistry.

Various LC phases utilizing POSS cages have been obtained by attaching different mesogens of varying shape and spacer length, and by varying the number of substituents on the POSS cage. [91-94] For example, Wang *et al.* reported a series of octameric POSS-based LCs. [94] Smectic phases were achieved when the mesogens were substituted with single flexible chains ($\text{R}^1 = \text{R}^3 = \text{H}$, $\text{R}^2 = -\text{OC}_{12}\text{H}_{25}$), as exemplified by the formation of large birefringent domains under crossed polarizers (Figure 10b). When the mesogens were substituted with two or three flexible chains, no LC phases were formed, indicating the importance of the number and length of flexible chains on the phase behavior.

While fully substituted (octameric) POSS materials are easy to synthesize, their transition temperatures remain relatively high, with LC phases being achieved over $100\text{ }^\circ\text{C}$ [94]. However, Kim *et al.* recently showed that smectic phases can be induced by the addition of a nematic LC (4-cyano-4'-heptyloxybiphenyl) (7OCB) to a POSS cage mono-substituted with a cyanobiphenyl (POSS-CB) (Figure 10c). A 30/70 POSS-CB/7OCB composition induced a room-temperature smectic phase in which the nematic LCs crawl into the space between the POSS cages. As evidenced by TEM (Figure 10d), the layered structure had a periodicity of 5.2 nm. Unfortunately, the composition range of the induced smectic phase was very narrow, and the phase diagram was rather complex with several co-existing phases, including various crystalline and nematic regions, which is highly undesirable from a processing standpoint.

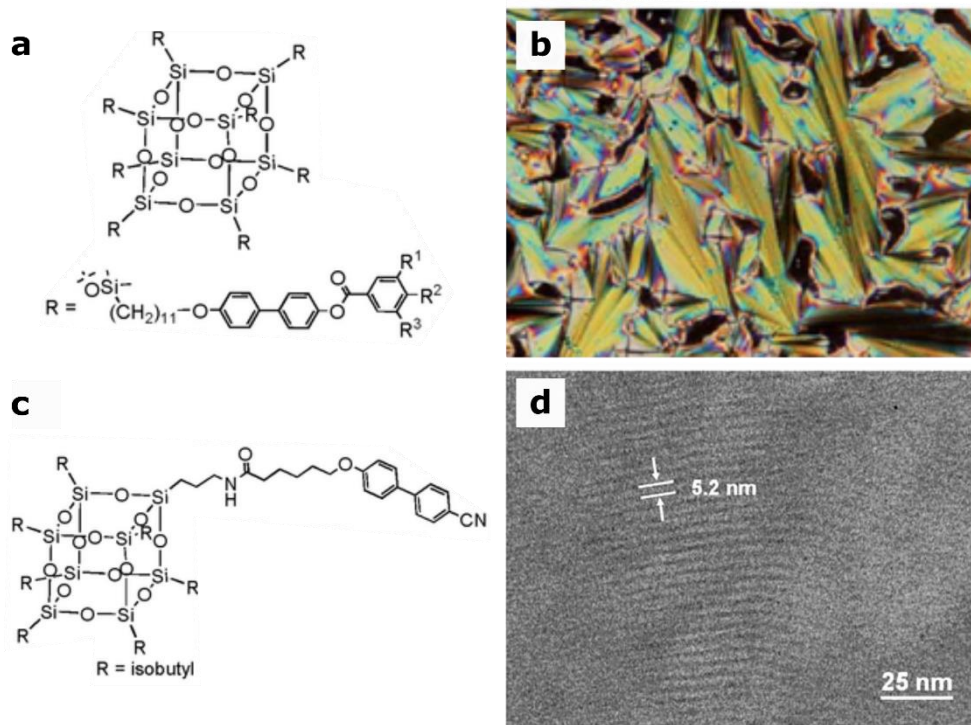


Figure 10. a) Chemical structure of octameric POSS-based LCs. b) POM image of (a) under crossed polarizers at 213 °C ($R_1 = R_3 = H$, $R_2 = -OC_{12}H_{25}$). c) Chemical structure of monomeric POSS-based LC. d) TEM image of the layered structure induced by a POSS-CB/70CB mixture of 30/70 composition. a-b) Reproduced with permission.^[94] Copyright 2011, Royal Society of Chemistry c) Reproduced with permission.^[95] Copyright 2014, American Chemical Society. d) Reproduced with permission.^[96] Copyright 2015, American Chemical Society.

1.2.3.2. Oligo(dimethylsiloxane) (ODMS)

Oligo(dimethylsiloxane) (ODMS), with the chemical formula $(Si(CH_3)_2O)_n$, can also act as a precursor to inorganic silicon oxides through plasma oxidation, making it an attractive etch mask.^[30,38] In contrast to POSS, ODMS is a flexible silicon-containing moiety, which makes it a favorable “coil” moiety in LC design.^[40,43] Due to the chemical incompatibility and large surface tension mismatch of ODMS with most organic materials, nanophase segregation is promoted,^[97–99] which leads to the formation of highly ordered nanostructured morphologies.^[40,41] In the case of rod-coil motifs, smectic^[100,101] discotic,^[43,102] or more complex LC phases^[103,104] are observed, rather than nematic phases,^[40,97] which is a requirement for the preparation of sub-5 nm hybrid organic/inorganic patterns. Although many ODMS-

based LCs have been reported,^[40,41,43,100-108] their ODMS content has been generally restricted to 2-4 repeating units due to an unavailability of commercial ODMS of longer lengths. For nanopatterning applications, higher ODMS fractions are desirable (approximately 50% of the molecule).

Recent progress in the synthesis of discrete ODMS by the group of Meijer has led to the generation of a range of ODMS block molecules with interesting self-assembly behavior. For example, an ureidopyrimidinone (UPy) end-capped ODMS was shown to follow a BCP-like self-assembly behavior, while benzyl-protected derivatives always exhibit a lamellar organization, independent of the molecular composition.^[82] It was hypothesized that crystallization of the benzyl-protected UPy moiety in the UPy-ODMS conjugates was the reason for the generation of the lamellar morphologies. Subsequent investigations of block molecules consisting of naphthalenediimides (NDIs) and ODMS revealed that the synergy of high incompatibility and crystallization of the NDIs drives the formation of conformationally disordered crystal phases characterized by a crystalline-type order and very low mobility.^[109] When a centrally placed NDI moiety was flanked by two ODMS chains, granular textures were observed. Figure 11a-b shows the case where the length of the ODMS chain consisted of 15 DMS units. According to XRD, this material forms a Col_{Hex} phase with a lattice parameter of 6.6 nm. The grainy textures (Figure 11b), together with the large number of sharp reflections observed in the XRD scattering (beyond 4th order), indicate the combination of high order with low mobility, typical for conformationally disordered crystal phases. When NDI moieties were placed on the periphery of an ODMS bridge, this generally gave rise to low-contrast birefringent textures, indicating limited order. An exception was seen for a compound with limited ODMS content, (8 DMS units) (Figure 11c), which formed lamellar crystallites (Figure 11d) with a lattice parameter of 4.4 nm. While the high order observed in these materials is a suitable characteristic for nanolithography applications, the high crystallinity and associated low mobility of conformationally disordered crystal phases are likely undesirable for DSA processes.

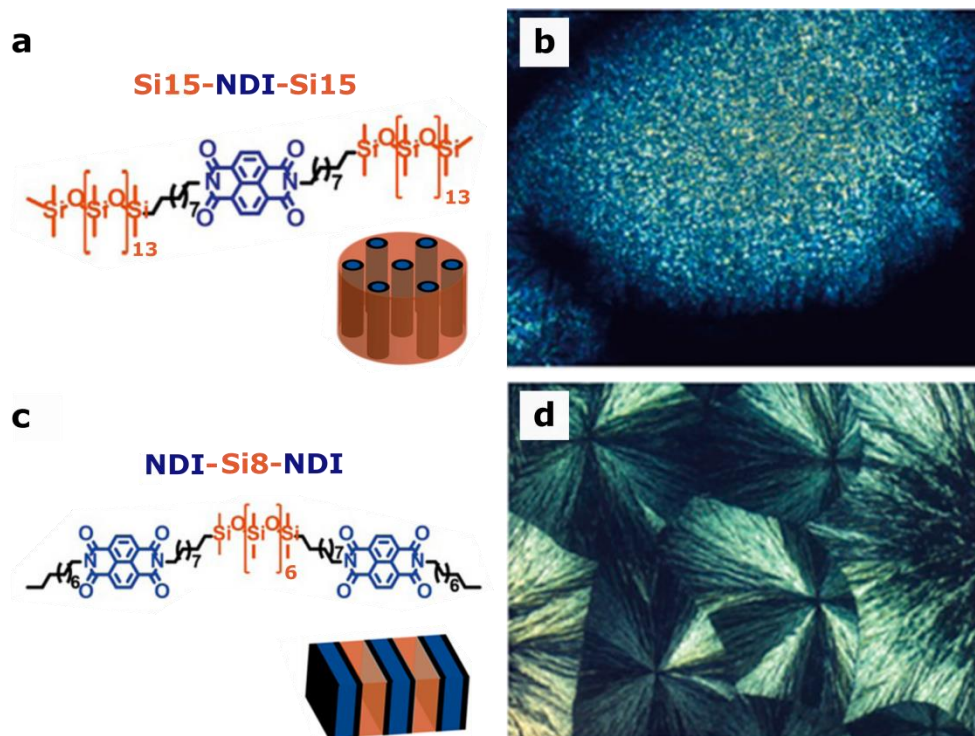


Figure 11. a) Chemical structure of Si15-NDI-Si15 which forms a Col_{Hex} phase. b) POM image of Si15-NDI-Si15 showing granular texture. c) Chemical structure of NDI-Si8-NDI which forms a lamellar morphology. d) POM image of NDI-Si8-NDI showing a spherulitic texture. POM images obtained under crossed polarizers after slow cooling from the isotropic melt. Reproduced with permission. [109] Copyright 2017, American Chemical Society.

1.3. Directed self-assembly of sub-5 nm patterns

To date, the thin film directed self-assembly of hybrid organic/inorganic small molecules has not been explored, even though it is a crucial step for nanopatterning applications. However, higher-order LCs can be envisioned for other applications, including organic electronics, porous membranes, and templated synthesis. Figure 12 schematically depicts these applications and their alignment configurations for discotic LCs (similar for smectics). Similar to nanopatterning applications, they require the fabrication of thin film nanostructure arrays with sub-5 nm features, a high level of perfection, and a unidirectional alignment over large areas. [47,110–113]

These functional thin films with sub-5 nm features provide their own opportunities to be relevant for nanopatterning. In this part, we will discuss the

directed self-assembly of sub-5 nm nanostructured LCs for organic electronics (Section 1.3.1), and nanoporous membranes (Section 1.3.2). To this end, we provide a brief overview of LCs having sub-5nm patterns for these applications and highlight suitable alignment methods for each case. We further highlight opportunities from a nanopatterning perspective.

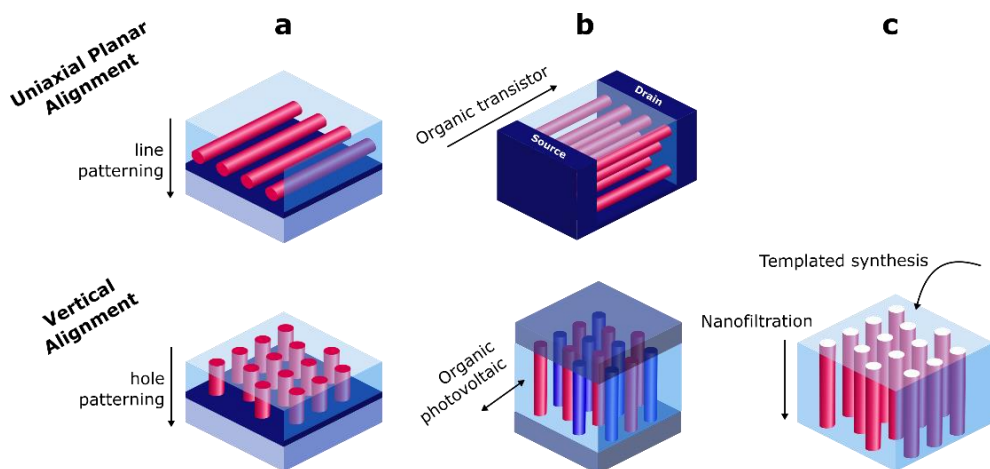


Figure 12. Applications employing discotic LCs with uniaxial planar alignment (top) and vertical alignment (bottom), include a) nanopatterning, b) organic electronics, c) porous membranes and templated synthesis.

1.3.1. Organic electronics

For the design of higher-order LCs for organic electronic applications such as organic photovoltaics, organic light emitting diodes, and organic transistors, the reader is referred to many available reviews.^[43,59,114–118] In brief, LC materials are required with a high charge carrier mobility for selective 1D charge transport (Figure 12b). High charge carrier mobilities are achieved by using π -conjugated molecules, such as triphenylenes, phthalocyanines,^[119] and perylene bisimides.^[120] Separation between LC columns can be improved by using highly immiscible terminal tails, such as oligo(dimethylsiloxane)s or a fluorinated alkyl tails.^[43] For applications in organic electronics, the alignment of the LC phases into large-area domains with minimal structural defects is essential for efficient charge transport between electrodes.^[59] Both uniaxial planar and vertical alignments can be useful, depending on the envisioned application (Figure 12b).

Organic transistors require uniaxial planar alignment between source and drain.^[114] Scaling down of the uniaxial alignment of columnar π - π conjugated systems to the nanometer range, and ultimately to single columns, would permit the fabrication of high density organic transistors arrays. Mouthuy *et. al.* demonstrated one of the earliest examples of uniaxial planar alignment using topological guiding structures (Figure 13a-e).^[121] The researchers studied a tetrasubstituted phthalocyanine which forms a columnar LC mesophase at room temperature. For the confinement, 200 nm wide guiding structures were fabricated by e-beam lithography and subsequent etching into silicon oxide. After deposition of the LCs by spin-coating and short thermal annealing, the LC phase was found to form in-plane oriented multilayers with a periodicity of approximately 3 nm. AFM phase images revealed that LC columnar axis was perpendicular to the long axis of the guiding structures (Figure 13c), likely due to surface anchoring of the discotic core on the hydrophilic guiding surfaces. A strikingly low level of defects was observed. The researchers were also able to induce the parallel orientation of cylinders to the guiding structures by using a crisscross pattern.^[121] In subsequent work, the LCs were deposited within tangentially aligned spiral networks with variable curvature radii resulting in the controlled bending of the LC columns (Figure 13d-e).^[122] For this particular LC, tangential alignment of the LC columns was obtained down to a curvature radius of approximately 1 μ m. At lower curvature radii, the LC columns followed a random alignment with respect to the spiral network, indicating that the bending energy of the columns overtakes the energy gain from the alignment at this limit.

Zhang *et al.* studied the self-assembly of columnar LCs in anodized aluminium oxide (AAO) pores.^[123,124] The researched studied, amongst other LCs, a soft dendronized carbazole which forms a hexagonal columnar phase at room temperature with a lattice spacing of 3.9 nm. It was found that the LC prefers to align parallel to substrate surfaces (Figure 13f), resulting in a circular concentric alignment inside the AAO pore. Incredibly, curvatures approaching the lattice spacing were tolerated for this 'soft' LC (Figure 13h), which illustrates the amenability of these materials for directed self-assembly. Interestingly, axial alignment could be obtained over circular alignment by choosing an LC with a higher rigidity (Figure 13e). This finding exemplifies the importance of molecular design towards achieving the application-specific required orientation of the LC phase.

In the aforementioned studies, the confinement geometry was limited to several hundred nanometers (*i.e.* the size of the pore). Cattle *et. al.* demonstrated the

alignment of a range of triphenylene and phthalocyanine-based discotic liquid crystals with widely spaced topological guiding structures.^[125] Using photolithography, SU8 channels of width 2-25 μm were fabricated on hydrophilic substrates. Amongst other LCs, the researchers investigated a substituted triphenylene which forms a Col_{hex} phase at 85 $^{\circ}\text{C}$, and a crystalline phase at room temperature (Figure 13j). For the alignment, a small amount of crystalline material was placed adjacent to the channels (Figure 13l, top left), heated to the isotropic phase to enable capillary filling, and cooled into the Col_{hex} phase (0.5 $^{\circ}\text{C}/\text{min}$). As a result, in-plane alignment was obtained, with the column director oriented across the microchannel (Figure 13k). The same observation was made for all investigated triphenylene and phthalocyanine compounds. The researchers concluded that the cooling rate, the width of the channel, and the strength of the anchoring interaction were critical for alignment. Under the investigated conditions, a slow cooling rate (0.1 $^{\circ}\text{C}/\text{min}$), and channels of limited width ($< 5\mu\text{m}$), were optimal for the realization of monolithically oriented columnar structures. Even though the alignment of the sub-5 nm patterns was not investigated at the nanoscale, the results imply that the influence of the guiding channels extends to several μm , which is roughly 3 orders of magnitude larger than the periodicity of the patterns themselves.

Organic photovoltaics require the vertical alignment between electrodes of electron donor and acceptor moieties (Figure 12b, red and blue columns). Higher-order columnar LC phases are ideally suited because the distance between the columns should be no greater than the exciton diffusion length, approximately 5–15 nanometers.^[60,126] The most straightforward way towards obtaining vertical alignment for columnar LC phases is to confine them between parallel surfaces, while slowly cooling from the isotropic melt.^[121,127,128] In this process, the vertical alignment is driven by a nucleation and growth process which is initiated at the interfaces. Hence, the process benefits from a slow cooling rate and depends on the film thickness.

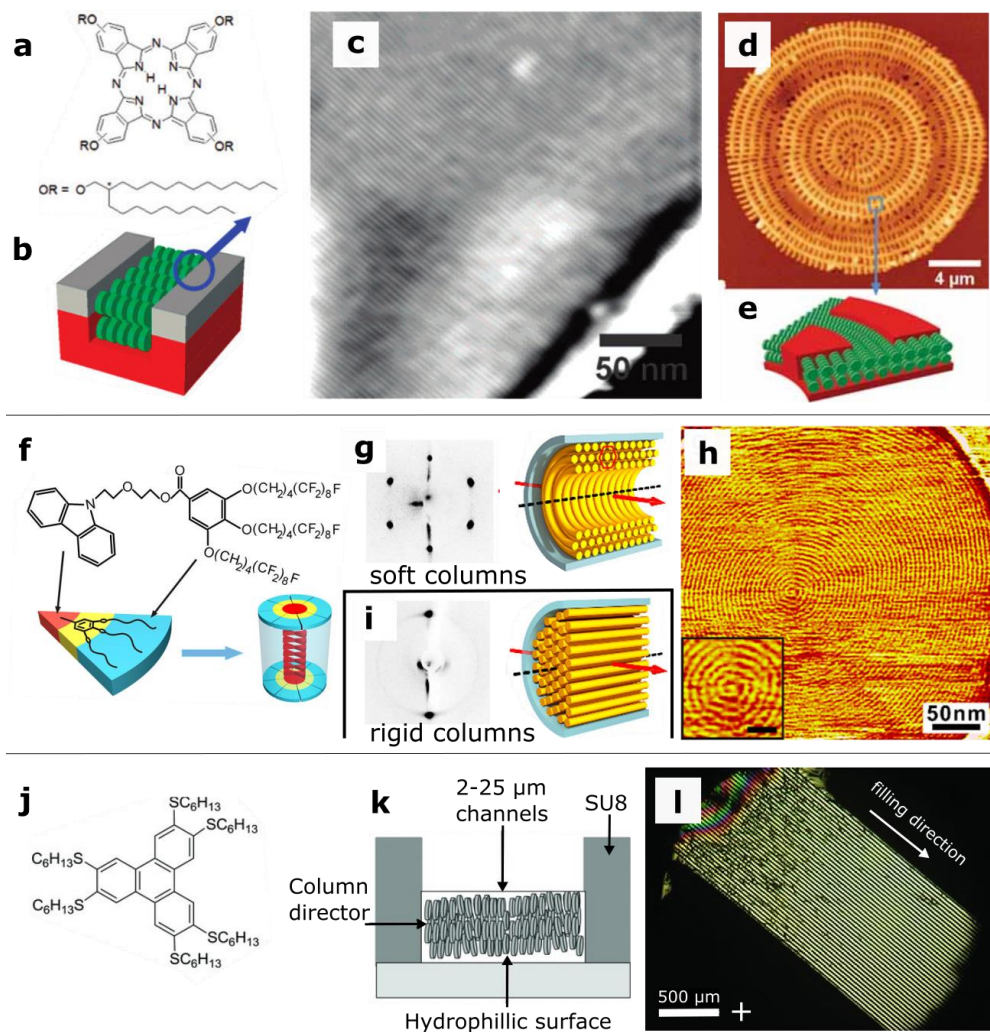


Figure 13. Topological alignment of sub-5 nm patterns for organic electronics. a-c) In-plane alignment of a tetrasubstituted phthalocyanine in topological guiding structures of 200 nm width. d-e) Alignment of (a) in a tangentially aligned spiral network. f-h) Circular alignment of a soft dendronized carbazole (f) in 400 nm circular anodized alumina pore showing extremely high curvature (bar in inset = 8 nm). i) In the case of rigid LCs, axial rather than circular alignment is generated. j-k) In-plane alignment of substituted triphenylene (j) in SU8 microchannels. l) POM image of (j) in 10 μm wide SU8 channels. The cross represents the polarizer axes. The arrow indicates the filling direction. a-c) Reproduced with permission. ^[121] Copyright 2007, American Chemical Society. d-e) Reproduced with permission. ^[122] Copyright 2008, Wiley. f-g) Adapted with permission. ^[124] Copyright 2015, American Chemical Society. j-k) Adapted with permission. ^[125] Copyright 2013, Wiley.

Kwon *et. al.* recently demonstrated the general applicability of the confinement method to a range of supramolecular materials.^[129] The researchers investigated, amongst other LCs, a fluorinated tapered dendrimer containing a crown ether (Figure 14a). Via the fluorophobic effect, this material forms cylindrical dendrimers which pack in a hexagonal lattice with a spacing of ca. 4.5 nm (Figure 14b).^[130] The crown ethers can be replaced with a large number of other functionalities which become part of the core of these supramolecular columns (i.e., donors, acceptors, donor–acceptor complexes) to form complex electronic materials.^[131] A 150 nm film of the fluorinated tapered monodendron was coated on a carbon substrate, covered with a PDMS top surface, heated to the isotropic phase (78 °C), and slowly cooled back to room temperature (Col_{Hex} phase) (Figure 14c). As indicated by TEM, a vertical alignment was achieved with high order (Figure 14d). Large area, vertically oriented domains were not only found with carbon substrates and PDMS top surfaces, but also with any other combination of PDMS, Teflon, perfluoropolyether (PFPE), polyethyleneimine (PEI), and carbon. In contrast, polydomain structures were observed when single substrates were used, with varying vertical or planar orientation determined by the specific interaction between the dendrimer and supporting substrate. Hence, the face-on orientation of the planar aromatic moieties is likely due to contact at the top and bottom interfaces.

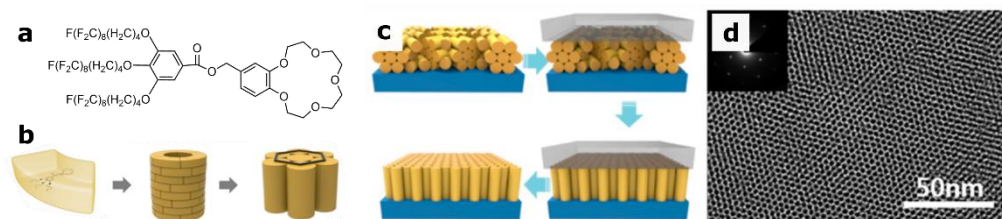


Figure 14. Vertical alignment of sub-5 nm patterns by confinement. a) perfluorinated tapered monodendron, b) cylindrical dendrimers formed by (a) with 4.5 nm lattice spacing. c) soft confinement protocol. d) TEM image after annealing a thin film of dendrimer (a) between a carbon bottom (carbon supported TEM grid) and a PDMS top surface while cooling from the isotropic transition temperature (78 °C) to room temperature at a rate of 0.1 °C min⁻¹. Reproduced with permission.^[129] Copyright 2015, American Chemical Society.

1.3.2. Nanoporous membranes

Nanofiltration membranes for the size-selective separation of small (<5 nm) organic solutes and ionic species require narrow porous channels with sub-5 nm features.^[54] For the construction of sub-5 nm porous membranes, most often

lyotropic LCs^[132,133] are utilised, but thermotropic LCs have also been employed.^[53] LC monomers are highly suitable as template molecules for the fabrication of porous membranes since they can be cross-linked to form rigid polymeric materials.^[134] Selective removal of a specific molecular component in a following step yields hollow channels with the dimensions of the template (1 - 2 nm). Given their monodispersity and customizable chemical functionality, LC materials could overcome the limitations of conventional membrane fabrication approaches with regard to pore size distribution, tortuosity, and selectivity.^[54] Furthermore, the porous channels provide an opportunity to be filled with inorganic materials for the preparation of hybrid organic/inorganic nanostructured materials (Section 1.4) which are interesting from a nanopatterning perspective.

In order to produce through-film channels for nanofiltration membranes, the LC columns must be vertically oriented and highly ordered with minimal defects throughout the thickness of the membrane. Magnetic alignment is particularly well suited for the alignment of LC mesophases.^[51,135] The great advantage of magnetic fields is their ability to penetrate homogeneously into the bulk from a distance, which allows the alignment of the entire sample in a noncontact manner. When LCs are placed in a magnetic field, they align preferentially with their most magnetically susceptible axis ('easy' axis) oriented parallel to the field. For calamitic LCs consisting of mostly aromatic groups, the easy axis is along the long axis of the molecule (positive diamagnetic susceptibility), resulting in the parallel alignment in the magnetic field (Figure 7c). For discotic LCs, the easy axis is typically in the plane of the aromatic rings (negative diamagnetic susceptibility), since the component of the diamagnetic susceptibility perpendicular to an aromatic ring is greater than the in-plane component.^[42] For discotics in a static magnetic field, this results in a degenerate scenario in which all azimuthal orientations of LC columns are isoenergetic. The degeneracy can be lifted by use of a rotating magnetic field.^[51,136,137]

Feng *et. al.*, investigated the magnetic alignment of a wedge-shaped amphiphilic monomer (Figure 15a).^[51] Structural "freezing in" of the LC order is promoted by the use of multiple reactive groups per monomer. In this study, a dense lyotropic phase was obtained with hexagonal symmetry and a lattice spacing of 3.6 nm by combining the LC monomer with a small amount of water. For the magnetic alignment, the material was slowly cooled in a rotating magnetic field (achieved by rotating the sample in a static field). The mesophase was aligned such that the least magnetically susceptible axis ('difficult' axis) was oriented parallel to the axis of rotation (Figure 15b). By lifting the degeneracy, oriented structures were obtained

that are impossible to obtain by using a static field only.^[51,137] After cross-linking the mesophase by polymerization, TEM images were obtained of the polymeric films perpendicular (Figure 15c) and parallel (Figure 15d) to the rotation axis, providing direct evidence of the long-range persistence of vertically aligned nanopores. The resulting ionic channels had a diameters of ca. 1 nm. Remarkably, ion conductivity measurements on the aligned membranes showed an 85-fold enhancement of conductivity over nonaligned samples.^[51]

The nondestructive nature of magnetic fields over longer time periods enables their use in combination with slower self-assembly processes such as surface alignment.^[136] Feng *et al.* recently demonstrated the preparation of vertically aligned nanopores based on conjugated linoleic acid (CLA) monomers. When combined in a 3:1 ratio with a 1,3,5-tris(1H-benzo[d]imidazol-2-yl)benzene (TBIB) core, these materials form a thermotropic Col_{Hex} phase at room temperature (Figure 15e) with a lattice spacing of 2.6 nm.^[136] The LC phase is formed through triple hydrogen bonding interactions by acid-base proton sharing, which leads to a partially ionic character. For relatively thin films (<5 μm), vertical alignment was achieved using a polyelectrolyte poly(sodium 4-styrenesulfonate) (PSS) surface which shows a strong affinity for the LC core. Therefore, anchoring of the core through ionic interactions resulted in a vertical alignment. For relatively thick films (> 5 micrometer), surface alignment alone was insufficient for obtaining through-film vertically oriented channels. For this reason, the PSS surface modification was combined with a rotating magnetic field (Figure 15f). The vertically aligned films exhibited optical extinction under crossed polarizers, thereby confirming their vertical alignment throughout the thickness of the film (Figure 15g). The TBIB core could be recovered by crystallization from solution, and subsequent adsorption experiments performed with model dye molecules demonstrated that the 1-1.5 nm ionic pores displayed size and charge selectivity. However, pattern collapse was observed upon drying of the films, which prohibits the use of these materials as an etch mask. Pattern collapse during the wet-development of high aspect ratio features in lithography is a well-established phenomenon in BCP lithography, and is due to large capillary forces.^[138] However, the filling of the ionic channels with inorganic precursors could be an alternative route towards obtaining hybrid organic/inorganic sub-5 nm patterns.

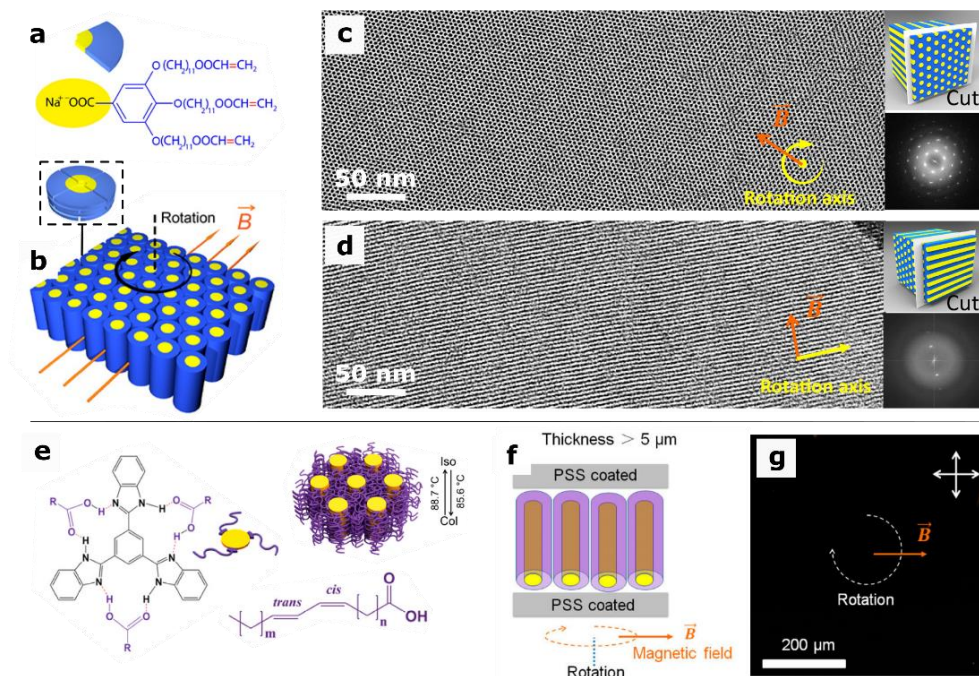


Figure 15. Fabrication of sub-5 nm porous membranes. a-b) Vertical alignment of a wedge-shaped amphiphilic LC (a) by a rotating magnetic field (b). c-d) TEM image taken perpendicular (c) and parallel (d) to the rotation axis, obtained after cross-linking. e-g) Vertical alignment of a triple-hydrogen bonding columnar LC (e) using a combination of surface alignment and magnetic field alignment. g) POM image of an aligned film of $\sim 15 \mu\text{m}$ thickness. The crosses represent the crossed polarizer axes. a-d) Adapted with permission. ^[51] Copyright 2014, American Chemical Society. e-g) Reproduced with permission. ^[136] Copyright 2017, American Chemical Society.

LC-derived porous materials can be employed for direct templating of inorganic materials by filling up the nanopores,^[56,57,139,140] which could be an interesting route towards lithographic etch masks. Our group has demonstrated the filling of porous materials formed by smectic hydrogen bonding LCs. The smectic LC formulation consisted of hydrogen bonding acrylate monomers which form hydrogen bonds between the smectic layers by carboxylic acid dimerization, and 10% of a diacrylate cross linker (Figure 16a). The interlayer crosslinks ensure that the structural integrity of the polymer is maintained after breakage of the hydrogen bonds in a basic solution (Figure 16b), which results in a stable polymer film, useful as a high capacity adsorber material for cationic dyes.^[53] The 2D smectic porous polymer network was subsequently used to fabricate silver nanoparticles by the infiltration of silver nitrate and subsequent reduction of the silver ions within the pores (Figure 16b).^[57] The diameter of the silver nanoparticles could be controlled by the covalent cross-linker.

Moreover, the process was amenable to other metal precursors, such as zinc ions. Further investigation of the silver nanoparticle polymer film by peak force tapping atomic force microscopy (PFT AFM) revealed a layered morphology over a large area (Figure 16c). The periodicity of the hybrid organic/inorganic features was approximately 4.3 nm.

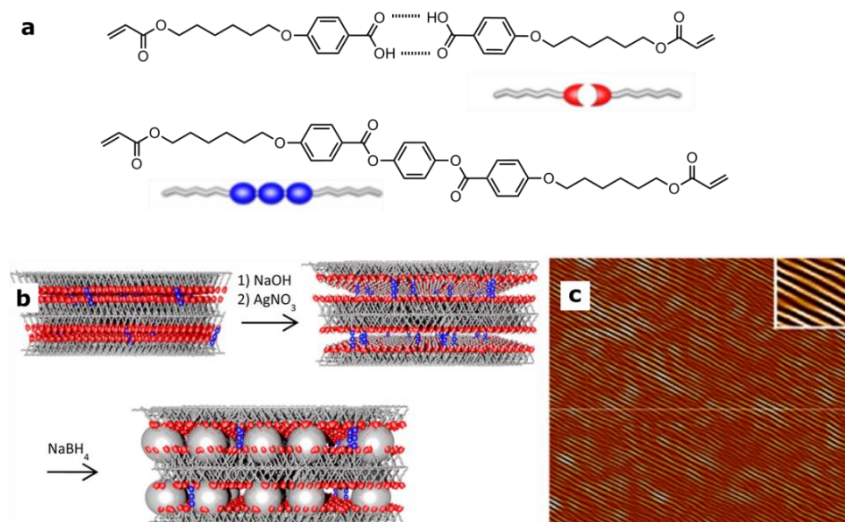


Figure 16. Synthesis of silver nanoparticles in a nanoporous smectic LC polymer network. a) Chemical structures of hydrogen-bonded LC dimer and covalent crosslinker. b) Schematic representation of the fabrication method of the silver nanoparticles within a smectic LC polymer network. c) Fourier transform refined image of a PFT AFM deformation map (500 × 500 nm) of a cryomicrotomed silver nanoparticle polymer film. Reproduced with permission. ^[57] Copyright 2013, American Chemical Society.

1.4. Aim and outline

While lithography based on directed self-assembly can in principle offer higher feature densities compared to optical lithography, three grand challenges remain for its adoption by the semiconductor industry: (1) the scaling of the technology to sub-5 nm feature sizes, (2) the directed self-assembly of the sub-5 nm patterns into defect-free thin films with a predetermined orientation, and (3) the conversion of the self-assembled morphologies into an inorganic array by selectively etching the respective molecular components.

Recent progress towards functional thin film nanostructures at the sub-5 nm length scale shows that thermotropic LC phases formed by small molecules offer

self-assembly at the molecular length scale, i.e. sub-5 nm, and they are particularly amenable to DSA processes due to the soft nature of the intermolecular interactions. Hybrid organic/inorganic sub-5 nm LC patterns are especially attractive from a nanopatterning perspective for their inherent etch contrast, but these materials, as can be concluded from this review, have not been investigated for nanopatterning purposes; their thin film directed self-assembly has not been explored, nor has their selective etching been demonstrated.

This thesis explores the directed self-assembly of oligo(dimethylsiloxane)-based liquid crystals for sub-5 nm patterning. Chapter two and three describe the synthesis and characterization of ODMS LCs which form columnar and lamellar morphologies respectively. We demonstrate that these hybrid organic-inorganic materials form thin film nanostructures with ultrafine sub-5 nm dimensions. We further illustrate the uniaxial planar alignment of the columnar LC nanopatterns using topological pre-patterns. Chapter four describes the photo-alignment of the columnar LC nanostructures by actinic light. Uniaxial planar alignment was achieved by exposure to linearly polarized light, and the alignment process was investigated in detail. Vertical alignment was achieved by exposure to unpolarized light. However, the vertical morphology was unstable due to the surface energy disparity between the ODMS and organic components of the molecules. Importantly, this result highlights an important difference between BCPs and LCs; while the removal of defects is facilitated by the low glass transition temperature of the LCs, the retention of the metastable out-of-plane morphology is hampered. To address this issue, a series of acrylate-terminated ODMS LCs was developed in chapter five. Cross-linking of the smectic phase formed by these compounds resulted in stable nanostructured polymers with retention of the structural order. An added benefit of these reactive materials is the possibility for micropatterning by mask polymerization. An alternative method to 'lock-in' LC order is proposed in chapter six. Novel hydrogen bonding ODMS LCs were prepared and mixed with a glassy hydrogen-bond accepting polymer to yield a range of glassy nanoscale morphologies. By mixing the LCs with a block copolymer, hierarchical morphologies are generated. The synergistic co-assembly phenomenon was used to realize a 'sandwich' structure in which the smectic LC phase is vertically aligned. Finally, chapter seven gathers the current challenges and opportunities regarding LCs for nanopatterning, and discloses a class of azobenzene-containing hydrogen-bonding ODMS LCs for the photoalignment of glassy, hierarchically oriented structures, thereby combining the concepts of previous chapters.

1.5. References

- [1] G. Moore, *Electronics* **1965**, 38, 114.
- [2] “Transistor count,” can be found under https://en.wikipedia.org/w/index.php?title=Transistor_count&oldid=785729146, **2017**.
- [3] B. J. Lin, *J Microlithogr Microfab Microcyst* **2004**, 3, 377.
- [4] G. Tallents, E. Wagenaars, G. Pert, *Nat. Photonics* **2010**, 4, 809.
- [5] C. Wagner, N. Harned, *Nat. Photonics* **2010**, 4, 24.
- [6] G. Kreindl, T. Glinsner, R. Miller, *Nat. Photonics* **2010**, 4, 27.
- [7] R. Ruiz, H. M. Kang, F. A. Detcheverry, E. Dobisz, D. S. Kercher, T. R. Albrecht, J. J. de Pablo, P. F. Nealey, *Science* **2008**, 321, 936.
- [8] T. Thurn-Albrecht, J. Schotter, C. A. Kastle, N. Emley, T. Shibauchi, L. Krusin-Elbaum, K. Guarini, C. T. Black, M. T. Tuominen, T. P. Russell, *Science* **2000**, 290, 2126.
- [9] S. Park, D. H. Lee, J. Xu, B. Kim, S. W. Hong, U. Jeong, T. Xu, T. P. Russell, *Science* **2009**, 323, 1030.
- [10] C. M. Bates, M. J. Maher, D. W. Janes, C. J. Ellison, C. G. Willson, *Macromolecules* **2014**, 47, 2.
- [11] S.-J. Jeong, J. Y. Kim, B. H. Kim, H.-S. Moon, S. O. Kim, *Mater. Today* **2013**, 16, 468.
- [12] S. B. Darling, *Prog. Polym. Sci.* **2007**, 32, 1152.
- [13] H. Hu, M. Gopinadhan, C. O. Osuji, *Soft Matter* **2014**, 10, 3867.
- [14] S. Ji, L. Wan, C.-C. Liu, P. F. Nealey, *Prog. Polym. Sci.* **2016**, 54–55, 76.
- [15] J. G. Son, K. W. Gotrik, C. A. Ross, *ACS Macro Lett.* **2012**, 1, 1279.
- [16] C. Sinturel, M. Vayer, M. Morris, M. A. Hillmyer, *Macromolecules* **2013**, 46, 5399.
- [17] T. L. Morkved, M. Lu, A. M. Urbas, E. E. Ehrichs, H. M. Jaeger, P. Mansky, T. P. Russell, *Science* **1996**, 273, 931.
- [18] H. Tran, M. Gopinadhan, P. W. Majewski, R. Shade, V. Steffes, C. Osuji, L. M. Campos, *ACS Nano* **2013**, 7, 5514.
- [19] A. Nunns, J. Gwyther, I. Manners, *Polymer* **2013**, 54, 1269.
- [20] J. Bang, U. Jeong, D. Y. Ryu, T. P. Russell, C. J. Hawker, *Adv. Mater.* **2009**, 21, 4769.
- [21] J. Chai, J. M. Buriak, *ACS Nano* **2008**, 2, 489.
- [22] H. Y. Tsai, J. W. Pitera, H. Miyazoe, S. Bangsaruntip, S. U. Engelmann, C. C. Liu, J. Y. Cheng, J. J. Bucchignano, D. P. Klaus, E. A. Joseph, D. P. Sanders, M. E. Colburn, M. A. Guillorn, *ACS Nano* **2014**, 8, 5227.
- [23] L. Yao, L. E. Oquendo, M. W. Schulze, R. M. Lewis, W. L. Gladfelter, M. A. Hillmyer, *ACS Appl. Mater. Interfaces* **2016**, 8, 7431.
- [24] M. D. Rodwogin, C. S. Spanjers, C. Leighton, M. A. Hillmyer, *ACS Nano* **2010**, 4, 725.
- [25] C. Cummins, T. Ghoshal, J. D. Holmes, M. A. Morris, *Adv. Mater.* **2016**, 28, 5586.
- [26] C. A. Ross, Y. S. Jung, V. P. Chuang, F. Ilievski, J. K. W. Yang, I. Bitá, E. L. Thomas, H. I. Smith, K. K. Berggren, G. J. Vancso, J. Y. Cheng, *J. Vac. Sci. Technol. B Microelectron. Nanometer Struct.* **2008**, 26, 2489.

- [27] T. Hirai, M. Leolukman, C. C. Liu, E. Han, Y. J. Kim, Y. Ishida, T. Hayakawa, M. Kakimoto, P. F. Nealey, P. Gopalan, *Adv. Mater.* **2009**, *21*, 4334.
- [28] D. Borah, S. Rasappa, R. SenthamaraiKannan, B. Kosmala, M. T. Shaw, J. D. Holmes, M. A. Morris, *ACS Appl. Mater. Interfaces* **2013**, *5*, 88.
- [29] S. Archambault, C. Girardot, M. Salaun, M. Delalande, S. Bohme, G. Cunge, E. Pargon, O. Joubert, M. Zelsmann, *Adv. Etch Technol. Nanopatterning III* **2014**, 9054.
- [30] Y. S. Jung, J. B. Chang, E. Verploegen, K. K. Berggren, C. A. Ross, *Nano Lett.* **2010**, *10*, 1000.
- [31] Y. S. Jung, C. A. Ross, *Nano Lett.* **2007**, *7*, 2046.
- [32] Y. S. Jung, W. Jung, H. L. Tuller, C. A. Ross, *Nano Lett.* **2008**, *8*, 3776.
- [33] S. Xiao, X. Yang, S. Park, D. Weller, T. P. Russell, *Adv. Mater.* **2009**, *21*, 2516.
- [34] Y. S. Jung, C. A. Ross, *Small* **2009**, *5*, 1654.
- [35] H. Pathangi, B. T. Chan, H. Bayana, N. Vandebroek, D. Van den Heuvel, L. Van Look, P. Rincon-Delgado, Y. Cao, J. Kim, G. Y. Lin, D. Parnell, K. Nafus, R. Harukawa, I. Chikashi, M. Polli, L. D'Urzo, R. Gronheid, P. Nealey, *J MicroNanolith MEMS MOEMS* **2015**, *14*.
- [36] M. Muramatsu, T. Nishi, G. You, Y. Saito, Y. Ido, N. Oikawa, T. Tobana, K. Ito, S. Morikita, T. Kitano, in *Proc SPIE 10144*, **2017**, p. 101440Q.
- [37] S. Hara, H. Wada, A. Shimojima, K. Kuroda, *ACS Nano* **2017**, *11*, 5160.
- [38] K. Nickmans, J. N. Murphy, B. de Waal, P. Leclère, J. Doise, R. Gronheid, D. J. Broer, A. P. H. J. Schenning, *Adv. Mater.* **2016**, *28*, 10068.
- [39] C. Sinturel, F. S. Bates, M. A. Hillmyer, *ACS Macro Lett.* **2015**, *4*, 1044.
- [40] C. Tschierske, *J. Mater. Chem.* **2001**, *11*, 2647.
- [41] C. Tschierske, *Angew. Chem.-Int. Ed.* **2013**, *52*, 8828.
- [42] J. W. Goodby, D. Demus, J. Goodby, G. W. Gray, H. W. Spiess, V. Vill, in *Handb. Liq. Cryst. Set*, Wiley-VCH Verlag GmbH, **2008**, pp. 3–21.
- [43] T. Wöhrle, I. Wurzbach, J. Kirres, A. Kostidou, N. Kapernaum, J. Litterscheidt, J. C. Haenle, P. Staffeld, A. Baro, F. Giesselmann, S. Laschat, *Chem. Rev.* **2016**, *116*, 1139.
- [44] L. Li, Y. Tang, H. Yu, J. Yang, J. Zhao, *Displays and Sensors Integrated with Multi-State Cholesteric Liquid Crystal Devices*, **2015**, US9046730 B2.
- [45] D. J. Broer, C. M. W. Bastiaansen, M. G. Debije, A. P. H. J. Schenning, *Angew. Chem.-Int. Ed.* **2012**, *51*, 7102.
- [46] K. Nickmans, G. M. B. Bogels, C. Sánchez-Somolinos, J. N. Murphy, P. Leclère, I. Voets, A. P. H. J. Schenning, *Small* **2017**, *13*, 1701043
- [47] T. Kato, N. Mizoshita, K. Kishimoto, *Angew. Chem. Int. Ed.* **2006**, *45*, 38.
- [48] C. L. van Oosten, C. W. M. Bastiaansen, D. J. Broer, *Nat. Mater.* **2009**, *8*, 677.
- [49] D. Liu, D. J. Broer, *Nat. Commun.* **2015**, *6*, 8334.
- [50] H. Shahsavan, S. M. Salili, A. Jákli, B. Zhao, *Adv. Mater.* **2015**, *27*, 6828.
- [51] X. D. Feng, M. E. Tousley, M. G. Cowan, B. R. Wiesenauer, S. Nejati, Y. Choo, R. D. Noble, M. Elimelech, D. L. Gin, C. O. Osuji, *ACS Nano* **2014**, *8*, 11977.

- [52] C. L. Gonzalez, C. W. M. Bastiaansen, J. Lub, J. Loos, K. Lu, H. J. Wondergem, D. J. Broer, *Adv. Mater.* **2008**, *20*, 1246.
- [53] H. P. C. van Kuringen, G. M. Eikelboom, I. K. Shishmanova, D. J. Broer, A. P. H. J. Schenning, *Adv. Funct. Mater.* **2014**, *24*, 5045.
- [54] J. R. Werber, C. O. Osuji, M. Elimelech, *Nat. Rev. Mater.* **2016**, *1*, 16018.
- [55] M. Zhou, T. J. Kidd, R. D. Noble, D. L. Gin, *Adv. Mater.* **2005**, *17*, 1850.
- [56] Y. Xu, H. P. C. van Kuringen, D. J. Mulder, A. P. H. J. Schenning, N. A. J. M. Sommerdijk, *RSC Adv.* **2016**, *6*, 13953.
- [57] D. Dasgupta, I. K. Shishmanova, A. Ruiz-Carretero, K. B. Lu, M. Verhoeven, H. P. C. van Kuringen, G. Portale, P. Leclere, C. W. M. Bastiaansen, D. J. Broer, A. P. H. J. Schenning, *J. Am. Chem. Soc.* **2013**, *135*, 10922.
- [58] M. O'Neill, S. M. Kelly, in *Liq. Cryst. Semicond.* (Eds.: R.J. Bushby, S.M. Kelly, M. O'Neill), Springer Netherlands, **2013**, pp. 247–268.
- [59] S. Sergeev, W. Pisula, Y. H. Geerts, *Chem. Soc. Rev.* **2007**, *36*, 1902.
- [60] M. Kumar, S. Kumar, *Polym. J.* **2017**, *49*, 85.
- [61] M. O'Neill, S. M. Kelly, in *Liq. Cryst. Semicond.* (Eds.: R.J. Bushby, S.M. Kelly, M. O'Neill), Springer Netherlands, **2013**, pp. 219–245.
- [62] Y. Shimizu, in *Nanosci. Liq. Cryst.* (Ed.: Q. Li), Springer International Publishing, **2014**, pp. 257–280.
- [63] Y. H. Kim, D. K. Yoon, H.-T. Jung, *J. Mater. Chem.* **2009**, *19*, 9091.
- [64] J. Hoogboom, J. A. Elemans, T. Rasing, A. E. Rowan, R. J. Nolte, *Polym. Int.* **2007**, *56*, 1186.
- [65] C. M. Bates, F. S. Bates, *Macromolecules* **2017**, *50*, 3.
- [66] W. J. Durand, G. Blachut, M. J. Maher, S. Sirard, S. Tein, M. C. Carlson, Y. Asano, S. X. Zhou, A. P. Lane, C. M. Bates, C. J. Ellison, C. G. Willson, *J. Polym. Sci. Part Polym. Chem.* **2015**, *53*, 344.
- [67] J. D. Cushen, I. Otsuka, C. M. Bates, S. Halila, S. Fort, C. Rochas, J. A. Easley, E. L. Rausch, A. Thio, R. Borsali, C. G. Willson, C. J. Ellison, *ACS Nano* **2012**, *6*, 3424.
- [68] L. M. Pitet, S. F. Wuister, E. Peeters, E. J. Kramer, C. J. Hawker, E. W. Meijer, *Macromolecules* **2013**, *46*, 8289.
- [69] W. Gu, J. Xu, J.-K. Kim, S. W. Hong, X. Wei, X. Yang, K. Y. Lee, D. S. Kuo, S. Xiao, T. P. Russell, *Adv. Mater.* **2013**, *25*, 3677.
- [70] E. Elacqua, D. S. Lye, M. Weck, *Acc. Chem. Res.* **2014**, *47*, 2405.
- [71] N. D. Jarnagin, J. Cheng, A. Peters, W. M. Yeh, R. A. Lawson, L. M. Tolbert, C. L. Henderson, *Altern. Lithogr. Technol. IV* **2012**, 8323.
- [72] D. P. Sweat, M. Kim, A. K. Schmitt, D. V. Perroni, C. G. Fry, M. K. Mahanthappa, P. Gopalan, *Macromolecules* **2014**, *47*, 6302.
- [73] C. Tang, S. Hur, B. C. Stahl, K. Sivanandan, M. Dimitriou, E. Pressly, G. H. Fredrickson, E. J. Kramer, C. J. Hawker, *Macromolecules* **2010**, *43*, 2880.
- [74] C. Tang, E. M. Lennon, G. H. Fredrickson, E. J. Kramer, C. J. Hawker, *Science* **2008**, *322*, 429.

- [75] S. H. Han, V. Pryamitsyn, D. Bae, J. Kwak, V. Ganesan, J. K. Kim, *ACS Nano* **2012**, *6*, 7966.
- [76] Y. Luo, B. Kim, D. Montarnal, Z. Mester, C. W. Pester, A. J. McGrath, G. Hill, E. J. Kramer, G. H. Fredrickson, C. J. Hawker, *J. Polym. Sci. Part Polym. Chem.* **2016**, *54*, 2200.
- [77] S. X. Zhou, D. W. Janes, C. B. Kim, C. G. Willson, C. J. Ellison, *Macromolecules* **2016**, *49*, 8332.
- [78] K. Zhang, S. J. Talley, Y. Peng Yu, R. B. Moore, M. Murayama, T. E. Long, *Chem. Commun.* **2016**, *52*, 7564.
- [79] Y. Sakai-Otsuka, S. Zaiioncz, I. Otsuka, S. Halila, P. Rannou, R. Borsali, *Macromolecules* **2017**, *50*, 3365.
- [80] X. Yu, K. Yue, I. F. Hsieh, Y. Li, X. H. Dong, C. Liu, Y. Xin, H. F. Wang, A. C. Shi, G. R. Newkome, R. M. Ho, E. Q. Chen, W. B. Zhang, S. Z. Cheng, *Proc Natl Acad Sci U A* **2013**, *110*, 10078.
- [81] K. Yue, C. Liu, M. Huang, J. Huang, Z. Zhou, K. Wu, H. Liu, Z. Lin, A.-C. Shi, W.-B. Zhang, S. Z. D. Cheng, *Macromolecules* **2017**, *50*, 303.
- [82] R. H. Zha, B. F. de Waal, M. Lutz, A. J. Teunissen, E. W. Meijer, *J. Am. Chem. Soc.* **2016**, *138*, 5693.
- [83] B. van Genabeek, B. F. M. de Waal, M. M. J. Gosens, L. M. Pitet, A. R. A. Palmans, E. W. Meijer, *J. Am. Chem. Soc.* **2016**, *138*, 4210.
- [84] Y. Wan, Y. Shi, D. Zhao, *Chem. Commun.* **2007**, *0*, 897.
- [85] W. Chen, B. Wunderlich, *Macromol. Chem. Phys.* **1999**, *200*, 283.
- [86] C. Tschierske, *Curr. Opin. Colloid Interface Sci.* **2002**, *7*, 69.
- [87] M. Lee, B. K. Cho, H. Kim, J. Y. Yoon, W. C. Zin, *J. Am. Chem. Soc.* **1998**, *120*, 9168.
- [88] L. Wang, Y. Ishida, R. Maeda, M. Tokita, S. Horiuchi, T. Hayakawa, *Langmuir* **2014**, *30*, 9797.
- [89] L. Wang, Y. Ishida, R. Maeda, M. Tokita, T. Hayakawa, *RSC Adv.* **2014**, *4*, 34981.
- [90] P. Capper, S. Irvine, T. Joyce, in *Springer Handb. Electron. Photonic Mater.* (Eds.: S.K. Prof. P.C. Dr), Springer US, **2006**, pp. 271–301.
- [91] Q. W. Pan, X. F. Chen, X. G. Fan, Z. H. Shen, Q. F. Zhou, *J. Mater. Chem.* **2008**, *18*, 3481.
- [92] P. K. Karahaliou, P. H. J. Kouwer, T. Meyer, G. H. Mehl, D. J. Photinos, *Soft Matter* **2007**, *3*, 857.
- [93] I. M. Saez, J. W. Goodby, *J. Mater. Chem.* **2001**, *11*, 2845.
- [94] X. Wang, C. M. Cho, W. Y. Say, A. Y. X. Tan, C. He, H. S. O. Chan, J. Xu, *J. Mater. Chem.* **2011**, *21*, 5248.
- [95] D.-Y. Kim, S. Kim, S.-A. Lee, Y.-E. Choi, W.-J. Yoon, S.-W. Kuo, C.-H. Hsu, M. Huang, S. H. Lee, K.-U. Jeong, *J. Phys. Chem. C* **2014**, *118*, 6300.
- [96] N. Kim, D.-Y. Kim, M. Park, Y.-J. Choi, S. Kim, S. H. Lee, K.-U. Jeong, *J. Phys. Chem. C* **2015**, *119*, 766.

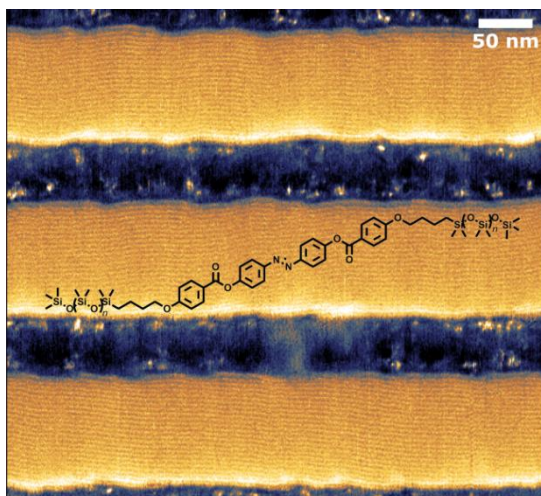
- [97] C. Pugh, J. Y. Bae, J. Dharia, J. J. Ge, S. Z. D. Cheng, *Macromolecules* **1998**, *31*, 5188.
- [98] I. Dierking, L. Komitov, S. T. Lagerwall, T. Wittig, R. Zentel, *Liq. Cryst.* **1999**, *26*, 1511.
- [99] S. Westphal, S. Diele, A. Mädicke, F. Kuschel, U. Scheim, K. Rühlmann, B. Hisgen, H. Ringsdorf, *Makromol. Chem. Rapid Commun.* **1988**, *9*, 489.
- [100] Q. Song, D. Nonnenmacher, F. Giesselmann, R. P. Lemieux, *J. Mater. Chem. C* **2012**, *1*, 343.
- [101] J. Newton, H. Coles, P. Hodge, J. Hannington, *J. Mater. Chem.* **1994**, *4*, 869.
- [102] T. J. Zhang, D. M. Sun, X. K. Ren, L. L. Liu, G. Y. Wen, Z. J. Ren, H. H. Li, S. K. Yan, *Soft Matter* **2013**, *9*, 10739.
- [103] E. Nishikawa, E. T. Samulski, *Liq. Cryst.* **2000**, *27*, 1457.
- [104] R. A. Reddy, U. Baumeister, J. L. Chao, H. Kresse, C. Tschierske, *Soft Matter* **2010**, *6*, 3883.
- [105] R. Achten, A. Koudijs, M. Giesbers, A. Marcelis, E. Sudholter, *Mol. Cryst. Liq. Cryst.* **2007**, *477*, 169.
- [106] E. Corsellis, D. Guillon, P. Kloess, H. Coles, *Liq. Cryst.* **1997**, *23*, 235.
- [107] M. García-Iglesias, B. F. M. de Waal, I. de Feijter, A. R. A. Palmans, E. W. Meijer, *Chem. Eur. J.* **2015**, *21*, 377.
- [108] N. Olsson, B. Helgee, G. Andersson, L. Komitov, *Liq. Cryst.* **2005**, *32*, 1139.
- [109] J. A. Berrocal, R. H. Zha, B. F. M. de Waal, J. A. M. Lugger, M. Lutz, E. W. Meijer, *ACS Nano* **2017**, *11*, 3733.
- [110] J. P. F. Lagerwall, G. Scalia, *Curr. Appl. Phys.* **2012**, *12*, 1387.
- [111] B. Soberats, M. Yoshio, T. Ichikawa, X. Zeng, H. Ohno, G. Ungar, T. Kato, *J. Am. Chem. Soc.* **2015**, *137*, 13212.
- [112] D. B. Amabilino, D. K. Smith, J. W. Steed, *Chem. Soc. Rev.* **2017**, *46*, 2404.
- [113] T. Kato, *Science* **2002**, *295*, 2414.
- [114] B. R. Kaafarani, *Chem. Mater.* **2011**, *23*, 378.
- [115] S. Laschat, A. Baro, N. Steinke, F. Giesselmann, C. Hägele, G. Scalia, R. Judele, E. Kapatsina, S. Sauer, A. Schreivogel, M. Tosoni, *Angew. Chem. Int. Ed.* **2007**, *46*, 4832.
- [116] S. Kumar, *Chem. Soc. Rev.* **2006**, *35*, 83.
- [117] K. Hirota, K. Tajima, K. Hashimoto, *Synth. Met.* **2007**, *157*, 290.
- [118] R. J. Bushby, D. J. Tate, in *Liq. Cryst. Semicond.* (Eds.: R.J. Bushby, S.M. Kelly, M. O'Neill), Springer Netherlands, **2013**, pp. 65–96.
- [119] *Appl. Phys. Lett.* **2005**, *87*, 132102.
- [120] M. Funahashi, A. Sonoda, *J. Mater. Chem.* **2012**, *22*, 25190.
- [121] P. O. Mouthuy, S. Melinte, Y. H. Geerts, A. M. Jonas, *Nano Lett.* **2007**, *7*, 2627.
- [122] P. O. Mouthuy, S. Melinte, Y. H. Geerts, B. Nysten, A. M. Jonas, *Small* **2008**, *4*, 728.

- [123] R. Zhang, X. Zeng, M. Prehm, F. Liu, S. Grimm, M. Geuss, M. Steinhart, C. Tschierske, G. Ungar, *ACS Nano* **2014**, *8*, 4500.
- [124] R. B. Zhang, X. B. Zeng, B. Kim, R. J. Bushby, K. Shin, P. J. Baker, V. Percec, P. Leowanawat, G. Ungar, *ACS Nano* **2015**, *9*, 1759.
- [125] J. Cattle, P. Bao, J. P. Bramble, R. J. Bushby, S. D. Evans, J. E. Lydon, D. J. Tate, *Adv. Funct. Mater.* **2013**, *23*, 5997.
- [126] P. E. Shaw, A. Ruseckas, I. D. W. Samuel, *Adv. Mater.* **2008**, *20*, 3516.
- [127] S. Qu, H. Zhang, Y. Ma, J. Cao, S. Wu, X. Liu, *RSC Adv.* **2013**, *3*, 19104.
- [128] T. Kamei, T. Kato, E. Itoh, K. Ohta, *J. Porphyr. Phthalocyanines* **2012**, *16*, 1261.
- [129] K. Kwon, J. M. Ok, Y. H. Kim, J.-S. Kim, W.-B. Jung, S.-Y. Cho, H.-T. Jung, *Nano Lett.* **2015**, *15*, 7552.
- [130] V. Percec, G. Johansson, G. Ungar, J. Zhou, *J. Am. Chem. Soc.* **1996**, *118*, 9855.
- [131] V. Percec, M. Glodde, T. K. Bera, Y. Miura, I. Shiyonovskaya, K. D. Singer, V. S. K. Balagurusamy, P. A. Heiney, I. Schnell, A. Rapp, H.-W. Spiess, S. D. Hudson, H. Duan, *Nature* **2002**, *419*, 384.
- [132] D. L. Gin, J. E. Bara, R. D. Noble, B. J. Elliott, *Macromol. Rapid Commun.* **2008**, *29*, 367.
- [133] D. L. Gin, X. Lu, P. R. Nemade, C. S. Pecinovsky, Y. Xu, M. Zhou, *Adv. Funct. Mater.* **2006**, *16*, 865.
- [134] A. P. H. J. Schenning, Y. C. Gonzalez-Lemus, I. K. Shishmanova, D. J. Broer, *Liq. Cryst.* **2011**, *38*, 1627.
- [135] D. K. Yoon, S. R. Lee, Y. H. Kim, S.-M. Choi, H.-T. Jung, *Adv. Mater.* **2006**, *18*, 509.
- [136] X. Feng, K. Kawabata, G. Kaufman, M. Elimelech, C. O. Osuji, *ACS Nano* **2017**, *11*, 3911.
- [137] M. E. Tousley, X. Feng, M. Elimelech, C. O. Osuji, *ACS Appl. Mater. Interfaces* **2014**, *6*, 19710.
- [138] R. Ruiz, E. Dobisz, T. R. Albrecht, *ACS Nano* **2011**, *5*, 79.
- [139] I. Gracia, P. Romero, J. L. Serrano, J. Barberá, A. Omenat, *J. Mater. Chem. C* **2017**, *5*, 2033.
- [140] K. Yuan, L. Chen, Y. Chen, *Chem. – Eur. J.* **2014**, *20*, 11488.

Chapter 2

Thin film directed self-assembly of columnar oligo(dimethylsiloxane) liquid crystals

Abstract. This chapter describes the synthesis and characterization of a novel class of monodisperse, oligo(dimethylsiloxane)-based (ODMS) liquid crystals which form columnar morphologies at sub-5 nm periodicities (3.8 – 5.1 nm) in thin films. Highly ordered nanopatterns were obtained by graphoepitaxial directed self-assembly. These hybrid organic/inorganic liquid crystals are of high interest for nanopatterning applications due to the combination of their ultrasmall feature sizes, high etching contrast, and their ability to be directed into highly ordered domains without additional annealing.



This chapter is based on:

K. Nickmans, J. N. Murphy, B. de Waal, P. Leclère, J. Doise, R. Gronheid, D. J. Broer, A. P. H. J. Schenning, *Adv. Mater.* **2016**, 28, 10068

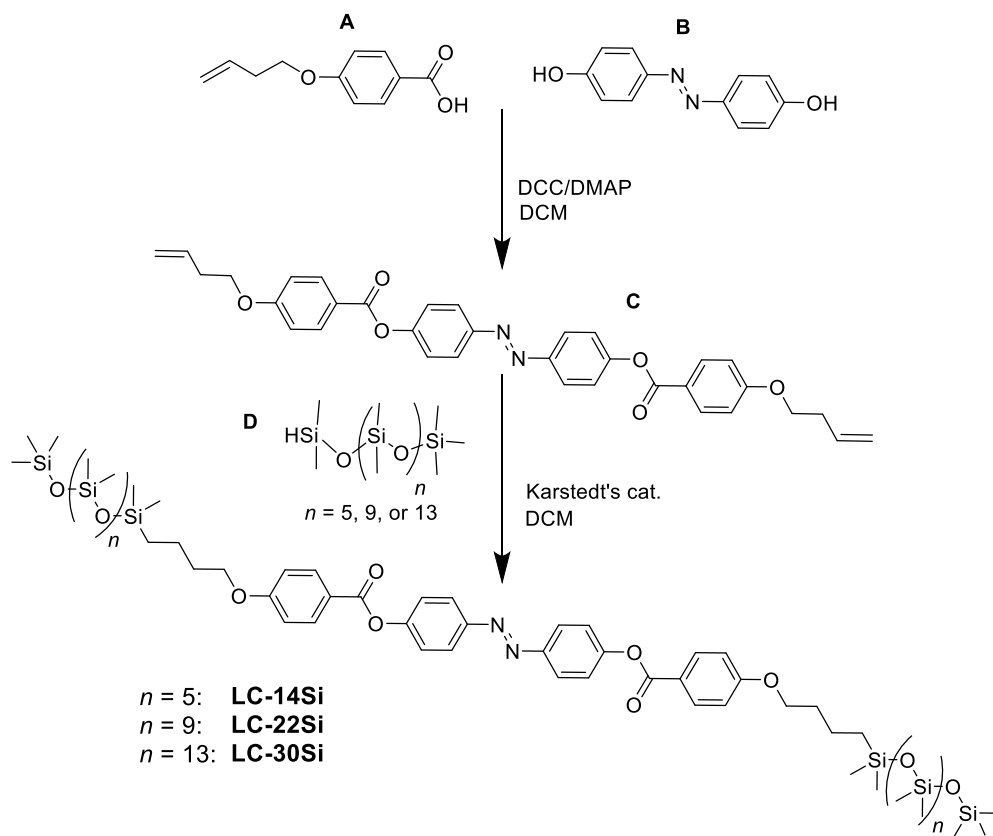
2.1. Introduction

The sustained shrinking of device components is an embodiment of human progress that has led to an explosion of micro- and nano-technologies. As discussed in chapter 1, block copolymer (BCP)-based nano-patterning has paved a strong foundation in nanotechnology including nano-porous membranes, patterned magnetic media, and nanolithography. At the heart of the nano-patterning lies the thin film micro-phase separation of chemically distinct and thermodynamically immiscible polymer blocks into dense periodic structures (10 – 100 nm). To enable pattern transfer, the respective blocks must contain sufficient etching contrast and resistance, which is commonly achieved by introducing silicon into one block of the copolymer.^[1] Among these materials, poly(styrene)-b-poly(dimethylsiloxane) (PS-b-PDMS) is the most widely investigated BCP in which the PS block is removed by oxygen plasma resulting in a silica-rich nano-pattern.^[2,3] The periodic structure depends on the overall degree of polymerization of the polymer blocks (N), and the Flory–Huggins interaction parameter (χ). The additional requirement that χN exceed 10.5 for micro-phase separation to occur has led to a surge in so-called high- χ , low- N block copolymers^[4] that target nano-patterns with minimum periodicities and therefore maximum feature densities.^[5,6] Unfortunately, an immiscibility-driven approach will not suffice when sub-5 nm periodicities are desired,^[4] preventing extendibility to smaller dimensions. In addition, although the assembly of block copolymers can be directed within a photolithographic pre-pattern,^[7] the formation of defect-free periodic structures remains a challenge.^[8]

For sub-5 nm periodicities, monodisperse small molecules such as liquid crystals have been proposed (see chapter 1).^[4] Liquid crystals (LC) can form similar phases as reported for block copolymers, such as smectic (lamellar) or discotic (cylindrical) morphologies.^[9] Therefore, LCs could operate beyond the scaling limits of block copolymers for nano-patterning applications, provided they can bear substantial etch selectivity. Liquid crystals have the advantage that they can be easily aligned into defect free structures, by for example shear,^[10] photo-alignment layers,^[11] and mechanical alignment layers,^[12] though these methods are not generally applicable for thin films. As discussed in chapter 1, exciting work has been performed on the confinement of liquid crystals in structures such as micro-channels,^[13] nano-grooves,^[14] or nano-pores,^[15] but the directed self-assembly of thin films with sub 5 nm periodicities has not been reported.

In this chapter we explore oligo(dimethylsiloxane) (ODMS) liquid crystals^[10, 16, 17] as candidates for sub-5 nm nano-patterning. In these LCs the volume fraction of

flexible inorganic ODMS has been systematically varied in comparison to the organic mesogenic core, resulting in various sub-5 nm, hybrid organic/inorganic morphologies. We further examine the LC self-assembly in thin films and demonstrate the compatibility of the ODMS LCs with grapho-epitaxy, where ordered nano-patterns are achieved without additional annealing.



Scheme 1. Synthetic scheme for the preparation of the ODMS liquid crystals, where *n* represents the length of the ODMS tail: **LC-14Si** (*n* = 5), **LC-22Si** (*n* = 9), **LC-30Si** (*n* = 13).

2.2. Results & Discussion

The synthetic scheme for the preparation of the ODMS liquid crystals is depicted in Scheme 1. A four-ring rigid core (**C**) was synthesized by reaction of 4-(butenyloxy)benzoic acid (**A**) with 4, 4'-dihydroxy azobenzene (**B**) in an esterification reaction with dicyclohexylcarbodiimide (DCC) and 4-dimethylaminopyridine (DMAP).^[18] Oligo(dimethylsiloxane)s were prepared in the group of Meijer by coupling

a linear trisiloxane to a linear chlorotetrasiloxane in an iterative fashion,^[19] producing a heptasiloxane monohydride (first cycle), an undecasiloxane monohydride (second cycle), and pentadecasiloxane (third cycle). Subsequently, the respective ODMS hydrides (**D**) were coupled to the core, using Karstedt's catalyst. The conversion of Si-H bond to Si-C bond was examined by Fourier transform infrared spectroscopy (FT-IR), by following the disappearance of the Si-H absorption band at about 2130 cm^{-1} and C=C absorption at $1648\text{-}1640\text{ cm}^{-1}$. The molecular structure of the ODMS liquid crystals is depicted in Scheme 1, where n represents the length of the ODMS tail. ODMS tails consisting of 7 ($n = 5$), 11 ($n = 9$), and 15 ($n = 13$) dimethylsiloxane units were used, resulting in liquid crystals **LC-14Si**, **LC-22Si**, and **LC-30Si**, respectively. All LCs were purified and fully characterized.

To investigate the LC phase behavior, the LCs were analyzed by polarized optical microscopy (POM) and differential scanning calorimetry (DSC). The POM images (Figure 1) show birefringent multi-domains typical for liquid crystals and signify a correlation length of the nanostructures contained within the domains that is on the order of micrometers. DSC (Figure 2) shows the presence of mesophases marked by sharp order-disorder transitions. None of the compounds are found to crystallize. The room-temperature LC phases were further investigated by bulk X-ray diffraction (XRD) in both wide-angle and medium-angle configurations (Figure 1). For each liquid crystal, two broad peaks were observed in the wide-angle region ($5\text{ nm}^{-1} < q < 20\text{ nm}^{-1}$). The first, at $q = 9\text{ nm}^{-1}$ ($d = 0.70\text{ nm}$), is assigned to the mean distance between siloxane units.^[17] The second, at $q = 13.4\text{ nm}^{-1}$ ($d = 0.45\text{ nm}$), is assigned to the mean distance between the aliphatic and aromatic parts of the molecule. The presence of two distinct wide angle peaks evidences the nano-phase separation between the ODMS and organic molecular components. The medium angle reflections ($1\text{ nm}^{-1} < q < 5\text{ nm}^{-1}$) were used to assign the LC lattice parameters indicated in Figure 1. **LC-14Si** forms a rectangular columnar phase ($a = 3.8\text{ nm}$, $b = 7.4\text{ nm}$) (plane group $c2nm$). **LC-22Si** also forms a rectangular columnar phase ($a = 4.3\text{ nm}$, $b = 8.5\text{ nm}$) with a comparatively larger lattice. **LC-30Si** forms a hexagonal columnar phase ($a = 5.1\text{ nm}$) (plane group $p6nm$). This finding indicates the modularity of the LC approach, i.e. the pitch can be tuned by changing the length of the ODMS tail.

Schematic representations of the liquid crystal phases are included in Figure 1. In the columnar phases, the LC cylinder can be considered to consist of an arrangement of rigid rods with a cross section of approximately 2.4 nm ^[20] (red), while the matrix consists of flexible ODMS coils which fill the space between the cylinders^[21] (blue). The absence of an 'inter-disc distance' in the wide-angle region

reveals that the rigid cores are relatively unordered within the LC cylinders. The morphology change from the higher-order rectangular columnar phase to the lower-order hexagonal columnar phase is considered a consequence of the increased coil-to-rod volume fraction^[24, 22] in the LC series.

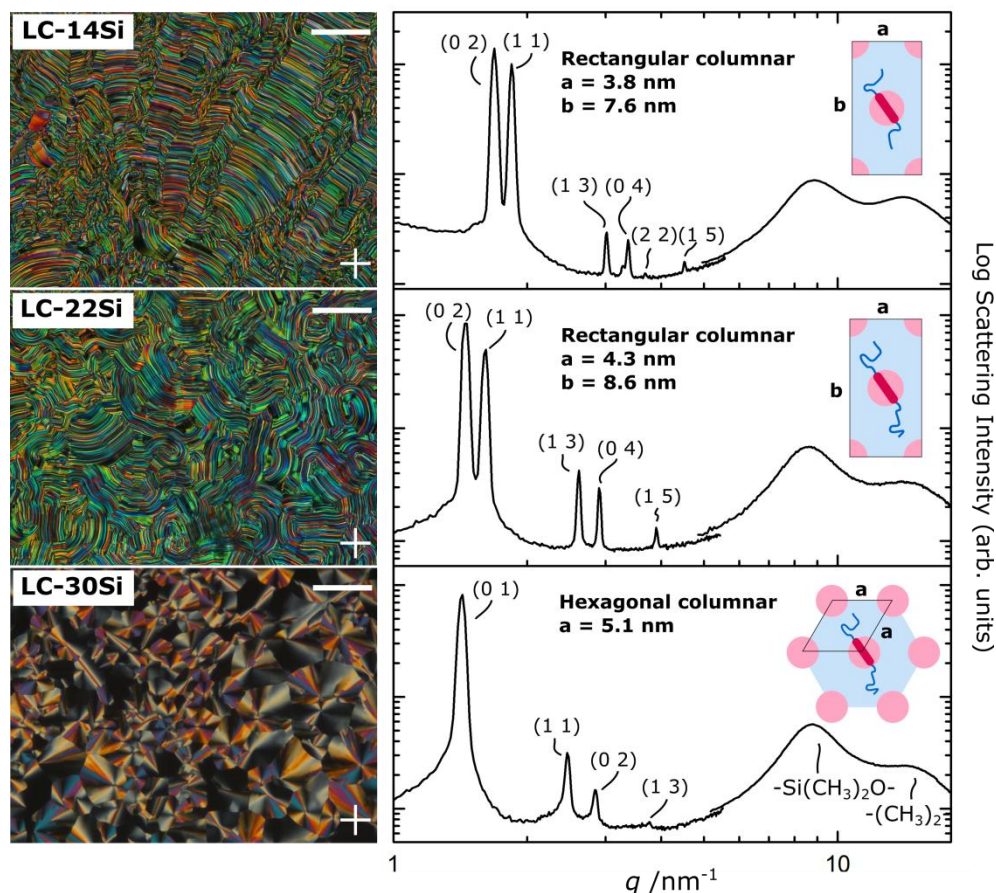


Figure 1. Room-temperature POM images of the ODMS liquid crystals and their corresponding XRD spectra. The POM images were obtained under crossed polarizers (polarizer axes are indicated in the images with a cross). All scale bars: $100 \mu\text{m}$. The XRD spectra were collected in both wide- and medium-angle configurations (the transition is marked by a discontinuity at $q \sim 5 \text{ nm}^{-1}$). The assigned Miller indices and the respective intermolecular scatterings are indicated, as well as the corresponding lattices.

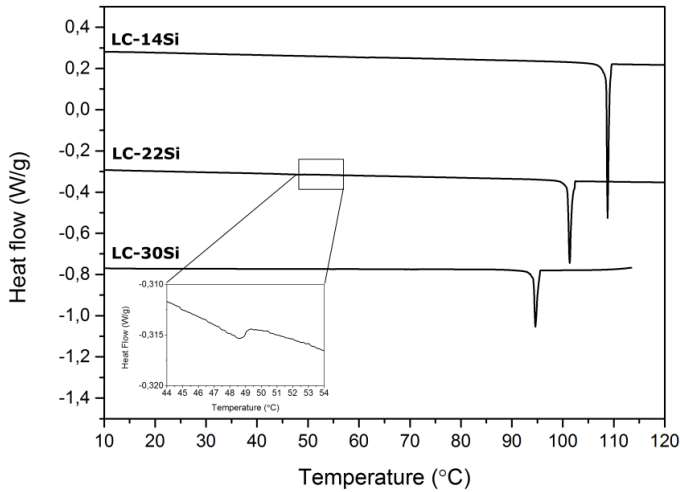


Figure 2. DSC cooling curves of second cooling ($10^{\circ}\text{C} / \text{min}$) of the ODMS liquid crystals.

In order to study the morphology of the LCs in thin films, solutions of LC were spin-coated on Si wafers modified with a PDMS polymer brush.^[3] Solutions of 1 wt % in heptane resulted in 40 nm thin films on top of a 4.5 nm brush layer, according to ellipsometry. AFM phase images of the thin films surface exhibit highly-ordered line features indicative of a planar orientation of LC cylinders (Figure 3). Since the surface energy of the ODMS tails is presumed to be very low ($\gamma_{\text{PDMS}} = 20.5 \text{ mN/m}$),^[23] the siloxane tails are anticipated to wet the air interface. Since the cylinder structures are buried inside the film, the contrast in AFM height and phase images is assumed to arise from the disparate mechanical properties of the rigid LC core and flexible ODMS tails in tapping mode (core = light, ODMS = dark). The center-to-center distances were determined by Fourier analysis. For the columnar rectangular phases of **LC-14Si** and **LC-22Si**, distances of 3.8 and 4.3 nm are found respectively, corresponding to lattice parameter 'a' in each case. Lattice parameter 'b' was not seen, suggesting a preferential orientation of the columnar lattice with 'a' parallel to the substrate and 'b' perpendicular to the substrate. The defect density in these as-cast, un-annealed films is remarkably low. At the same time, the orientation of the micro-domains is preserved over large distances, indicating a naturally large correlation length between the LC cylinders, in accordance with POM observations of bulk material.

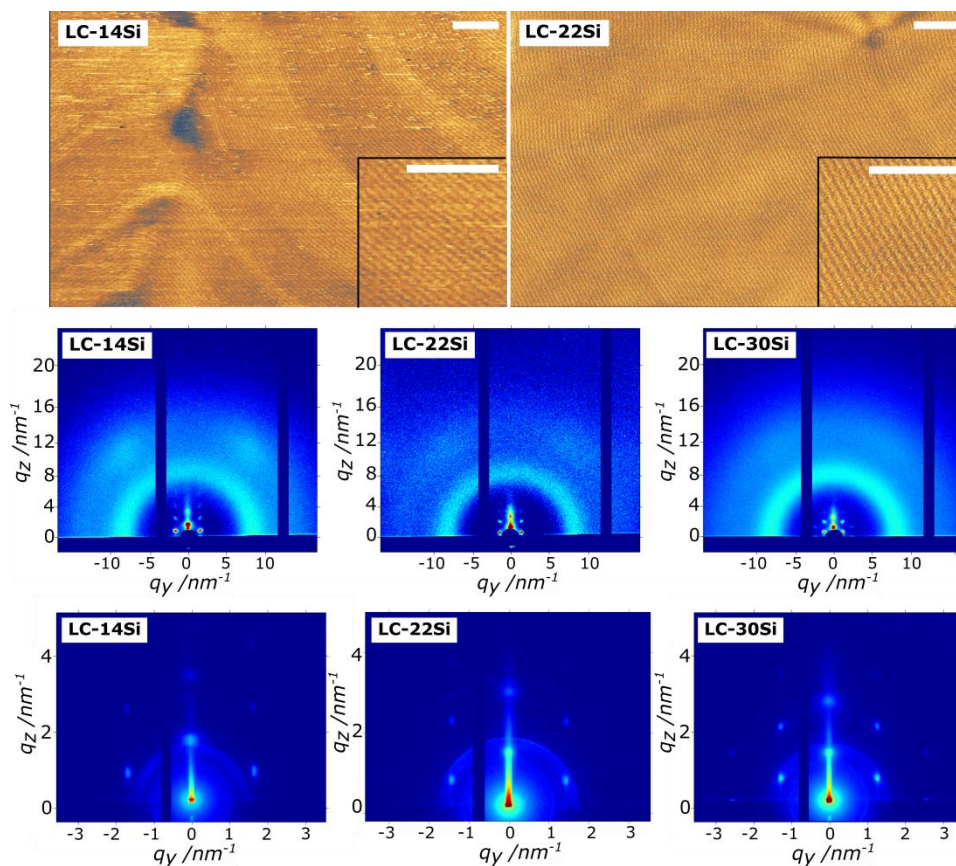


Figure 3. Characterization of as-cast ODMS LC thin films of thickness 40 nm. Top: AFM phase images exhibit line structures produced by in-plane LC cylinders (bright domains). Scale bars: 50 nm. Bottom: grazing-incidence x-ray diffraction data in wide-angle and medium-angle configurations, measured around the critical angle.

Grazing-incidence x-ray diffraction (GIXRD) was performed in both wide-angle and medium-angle configurations (Figure 3) to investigate the through-film morphology of the thin films. In line with bulk measurements, the broad reflections at $7 \text{ nm}^{-1} < q < 14 \text{ nm}^{-1}$ signify that the liquid-like nature of the respective intermolecular interactions (siloxane-siloxane and organic-organic) is maintained in the thin films. The medium-angle reflections were used to assign the LC lattice parameters. The observed distinct Bragg spots confirm the LC cylinders are oriented parallel to the substrate. For **LC-14Si**, the scattering data is fitted with a rectangular lattice ($a = 3.8 \text{ nm}$, $b = 7.4 \text{ nm}$, plane group $c2nm$). For **LC-22Si**, the scattering data is also fitted with a rectangular lattice ($a = 4.3 \text{ nm}$, $b = 8.5 \text{ nm}$, plane group $c2nm$). The rectangular lattices are oriented with their short axis 'a' parallel to the surface,

in line with AFM observations. For **LC-30Si**, the scattering data is fitted with an hexagonal lattice ($a = 5.1$ nm, plane group $p6nm$). In each case, the presence of higher order reflections is a sign of the high lateral order and large correlation lengths, in accordance with AFM. We argue that the LC nature of the film and absence of polydispersity are responsible for the high lateral order. Interestingly, the bulk and thin film periodicities correspond exactly. This finding stands in contrast with thin block copolymer films, where the periodicity typically increases by approximately 10 % from the bulk due to stretching of the polymer chains. [5, 24]

We further investigated the directed self-assembly of the LC in grapho-epitaxial trenches of approximately 100 nm in width, which were patterned with classical 193 nm immersion lithography and modified with a PDMS polymer brush. The patterned wafers were coated with a 1 wt % heptane solution of **LC-22Si**. AFM reveals multi-layers confined inside the trenches with the cylindrical long axis parallel to the trench walls (Figure 4). The trench is subdivided into 24 smaller line structures with a 4.3 nm periodicity (obtained from Fourier analysis). The high order is remarkable considering the absence of any annealing or further optimization of any kind, and clearly demonstrates the potential of using liquid crystals for the production of monolithic systems. However, the lithographic processes used to produce the trenches are imperfect which results in local variations of the trench width on the order of several nanometers.^[25] Apparent defects result from confinement of the LC by trench walls with nonzero roughness, which causes bending of the line structures, in addition to a few disclinations, however these are largely limited to the edge of each channel. ^[26] Given the low density of non-equilibrium defects in samples with no directing features (ca. 2 defects- μm^{-2} , based on Figure 3 and similar images), it is unlikely that such defects are present within the trenches. Other apparent defects are likely artefacts due to a combination of noise and row misalignment, given the small periodicity (4.3 nm) relative to the AFM resolution (1 pixel / nm). Furthermore, the LC periodicity does not fluctuate as it is fixed by the LC lattice parameters, and hence, the placement error is on the order of the trench roughness.^[27] For pattern registration, further roughness reduction could be achieved with an optimized photolithographic step or by a next generation extreme-UV lithographical tool.

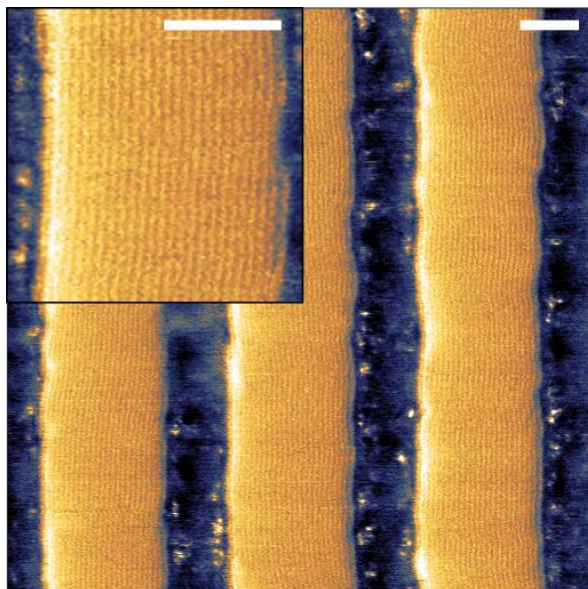


Figure 4. AFM phase image of as-cast **LC-22Si** thin film within grapho-epitaxial trenches of approximately 100 nm width. Highly-ordered line structures are formed with a period of 4.3 nm. The inset corresponds to a 2x magnification. Scale bars: 50 nm.

The next steps toward liquid crystal based nanolithography are first, the casting of single layer films, and then pattern transfer of the ODMS nano-patterns by etching. AFM experiments show that uniform thin films can be prepared in which the LC morphology is maintained by adjusting the spin-coating concentration (Figure 5). At concentrations below 1.00 gL^{-1} , islands are formed with uniform height of approximately 7.2 – 8.0 nm. At 1.00 gL^{-1} , a near-complete layer is formed (coverage 95%). At higher concentrations, a second layer is formed alongside the first layer (1.25 gL^{-1} , 1.50 gL^{-1} , 1.75 gL^{-1}). The thickness of the second layer is approximately 3.3 - 3.9 nm. At 2.50 gL^{-1} , a third layer is formed. The thickness of the third LC layer is approximately 4.3 nm, which is equal to the bulk periodicity.

These findings are confirmed by medium-angle grazing incidence x-ray diffraction experiments (Figure 6). At a concentration of 1.00 gL^{-1} , a single reflection is present perpendicular to the substrate at $q = 1.48 \text{ nm}^{-1}$ (4.25 nm), which is identified as the scattering from a single layer of in-plane LC cylinders. This reflection is referenced as the (2 0) reflection in the rectangular columnar lattice, although this lattice cannot strictly be applied to a 1D system. At higher concentrations (1.25 gL^{-1} , 2.50 gL^{-1}), the out-of-plane (1 1), (0 2), and (1 3) reflections appear, indicative of the formation of LC-multilayers, in accordance with AFM findings (Figure 5).

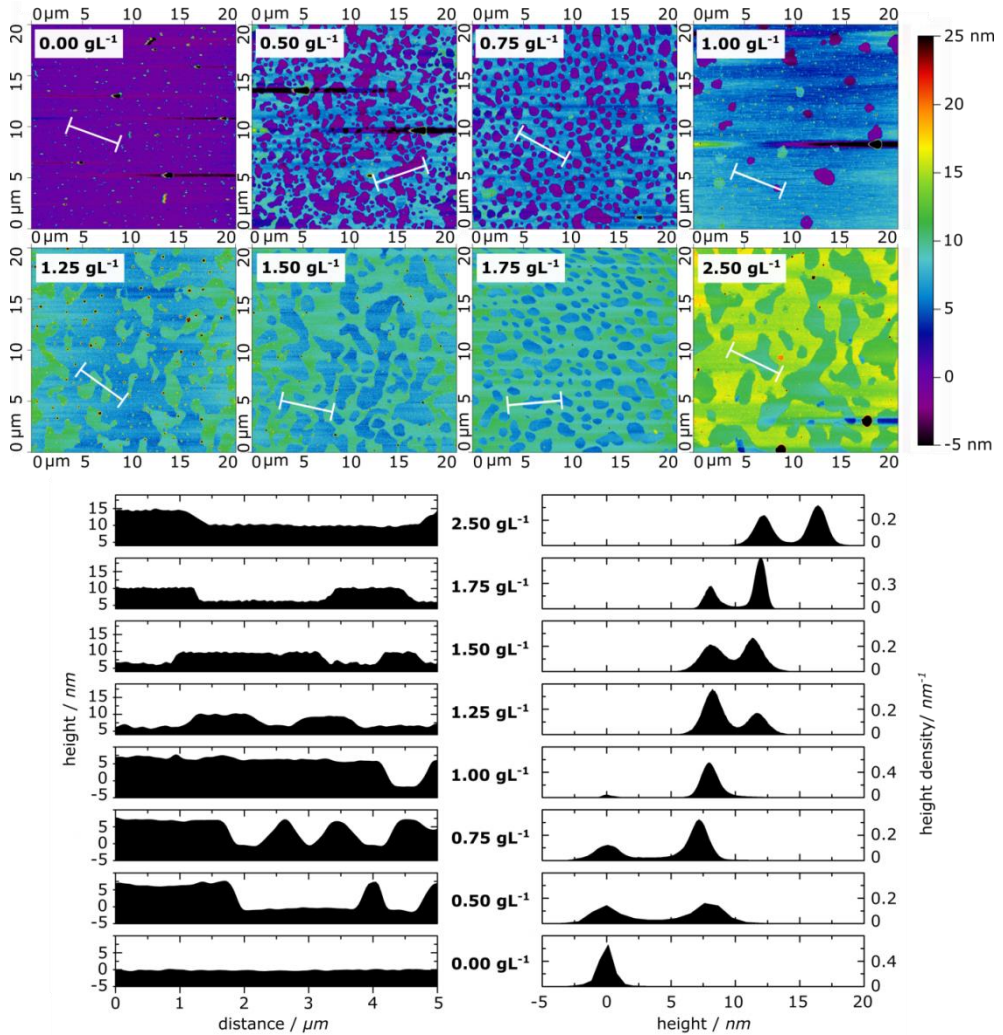


Figure 5: AFM height images of LC-22Si thin films (top) spin-coated at varying concentrations, with corresponding height profiles (bottom left) and height density maps (bottom right). The height profiles are indicated by a white line in the AFM images.

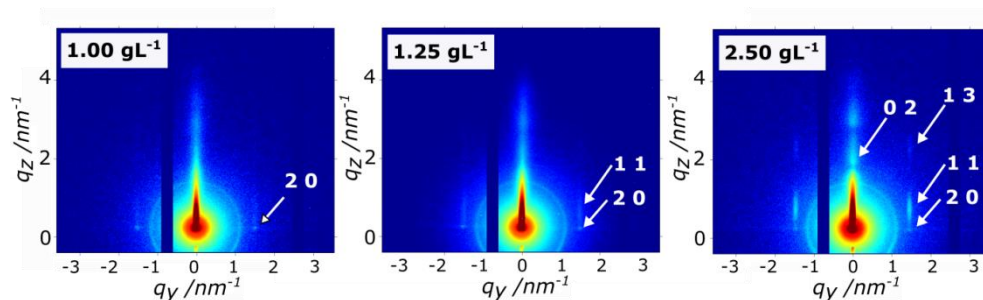


Figure 6. Medium-angle grazing incidence x-ray diffraction data of **LC-22Si** thin films cast at various concentrations. The samples were measured at the critical angle with a sample detector distance of 491 mm.

Preliminary oxygen plasma etching experiments on a multilayer film indicate that the organics are etched away while the ODMS is oxidized (Figure 7), demonstrating the potential of these liquid crystals for nanolithography. The etched sample was exposed to 10 seconds of plasma produced by 20W RF (100% O_2). The mass concentration percentages of an un-etched and etched **LC-22Si** thin film were determined via X-ray photoelectron spectroscopy. Upon etching, the carbon mass concentration is decreased while the oxygen concentration is increased, signifying the etching of organic material. Furthermore, methyl-bound silicon oxidizes into oxygen-bound silicon, indicating the formation of silicon oxides. While the limited aspect ratio of the in-plane cylinders in combination with the nanoscopic dimensions will undoubtedly impose extensive optimization of etching parameters for pattern transfer, the materials described in this chapter open up a promising avenue for the production of sub-5 nm inorganic features.

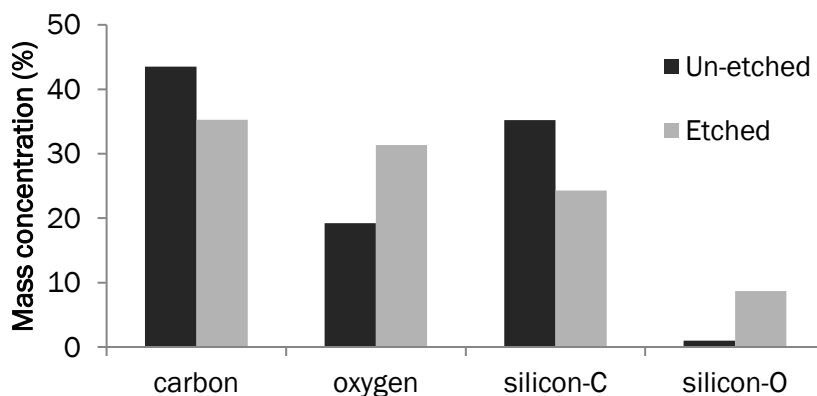


Figure 7. Mass concentration percentages of an un-etched and etched **LC-22Si** thin film determined via X-ray photoelectron spectroscopy.

2.3. Conclusion

In this chapter, we have introduced oligo(dimethylsiloxane) liquid crystals as candidates for sub-5 nm nano-patterning. The ease with which these materials align by grapho-epitaxial templates bears witness to the benefit of using liquid crystals for obtaining ultra-small, highly-ordered nano-patterns. In perspective, the use of liquid crystals could provide a real advantage over block copolymers not only in feature size, but also by the lack of variations in domain-size and periodicity in thin films versus bulk and across a trench.^[28]

2.4. Materials & Methods

All reagents were used as received. The ODMS materials were received from the group of Meijer. All solvents were of AR quality and purchased from Biosolve. Dry DCM was tapped off a distillation setup which contained molecular sieves. Reactions were followed by thin-layer chromatography (pre-coated 0.25 mm, 60-F254 silica gel plates from Merck). The LC compositions were identified by ¹H NMR and ¹³C NMR on a Varian Mercury Vx 400 MHz (100 MHz for ¹³C NMR) spectrometer. Deuterated chloroform (CDCl₃) and tetramethylsilane (TMS) were used as solvent and internal standard, respectively. Matrix-assisted laser desorption/ionization mass spectra were obtained on a PerSeptive Biosystems Voyager DE-PRO spectrometer or a Bruker autoflex speed spectrometer using α -cyano-4-hydroxycinnamic acid (CHCA) and 2-[(2E)-3-(4-tert-butylphenyl)-2-methylprop-2-enylidene]malononitrile (DCTB) as matrices. Temperature stability was evaluated by thermal gravimetric analysis (TGA). For the POM measurements, a small amount of LC material was placed between microscope slides, heated to the isotropic phase, and cooled (10 °C / min) to room temperature by a hot-stage (Linkam, THMS600) coupled to a polarized optical microscope (POM) (Leica DM6000M), equipped with a DFC420C camera. X-ray scattering measurements were performed on a Ganesha lab instrument equipped with a GeniX-Cu ultralow divergence source producing X-ray photons with a wavelength of 1.54 Å and a flux of 1x10⁸ phs⁻¹. Scattering patterns were collected using a Pilatus 300 K silicon pixel detector. The beam center and the q range were calibrated using the diffraction peaks of silver behenate. Bulk XRD was performed on samples sealed in a 1mm glass capillary. Grazing incidence XRD was performed at the critical angle (~ 0.18°). The sample to detector distance was 91 mm for wide-angle measurements and 441 mm for medium-angle measurements. The AFM data were recorded in ambient conditions using a Dimension ICON atomic force microscope (Bruker Nano Inc., Santa Barbara, CA) fitted with an NCHV silicon probe (Bruker, spring constant 42 N/m and a resonance frequency 320 kHz). The AFM

images were all captured on films without any etching, so a thin wetting layer of ODMS is presumably at the air-LC interface. For thin film preparation, a hydroxy-terminated PDMS homopolymer from Polymer Source with molecular weight 5 kg/mol was applied onto templated or untemplated silicon substrates from a 1-2 wt. % solution in heptane, baked at 150 °C for at least 24h, and rinsed with heptane. The liquid crystals were subsequently spin-coated from 1 wt. % solution in heptane (3000 RPM, 45s). For the fabrication of the trenches, spin-on carbon (SOC) HM710 and spin-on glass (SOG) ISX304 from JSR Micro were used with vendor recommended process conditions. Negative tone development photoresist ANO2 from FUJIFILM was patterned on this stack using an ASML NXT:1950i ArF immersion scanner with moderate off-axis illumination conditions (1.2NA, annular illumination, $\sigma_o/\sigma_i = 0.8/0.6$). The resist patterns were transferred into the SOC using a TEL Tactras™ dry etch system and the SOG was removed using 0.5% HF on a TEL CELLESTA™ wafer clean system. Oxygen plasma etching was performed with an Emitech K1050X RF plasma reactor operating in plasma ashing mode. The XPS measurements were carried out with a Thermo Scientific K-Alpha, equipped with a monochromatic small-spot X-ray source and a 180° double focusing hemispherical analyzer with a 128-channel detector. The spectra were obtained using an aluminium anode (Al K α = 1486.6 eV) operating at 72W and a spot size of 400 μ m. Ellipsometric measurements were acquired via nulling ellipsometry using a spectroscopic imaging ellipsometer (Accurion Nanofilm ep4, Accurion GmbH, Göttingen, Germany) fit with a 10 \times objective ($\sim 2 \mu$ m lateral resolution). Data was collected at angles from 50° to 70° at selected wavelengths from 350 to 1000 nm. The data were modelled based on sequential measurements of the thermal oxide (~ 2 nm) on Si(100), the PDMS brush (~ 5 nm), and various layers of LC-22Si.

2.5. Synthetic procedures

To a 100mL three-necked flask were added 1 eq. (750 mg) 4-butenyloxybenzoic acid (**A**), 1.1 eq. of *N,N'*-dicyclohexylcarbodiimide (DCC) and 0.07 eq. of 4-dimethylaminopyridine (DMAP). After 30 min of stirring and purging with argon, 10 mL of anhydrous dichloromethane (DCM) were added. In a separate 25 mL flask, 0.5 eq. of (*E*)-4,4'-dihydroxy-azobenzene (**B**) was dissolved in 10 mL of anhydrous THF under argon atmosphere, and the solution was transferred by canula to the first flask. The reaction was stirred at room temperature for 5 h until TLC (SiO₂, DCM) indicated that reaction was complete. The urea derivative was filtered off, the reaction mixture was diluted with 2 M KOH, and extracted with DCM. The combined organic layers were dried over anhydrous magnesium sulphate, filtered and evaporated. The residue was recrystallized from DCM to yield **C**. A Schlenk flask was charged with 1

eq. (100 mg) of **C** and 2.2 eq. siloxanemonohydride (**D**) and put under an Argon atmosphere. Subsequently dry DCM (5 mL) and drop of Karstedt's catalyst (1% in xylene) were added. The solution was stirred overnight at room temperature. The reaction was quenched in methanol and the reaction product was purified using column chromatography (eluent: heptane/ethyl acetate) to offer the desired product.

(E)-diazene-1,2-diylbis(4,1-phenylene) bis(4-(but-3-en-1-yloxy)benzoate). (C)

Orange powder, yield: 40%; $^1\text{H-NMR}$ (400 MHz, CDCl_3): δ 8.16 (d, 4H); 8.00 (d, 4H); 7.39 (d, 4H); 7.00 (d, 4H); 4.06 (m, 4H); 1.86 (m, 4H); 0.63 (m, 4H); 0.13-0.01 (m, 138H); $^{13}\text{C-NMR}$ (100 MHz, CDCl_3): δ 164.6, 163.7, 153.1, 150.1, 132.3, 124.1, 122.4, 121.2, 114.4, 68.0, 32.6, 29.7, 19.7, 18.0, 1.82, 1.28; MALDI-TOF MS (m/z): $[\text{M}+\text{H}]^+$ calcd for $\text{C}_{34}\text{H}_{30}\text{N}_2\text{O}_6$ 563.21, found 563.22.

(E)-diazene-1,2-diylbis(4,1-phenylene)bis(4-(4-(1,1,3,3,5,5,5-heptamethyltrisiloxanyl)butoxy)benzoate) (LC-6Si)

Orange paste: yield 26%. $^1\text{H NMR}$ (400 MHz, CDCl_3 , δ in ppm: 8.16 (d, 4H); 8.00 (d, 4H); 7.39 (d, 4H); 7.00 (d, 4H); 4.06 (m, 4H); 1.86 (m, 4H); 0.63 (m, 4H); 0.13-0.01 (m, 42H). $^{13}\text{C NMR}$ (400 MHz, CDCl_3 , δ in ppm): 164.6, 163.7, 153.1, 150.1, 132.3, 124.1, 122.4, 121.2, 114.4, 68.0, 32.6, 29.7, 19.7, 18.0, 1.82, 1.28. MALDI-TOF MS: $[\text{M}+\text{Na}]^+$ calcd for $\text{C}_{48}\text{H}_{74}\text{N}_2\text{O}_{10}\text{Si}_6$ 1029.39, found 1029.49.

(E)-diazene-1,2-diylbis(4,1-phenylene)bis(4-(4-1,1,3,3,5,5,7,7,9,9,11,11,13,13,13-pentadecamethylheptasiloxanyl)butoxy)benzoate) (LC-14Si)

Orange paste, yield: 89%; $^1\text{H-NMR}$ (400 MHz, CDCl_3 , δ 8.16 (d, 4H); 8.00 (d, 4H); 7.39 (d, 4H); 7.00 (d, 4H); 4.06 (m, 4H); 1.86 (m, 4H); 0.63 (m, 4H); 0.13-0.01 (m, 90H); $^{13}\text{C-NMR}$ (100 MHz, CDCl_3): δ 164.6, 163.7, 153.1, 150.1, 132.3, 124.1, 122.4, 121.2, 114.4, 68.0, 32.6, 29.7, 19.7, 18.0, 1.82, 1.28; MALDI-TOF MS (m/z): $[\text{M}+\text{Na}]^+$ calcd for $\text{C}_{64}\text{H}_{122}\text{N}_2\text{O}_{18}\text{Si}_{14}$ 1621.54, found 1621.56.

(E)-diazene-1,2-diylbis(4,1-phenylene)bis(4-(4-(1,1,3,3,5,5,7,7,9,9,11,11,13,13,15,15,17,17,19,19,21,21,21-tricosamethylundecasiloxanyl)butoxy)benzoate) (LC-22Si)

Orange paste, yield: 84%; $^1\text{H-NMR}$ (400 MHz, CDCl_3): δ 8.16 (d, 4H); 8.00 (d, 4H); 7.39 (d, 4H); 7.00 (d, 4H); 4.06 (m, 4H); 1.86 (m, 4H); 0.63 (m, 4H); 0.13-0.01 (m, 138H); $^{13}\text{C-NMR}$ (100 MHz, CDCl_3): δ 164.6, 163.7, 153.1, 150.1, 132.3, 124.1, 122.4, 121.2, 114.4, 68.0, 32.6, 29.7, 19.7, 18.0, 1.82, 1.28; UV/Vis: λ_{max} 330 nm; MALDI-TOF MS (m/z): $[\text{M}+\text{Na}]^+$ calcd for $\text{C}_{80}\text{H}_{170}\text{N}_2\text{O}_{26}\text{Si}_{22}$ 2213.69, found 2213.71.

(E)-diazene-1,2-diylbis(4,1-phenylene)bis(4-(4-(1,1,3,3,5,5,7,7,9,9,11,11,13,13,15,15,17,17,19,19,21,21,23,23,25,25,27,27,29,29-hentriacontamethylpentadecasiloxanyl)butoxy)benzoate) (LC-30Si)

Orange paste, yield: 69%; $^1\text{H-NMR}$ (400 MHz, CDCl_3), δ 8.16 (d, 4H); 8.00 (d, 4H); 7.39 (d, 4H); 7.00 (d, 4H); 4.06 (m, 4H); 1.86 (m, 4H); 0.63 (m, 4H); 0.13-0.01 (m, 186H); $^{13}\text{C-NMR}$ (100 MHz, CDCl_3): δ 164.6, 163.7, 153.1, 150.1, 132.3, 124.1, 122.4, 121.2, 114.4, 68.0, 32.6, 29.7, 19.7, 18.0, 1.82, 1.28; MALDI-TOF MS (m/z): $[\text{M}+\text{Na}]^+$ calcd for $\text{C}_{96}\text{H}_{218}\text{N}_2\text{O}_{34}\text{Si}_{30}$ 2805.84, found 2805.86.

2.6. References

- [1] a) A. Nunns, J. Gwyther, I. Manners, *Polymer* **2013**, *54*, 1269; b) J. D. Cushen, I. Otsuka, C. M. Bates, S. Halila, S. Fort, C. Rochas, J. A. Easley, E. L. Rausch, A. Thio, R. Borsali, C. G. Willson, C. J. Ellison, *ACS Nano* **2012**, *6*, 3424; c) X. Yu, K. Yue, I. F. Hsieh, Y. Li, X. H. Dong, C. Liu, Y. Xin, H. F. Wang, A. C. Shi, G. R. Newkome, R. M. Ho, E. Q. Chen, W. B. Zhang, S. Z. Cheng, *Proc. Natl. Acad. Sci. USA* **2013**, *110*, 10078.
- [2] a) Y. S. Jung, J. B. Chang, E. Verploegen, K. K. Berggren, C. A. Ross, *Nano Lett.* **2010**, *10*, 1000; b) M. L. Wadey, I. F. Hsieh, K. A. Cavicchi, S. Z. D. Cheng, *Macromolecules* **2012**, *45*, 5538; c) C. C. Chao, T. C. Wang, R. M. Ho, P. Georgopoulos, A. Avgeropoulos, E. L. Thomas, *ACS Nano* **2010**, *4*, 2088.
- [3] Y. S. Jung, C. A. Ross, *Nano Lett.* **2007**, *7*, 2046.
- [4] C. Sinturel, F. S. Bates, M. A. Hillmyer, *ACS Macro Lett.* **2015**, *4*, 1044.
- [5] Y. Luo, D. Montarnal, S. Kim, W. Shi, K. P. Barteau, C. W. Pester, P. D. Hustad, M. D. Christianson, G. H. Fredrickson, E. J. Kramer, C. J. Hawker, *Macromolecules* **2015**, *48*, 3422; [6] a) J. W. Jeong, W. I. Park, M.-J. Kim, C. A. Ross, Y. S. Jung, *Nano Lett.* **2011**, *11*, 4095; b) L. M. Pitet, S. F. Wuister, E. Peeters, E. J. Kramer, C. J. Hawker, E. W. Meijer, *Macromolecules* **2013**, *46*, 8289.
- [7] M. Luo, T. H. Epps, *Macromolecules* **2013**, *46*, 7567.
- [8] H. Pathangi, B. T. Chan, H. Bayana, N. Vandenbroeck, D. Van den Heuvel, L. Van Look, P. Rincon-Delgadillo, Y. Cao, J. Kim, G. Y. Lin, D. Parnell, K. Nafus, R. Harukawa, I. Chikashi, M. Polli, L. D'Urzo, R. Gronheid, P. Nealey, *J. Micro-Nanolith. Mem.* **2015**, *14*.
- [9] a) M. Lee, B. K. Cho, Y. G. Jang, W. C. Zin, *J. Am. Chem. Soc.* **2000**, *122*, 7449; b) C. Keith, R. A. Reddy, A. Hauser, U. Baumeister, C. Tschierske, *J. Am. Chem. Soc.* **2006**, *128*, 3051; c) C. Tschierske, *Curr. Opin. Colloid. In. Sci.* **2002**, *7*, 69; d) C. Tschierske, *J. Mater. Chem.* **2001**, *11*, 2647; f) Q. Zhou, T. Chen, J. Zhang, L. Wan, P. Xie, C. C. Han, S. Yan, R. Zhang, *Tetrahedron Lett.* **2008**, *49*, 5522; g) M. Zhou, T. J. Kidd, R. D. Noble, D. L. Gin, *Adv. Mater.* **2005**, *17*, 1850; h) X. D. Feng, M. E. Tousley, M. G.

- Cowan, B. R. Wiesenauer, S. Nejati, Y. Choo, R. D. Noble, M. Elimelech, D. L. Gin, C. O. Osuji, *Acs Nano* **2014**, *8*, 11977.
- [10] R. H. Zha, B. F. de Waal, M. Lutz, A. J. Teunissen, E. W. Meijer, *J. Am. Chem. Soc.* **2016**, *138*, 5693.
- [11] a) T. Seki, S. Nagano, M. Hara, *Polymer* **2013**, *54*, 6053; b) A. Natansohn, P. Rochon, *Chem Rev* **2002**, *102*, 4139; c) T. Ikeda, *J. Mater. Chem.* **2003**, *13*, 2037.
- [12] J. C. Wittmann, P. Smith, *Nature* **1991**, 352, 414.
- [13] J. Cattle, P. Bao, J. P. Bramble, R. J. Bushby, S. D. Evans, J. E. Lydon, D. J. Tate, *Adv. Funct. Mater.* **2013**, *23*, 5997.
- [14] P. O. Mouthuy, S. Melinte, Y. H. Geerts, A. M. Jonas, *Nano Lett.* **2007**, *7*, 2627.
- [15] a) C. V. Cerclier, M. Ndao, R. Busselez, R. Lefort, E. Grelet, P. Huber, A. V. Kityk, L. Noirez, A. Schonhals, D. Morineau, *J. Phys. Chem. C* **2012**, *116*, 18990; b) R. B. Zhang, X. B. Zeng, B. Kim, R. J. Bushby, K. Shin, P. J. Baker, V. Percec, P. Leowanawat, G. Ungar, *ACS Nano* **2015**, *9*, 1759.
- [16] a) C. Pugh, J. Y. Bae, J. Dharia, J. J. Ge, S. Z. D. Cheng, *Macromolecules* **1998**, *31*, 5188; b) L. Wang, Y. Ishida, R. Maeda, M. Tokita, S. Horiuchi, T. Hayakawa, *Langmuir* **2014**, *30*, 9797; c) E. Nishikawa, E. T. Samulski, *Liq. Cryst.* **2000**, *27*, 1457.
- [17] C. Keith, R. A. Reddy, U. Baumeister, C. Tschierske, *J. Am. Chem. Soc.* **2004**, *126*, 14312.
- [18] a) J. Garcia-Amoros, A. Szymczyk, D. Velasco, *Phys. Chem. Chem. Phys.* **2009**, *11*, 4244; b) A. Sanchez-Ferrer, A. Merekalov, H. Finkelmann, *Macromol. Rapid Commun.* **2011**, *32*, 671.
- [19] B. van Genabeek, B. F. M. de Waal, M. M. J. Gosens, L. M. Pitet, A. R. A. Palmans, E. W. Meijer, *J. Am. Chem. Soc.* **2016**, *138*, 4210.
- [20] J. Garcia-Amoros, A. Szymczyk, D. Velasco, *Phys. Chem. Chem. Phys.* **2009**, *11*, 4244.
- [21] M. Lee, B. K. Cho, H. Kim, J. Y. Yoon, W. C. Zin, *J. Am. Chem. Soc.* **1998**, *120*, 9168.
- [22] E. Nishikawa, E. T. Samulski, *Liq. Cryst.* **2000**, *27*, 1463.
- [23] S. Wu, *Polymer Handbook*, Vol. VI, Wiley-Interscience, New York, USA **1989**.
- [24] K. Aissou, M. Mumtaz, G. Fleury, G. Portale, C. Navarro, E. Cloutet, C. Brochon, C. A. Ross, G. Hadziioannou, *Advanced materials* **2015**, *27*, 261.
- [25] B. Kim, N. Laachi, K. T. Delaney, G. H. Fredrickson, *Proc. SPIE 9049, Alternative Lithographic Technologies VI* **2014**, 9049.
- [26] a) Q. Tong, Q. Zheng, S. J. Sibener, *Macromolecules* **2014**, *47*, 4236; b) J. Chai, J. M. Buriak, *ACS Nano* **2008**, *2*, 489.
- [27] a) S. G. Xiao, X. M. Yang, *J. Vac. Sci. Technol. B.* **2007**, *25*, 1953; b) H. Boots, J. M. de Ruiter, T. T. Nguyen, A. Brizard, E. Peeters, S. F. Wuister, T. S. Druzhinina, J. K. Wolterink, J. G. E. M. Fraaije, *J. Micro-Nanolith. Mem.* **2014**, *13*; c) J. Y. Cheng, A. M. Mayes, C. A. Ross, *Nat. Mater.* **2004**, *3*, 823.

- [28] a) C. M. Bates, T. Seshimo, M. J. Maher, W. J. Durand, J. D. Cushen, L. M. Dean, G. Blachut, C. J. Ellison, C. G. Willson, *Science* **2012**, 338, 775; b) E. Kim, W. Kim, K. H. Lee, C. A. Ross, J. G. Son, *Adv. Funct. Mater.* **2014**, 24, 6981. J. G. Son, K. W. Gotrik, C. A. Ross, *ACS Macro Lett.* **2012**, 1, 1279.

Chapter 3

Smectic oligo(dimethylsiloxane) liquid crystal for sub-5 nm patterning

Abstract. A monodisperse oligo(dimethylsiloxane) liquid crystal is synthesized via hydrosilylation and characterized. The formation of a tilted smectic phase with a periodicity of approximately 3.0 nm is demonstrated via differential scanning calorimetry, polarized optical microscopy, and x-ray diffraction. Wide-angle x-ray diffraction was used to construct temperature dependent hypothetical packing models for the smectic phase (21 – 137 °C). We show that the layer spacing is relatively temperature independent across the smectic phase (~1% variation), but the director tilt is highly temperature dependent (20° - 70°). Finally, we show that the liquid crystal forms lamellar sheets in thin films.

This chapter is based on:

K. Nickmans, A. P. H. J. Schenning, Proc. SPIE 10125, Emerging Liquid Crystal Technologies XII 2017, 1012513

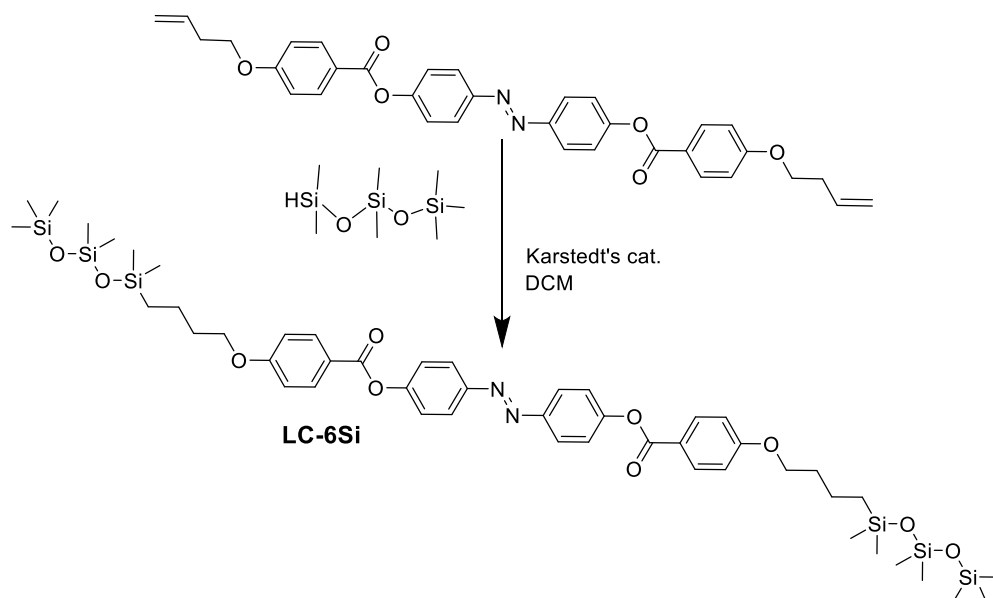
3.1. Introduction

As discussed in Chapter 1, the directed self-assembly of block copolymers has established itself as a powerful resolution enhancement technique to optical lithography.^[1,2] Block copolymers are known to form various phases depending on their relative block lengths, such as lamellar or hexagonal. Lamellar phases can be used to pattern dense line spaces,^[1,2] while hexagonal phases are typically employed for the patterning of contact holes.^[3] Unfortunately, the minimum domain spacing that can be obtained using typical block copolymer self-assembly does not exceed 10 nm.^[4] For next-generation directed self-assembly, particularly in combination with EUV, materials are required that can form ordered structures on the molecular length scale (1-10 nm).

Chapter 2 describes the directed self-assembly of a series of ODMS based liquid crystals (14 – 30 dimethylsiloxane units per molecule), which form columnar hexagonal and columnar rectangular phases with periodicities between 3.7 and 5.1 nm. The formation of columnar phases was promoted by the large volume fraction of bulky ODMS chains.^[5,6] In contrast, short siloxane tails (2 – 5 siloxane units per molecule) have been known to induce smectic phases.^[7-13] In this chapter, we report on a novel liquid crystal, **LC-6Si**, which contains six dimethylsiloxane repeating units (Scheme 1). Here we report the thermotropic phase behavior of **LC-6Si** and propose a tilted lamellar (SmC) packing with a periodicity of 3.0 nm. We further demonstrate that the liquid crystal forms lamellar thin films.

3.2. Results & Discussion

The oligo(dimethylsiloxane) liquid crystal **LC-6Si** was prepared by synthesizing an alkyl-terminated azobenzene core^[14] (Chapter 2) and coupling a commercially available, monodisperse, linear trisiloxane monohydride (Scheme 1). The reaction was carried out under standard hydrosilylation conditions using Karstedt's catalyst. After work-up and purification **LC-6Si** was fully characterized. The full synthetic procedures and characterization are provided in the experimental section. A few mg of **LC-6Si** were heated from room temperature to 800 °C in a TA 500 thermal gravitational analysis (TGA) instrument, at a rate of 10 °C min⁻¹, using an air atmosphere (Figure 1). At 800 °C, approximately 10 wt% of material remains which suggest the formation of inorganic silicon oxides by calcination.



Scheme 1. Synthetic scheme for the preparation of **LC-6Si**.

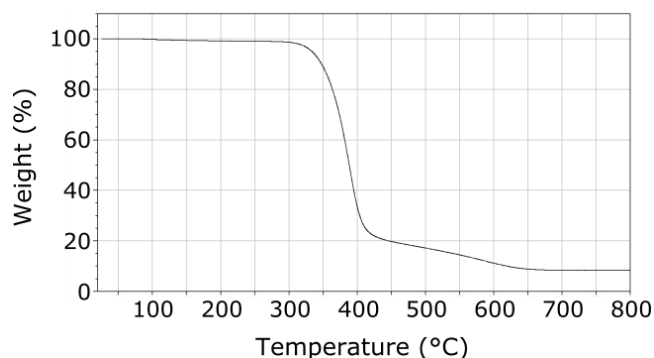


Figure 1. TGA experiment in air of **LC-6Si**.

To investigate the thermotropic phase behavior, **LC-6Si** was analyzed by differential scanning calorimetry (DSC), polarized optical microscopy (POM), and bulk X-ray diffraction (XRD). Figure 2 shows the DSC data obtained from the second cooling of the compound. The phase transition temperatures are I \rightarrow 137.3 °C (4.59 J g⁻¹) \rightarrow S_c \rightarrow 21.7 °C (1.14 J g⁻¹) \rightarrow K' \rightarrow 3.35 °C (7.59 J g⁻¹) \rightarrow K. Here, K, K', S_c, and I denote the crystalline, pre-crystalline, smectic C, and isotropic phases, respectively, and the associated enthalpy changes are given in parentheses. **LC-6Si** has a broad smectic LC temperature window, most likely promoted by partial phase

segregation of the ODMS tails (vide infra).^[10] Figure 2b shows POM images under crossed polarizers, taken after cooling **LC-6Si** from the isotropic phase. Just under the isotropic transition (137 °C), a fingerprint texture is observed. The birefringent domains are large. This signifies a large degree of lateral order and is significant for nanofabrication. The phase transitions into the K' and K phases are marked by an observable change in texture.

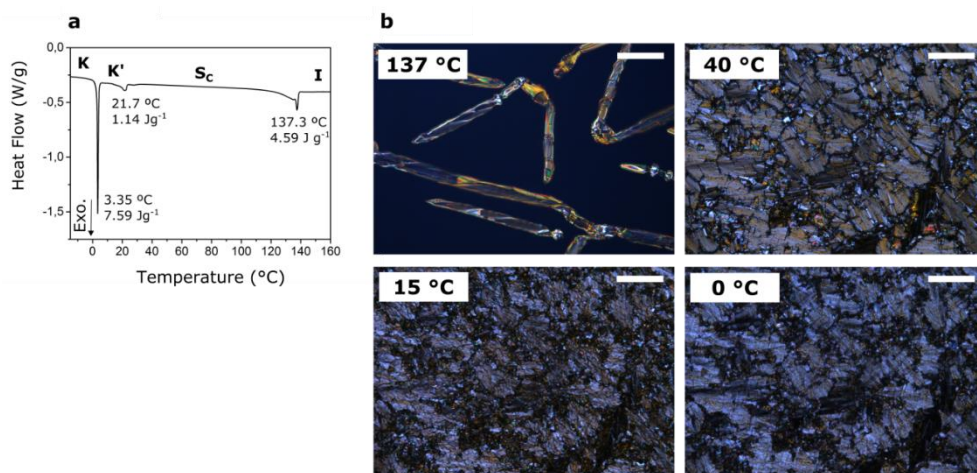


Figure 2. Thermal characterization of **LC-6Si**: DSC trace upon second cooling (a) and selected POM images taken between crossed polarizers at different temperatures (b). Scale bars: 200 μm .

In order to investigate the LC nanostructure and determine the lattice parameters, temperature dependent X-ray diffraction experiments were performed. To this end, **LC-6Si** was cooled in a magnetic field (1T) and a scattering profile was obtained at various temperatures. Figure 3 shows representative 2D diffractograms (a) and the associated reduced scattering profiles (b). In the isotropic phase (164 °C), two broad diffraction peaks are found. The first, centered at $q = 2.0 \text{ nm}^{-1}$ ($d = 3.2 \text{ nm}$) corresponds roughly to the molecular length and signifies the characteristic correlation hole effect due to concentration fluctuations. The second, centered at $q = 11.1 \text{ nm}^{-1}$ ($d = 0.55 \text{ nm}$), corresponds to the mean intermolecular distance between organic-organic, organic-ODMS, and ODMS-ODMS moieties, indicating the molecular mixing of these components.

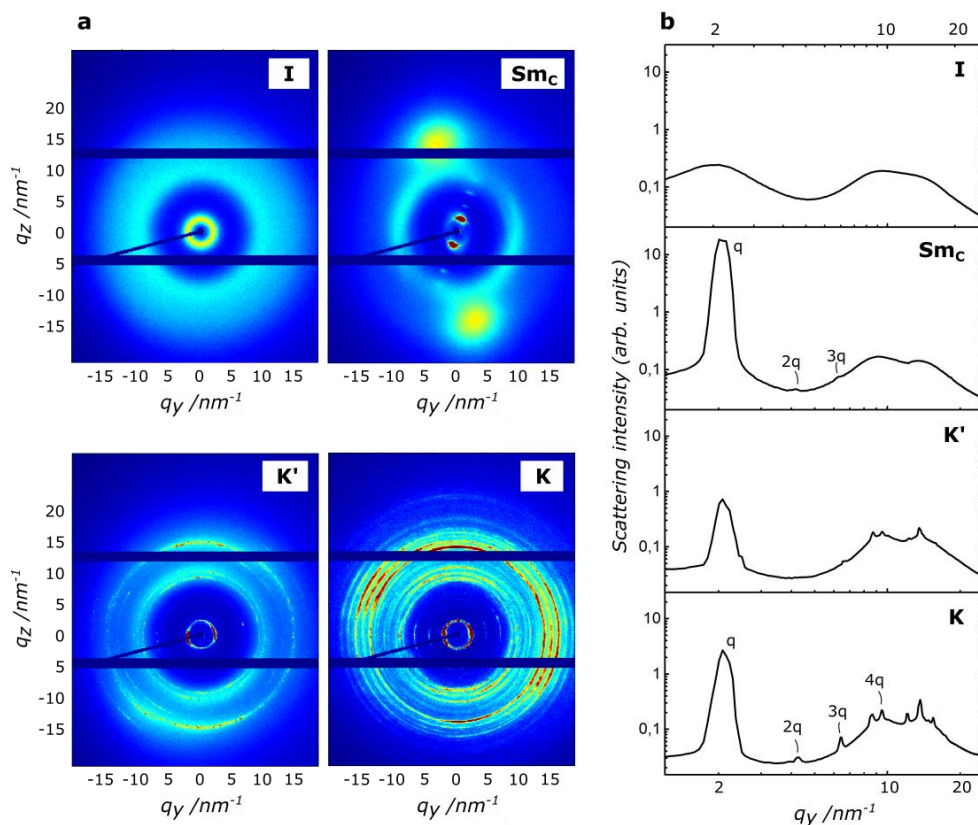


Figure 3. 2D XRD diffractograms (a) and the reduced 1D data (b) for LC-6Si obtained in the various LC phases: I (164 °C), SmC (135 °C), K' (13 °C), K (0 °C). Sample to detector distance: 91 mm.

Below the isotropic transition (135 °C), the peak at small angles sharpens and increases in relative intensity. The small-angle peak is centered at $q = 2.1 \text{ nm}^{-1}$, with additional higher order peaks present at $q = 4.2 \text{ nm}^{-1}$ and $q = 6.3 \text{ nm}^{-1}$ in the ratio q , $2q$, $3q$, signifying self-assembly into smectic layers with a periodicity of approximately 3.0 nm. Interestingly, the wide angle peak has split into two distinct peaks, centered at $q = 9.0 \text{ nm}^{-1}$ ($d = 0.70 \text{ nm}$) and $q = 14.0 \text{ nm}^{-1}$ ($d = 0.45 \text{ nm}$). These values are typical for ODMS-ODMS and organic-organic interactions, respectively signifying the segregation between bulky ODMS and organic moieties into separate layers.^[10] At lower temperatures (13 °C), additional peaks appear in the wide-angle region, demonstrating partial crystallization of the molecule. Since this transition is associated with a limited enthalpy change (Figure 2a), this phase is identified as lamellar pre-crystalline or soft-crystalline phase. Finally, at even lower

temperatures (0 °C), full crystallization occurs, as indicated by the appearance of many peaks in the wide-angle region.

The smectic layer spacing varies in discrete steps at temperatures corresponding to the phase transition temperatures (Figure 4a). Within the smectic LC window, the layer spacing slightly decreases with decreasing temperature from 3.03 nm (135 °C) to 2.99 nm (40 °C), likely due to a temperature dependence of the molecular tilt. To investigate this, the temperature-dependent tilt of the smectic layers and molecular components was investigated.

The director n , which is the spatial and temporal average of the long molecular axes, was defined as oriented perpendicular to the scattering intensity stemming from the organic-organic intermolecular interactions. The director tilt Ω , defined as the angle between the scattering intensity originating from the lamellar layers and the director n , was also extracted from the scattering data (Figure 4b). In this case we consider only the dominant layer orientation of the two layer orientations with opposite tilt normally found for tilted Smectics. The director tilt varies from 70° to 20° across the LC temperature range. This variation is extreme, considering the limited changes in layer spacing (Figure 4a). If we assume perfectly ordered rodlike molecules with director tilt Ω , the observed layer spacing d is equal to $d = l \cos(\Omega)$,^[15] in which l is the estimated molecular length $l = 4.5$ nm. According to this equation, the expected director tilt $45^\circ < \Omega < 50^\circ$. Hence, the molecules can be considered as disordered within the smectic layers. Together with the limited reduction in layer spacing across the temperature range, this suggests that the local molecular long axis (the local director) is tilted through a finite angle, while azimuthally uniformly distributed.^[8,15] This behavior has been previously observed for siloxane liquid crystals.^[8,15-17] Furthermore, the siloxane tilt α was extracted from the scattering data as the angle between the scattering intensity corresponding to the organic-organic intermolecular interactions (by definition perpendicular to n), and the scattering intensity corresponding to the ODMS-ODMS intermolecular interactions. Interestingly, when plotted together with the director tilt (Figure 4b), the values correspond almost exactly. This indicates that the ODMS-ODMS intermolecular interactions are on average perpendicular to the smectic layers regardless of the director tilt, which suggests that the microphase separation between organic and ODMS components drives a surface energy minimization that is responsible for the lamellar morphology.^[10]

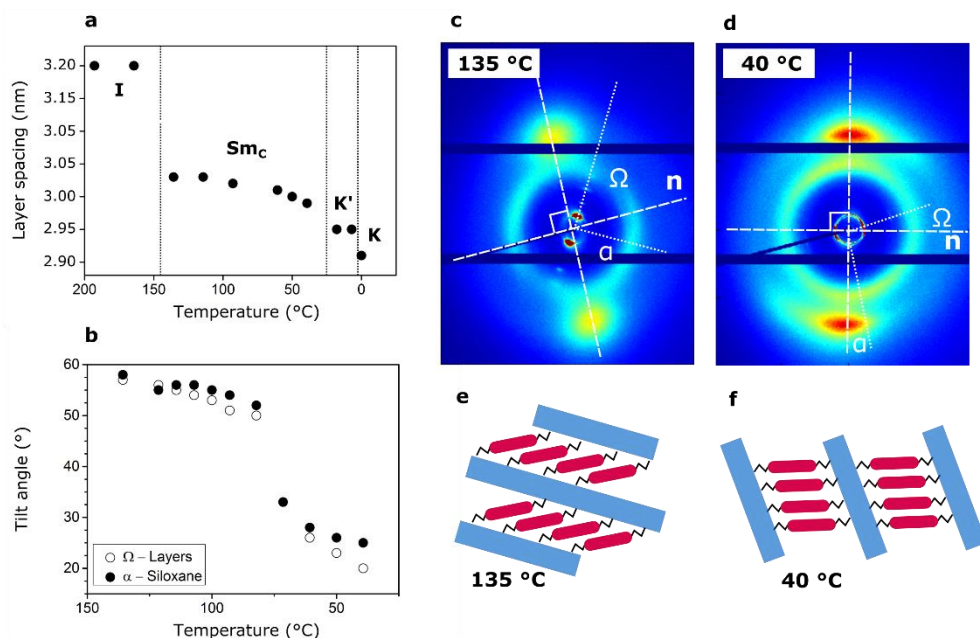


Figure 4. Observed smectic layer spacing (a) and calculated tilt angles (b) for LC-6Si in the Sm_C phase. The angle definitions are shown for the extreme temperature cases of 135 °C (c) and 40 °C (d). Corresponding proposed packing models of the dominant Smectic layer morphology at 135 °C (e) and 40 °C (f). Red: rigid core; black: alkyl chains, blue: ODMS layer.

For nanopatterning applications, the liquid crystals must self-assemble in thin films. To this end, a dilute solution of **LC-6Si** was spin-coated onto a PDMS-modified silicon wafer.^[14] The wafer was modified to ensure wetting of the LC. In order to study the film morphology, grazing-incidence x-ray diffraction (GIXRD) experiments were performed at room temperature (Figure 5). In the small angle region, significant diffraction intensity was obtained perpendicular to the substrate plane, in the ratio $q, 2q, 3q, 4q$, revealing a lamellar sheet morphology which is oriented parallel to the substrate. The primary scattering peak was centered at $q = 2.1 \text{ nm}^{-1}$, signifying the presence of smectic layers with a periodicity of 3.0 nm. The periodicity corresponds exactly with the data obtained in bulk. In the wide-angles of the diffraction pattern, a complex combination of highly oriented reflections was obtained, indicative of a (partially) crystalline morphology.

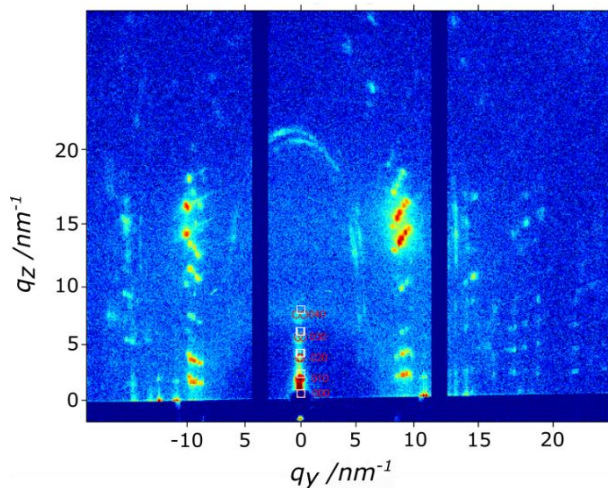


Figure 5. GIXRD diffractogram of a 40 nm **LC-6Si** thin film at room temperature.

3.3. Conclusion

In this chapter, we reported on the synthesis, characterization, and self-assembly behavior of novel oligo(dimethylsiloxane) liquid crystal **LC-6Si**. **LC-6Si** forms tilted smectic lamellar structures with 3.0 nm periodicity in bulk and in thin films. As observed by x-ray diffraction experiments, the director tilt is highly dependent on temperature (20° - 70°), while the layer spacing relatively temperature independent (2.99 - 3.03 nm). In order to employ the etch contrast provided by the ODMS, the LCs must first be oriented perpendicular to the film surface. This might be achieved with a neutral surface layer,^[18,19] a suitable top-coat,^[20] or photo-alignment.^[21] This type of material may be used to explore the resolution limits of directed self-assembly of lamellar sub-5 nm patterns.

3.4. Materials & Methods

Heptamethyltrisiloxane was purchased from Fluorochem and used as received. Dichloromethane (CH₂Cl₂) was dried over aluminum oxide in a commercial Grubbs-type system. The synthetic products were identified by 400 MHz NMR. Deuterated chloroform (CDCl₃) and tetramethylsilane (TMS) were used as solvent and internal standard, respectively. Molecular weights were determined by MALDI-TOF MS. Temperature stability was evaluated by thermal gravimetric analysis (TGA). Phase behavior was evaluated with differential scanning calorimetry (DSC), polarized optical microscopy (POM), and X-Ray diffraction (XRD). For POM analysis a small

amount of product was placed in between two glass microscope slides. XRD spectra were collected in a setup equipped with a Linkam hotstage for temperature control and a sample holder featuring 1 Tesla permanent magnets. Grazing-incidence X-ray diffraction (GIXRD) spectra were obtained at room temperature and around the critical angle (0.18°). For thin film preparation, a hydroxy-terminated PDMS homopolymer from Polymer Source with molecular weight 5 kg mol^{-1} was applied onto silicon substrates from a 1-2 wt. % solution in heptane, baked at 150°C for at least 24h, and rinsed with heptane. The liquid crystals were subsequently spin-coated from 1 wt. % solution in heptane (3000 RPM, 45s). The film thickness was approximately 40 nm as estimated by ellipsometry.

3.5. Synthetic procedures

A 20mL Schlenk flask was equipped with a magnetic stir bar and charged with 1,4-bis[4-(4-butenyloxy)benzoyl] azobenzene^[14] (170 mg, 0.30 mmol) and heptamethyltrisiloxane (243 mg, 1.05 mmol), and put under an Argon atmosphere. Subsequently dry DCM (10 mL) and drop of Karstedt's catalyst (1% in xylene) were added. The solution was stirred overnight at room temperature. The reaction was quenched in methanol and the reaction product was purified using column chromatography (hexane/ethyl acetate 20/1) to yield LC-6Si as an orange paste (yield 26%). ¹H NMR (400 MHz, CDCl₃, δ in ppm): 8.16 (d, 4H); 8.00 (d, 4H); 7.39 (d, 4H); 7.00 (d, 4H); 4.06 (m, 4H); 1.86 (m, 4H); 0.63 (m, 4H); 0.13-0.01 (m, 42H). ¹³C NMR (400 MHz, CDCl₃, δ in ppm): 164.6, 163.7, 153.1, 150.1, 132.3, 124.1, 122.4, 121.2, 114.4, 68.0, 32.6, 29.7, 19.7, 18.0, 1.82, 1.28. MALDI-TOF MS: [M+Na]⁺ calcd for C₄₈H₇₄N₂O₁₀Si₆ 1029.39, found 1029.49.

3.6. References

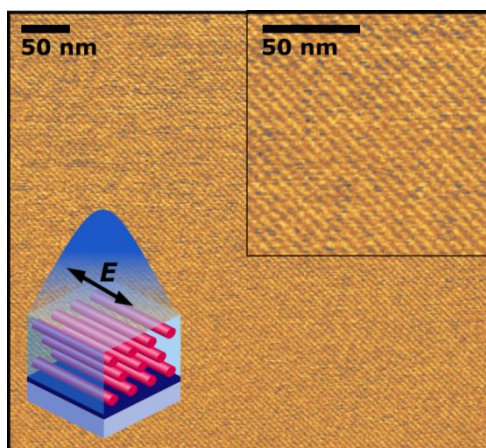
- [1] S.-J. Jeong, J. Y. Kim, B. H. Kim, H.-S. Moon, S. O. Kim, *Mater. Today* **2013**, *16*, 468.
- [2] M. Luo, T. H. Epps, *Macromolecules* **2013**, *46*, 7567.
- [3] R. Ruiz, H. M. Kang, F. A. Detcheverry, E. Dobisz, D. S. Kercher, T. R. Albrecht, J. J. de Pablo, P. F. Nealey, *Science* **2008**, *321*, 936.
- [4] C. Sinturel, F. S. Bates, M. A. Hillmyer, *ACS Macro Lett.* **2015**, *4*, 1044.
- [5] C. Tschierske, *Angew. Chem.-Int. Ed.* **2013**, *52*, 8828.
- [6] E. Nishikawa, E. T. Samulski, *Liq. Cryst.* **2000**, *27*, 1463.
- [7] J. Newton, H. Coles, P. Hodge, J. Hannington, *J. Mater. Chem.* **1994**, *4*, 869.
- [8] S. H. Ryu, T. J. Shin, T. Gong, Y. Shen, E. Korblova, R. Shao, D. M. Walba, N. A. Clark, D. K. Yoon, *Phys. Rev. E* **2014**, 89
- [9] R. Achten, A. Koudijs, M. Giesbers, A. Marcelis, E. Sudholter, *Mol. Cryst. Liq. Cryst.* **2007**, *477*, 169.

- [10] C. Pugh, J. Y. Bae, J. Dharia, J. J. Ge, S. Z. D. Cheng, *Macromolecules* **1998**, *31*, 5188.
- [11] N. Olsson, B. Helgee, G. Andersson, L. Komitov, *Liq. Cryst.* **2005**, *32*, 1139.
- [12] L. Li, C. D. Jones, J. Magolan, R. P. Lemieux, *J. Mater. Chem.* **2007**, *17*, 2313.
- [13] E. Corsellis, D. Guillon, P. Kloess, H. Coles, *Liq. Cryst.* **1997**, *23*, 235.
- [14] K. Nickmans, J. N. Murphy, B. de Waal, P. Leclère, J. Doise, R. Gronheid, D. J. Broer, A. P. H. J. Schenning, *Adv. Mater.* **2016**, *28*, 10068.
- [15] U. Manna, R. M. Richardson, A. Fukuda, J. K. Vij, *Phys. Rev. E* **2010**, *81*, 50701.
- [16] G. Galli, M. Reihmann, A. Crudeli, E. Chiellini, Y. Panarin, J. Vij, C. Blanc, V. Lorman, N. Olsson, *Mol. Cryst. Liq. Cryst.* **2005**, *439*, 245
- [17] Q. Song, D. Nonnenmacher, F. Giesselmann, R. P. Lemieux, *J. Mater. Chem. C* **2012**, *1*, 343.
- [18] E. Huang, T. P. Russell, C. Harrison, P. M. Chaikin, R. A. Register, C. J. Hawker, J. Mays, *Macromolecules* **1998**, *31*, 7641.
- [19] S. Ji, C. C. Liu, J. G. Son, K. Gotrik, G. S. W. Craig, P. Gopalan, F. J. Himpfel, K. Char, P. F. Nealey, *Macromolecules* **2008**, *41*, 9098.
- [20] C. M. Bates, T. Seshimo, M. J. Maher, W. J. Durand, J. D. Cushen, L. M. Dean, G. Blachut, C. J. Ellison, C. G. Willson, *Science* **2012**, *338*, 775.
- [21] T. Seki, *Polym. J.* **2014**, *46*, 751.

Chapter 4

Three-dimensional orientational control in self-assembled thin films with sub-5 nm features by light

Abstract. While self-assembled molecular building blocks could lead to many next-generation functional organic nanomaterials, control over the thin film morphologies to yield monolithic sub-5 nm patterns with three-dimensional orientational control at macroscopic length scales remains a grand challenge. We studied a series of photoresponsive hybrid oligo(dimethylsiloxane) liquid crystals that form periodic cylindrical nanostructures with periodicities between 3.8 – 5.1 nm (see chapter 2). The liquid crystals can be aligned in-plane by exposure to actinic linearly polarized light and out-of-plane by exposure to actinic unpolarized light. These results allow the generation of highly-ordered sub-5 nm patterns in thin films at macroscopic length scales, with control over the orientation in a non-contact fashion.



This chapter is based on:

K. Nickmans, G. M. B. Bogels, C. Sánchez-Somolinos, J. N. Murphy, P. Leclère, I. Voets, A. P. H. J. Schenning, *Small* **2017**, 13, 170143.

4.1. Introduction

Decades of soft matter research have yielded a plethora of building blocks, such as block copolymers,^[1-4] colloids,^[5] surfactants,^[6] and molecules,^[7-9] which can self-assemble into a range of periodic nanostructures, such as lamellae, cylinders or more complex geometries (chapter 1). Yet, the generation of defect-free thin film nanostructure arrays remains a grand challenge due to the tendency of these building blocks to self-assemble into arbitrarily oriented poly-domain structures.^[7] Achieving a thin film monolithic alignment of these materials, across the molecule to device length scales,^[10,11] could help to realize compelling advanced applications in areas such porous membranes,^[12-14] organic electronics,^[15] and nanolithography.^[16-18]

While traditional block copolymers (BCPs) have been the main driving force behind self-assembled thin film applications,^[1-4] sub-5 nm periodicities are more readily formed by small molecules.^[19,20] In bulk, these self-assembled small molecules have been aligned by for example shear,^[21,22] alignment layers,^[23,24] photo-alignment,^[25-30] magnetic fields,^[14,31] and geometric confinement.^[32-34] The induction of long range order and orientational control in thin films is, however, a critical step towards the application of these small molecule nanomaterials as supramolecular templates.^[7] In the sub- μm regime, photo-alignment is a potentially well-suited method as it is non-contact, free of complex surface modification, and compatible with top-down microfabrication techniques.

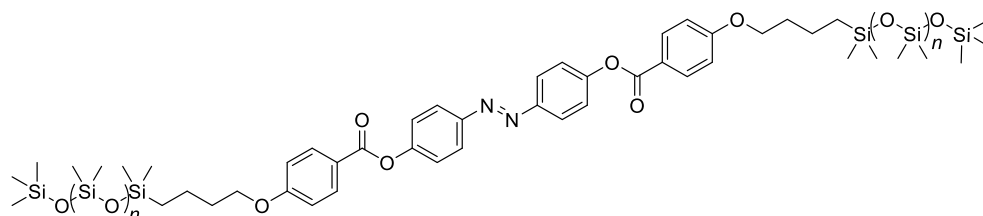
The groups of Seki and Ikeda revealed that thin film block copolymer (BCP) morphologies consisting of amorphous phase segregated cylinders in an Azobenzene (Az) liquid crystal (LC) matrix can be aligned with linearly polarized light (LPL).^[35-41] The rod-like *trans* Azs are isomerized most effectively when their transition moments are oriented parallel to the electric vector (E) of light. In the case of normally incident LPL, this leads to a statistical build-up of Azs moieties oriented orthogonal to E ,^[27,42-45] and the concurrent in-plane alignment of BCP nanostructures.^[35-39] It was shown that the in-plane alignment of cylinders proceeds through subdomain rotation in a cooperative and synchronized manner.^[46] In the case of normally incident unpolarized light, the Azs orient parallel to the light propagation direction minimizing their light absorption,^[47] which allows the on-demand switching between in-plane and out-of-plane directions.

In chapter 2, we reported a series of monodisperse organic-inorganic Az-LCs containing oligo(dimethylsiloxane) (ODMS) for etch contrast that form sub-5 nm

patterns,^[48] and showed that their self-assembly can be directed in-plane by graphoepitaxy, in a manner analogous to BCPs. In this chapter we demonstrate by a variety of techniques that the LC self-assembly can be directed both in-plane and out-of-plane with light, and that the mobility of the LC phase is key to achieving a rapid alignment. While it should be noted that photo-alignment is a well-established method to align liquid crystals, both in terms of photo-alignment layers ^[26] and the alignment of bulk material,^[25,27,49] the 3 dimensional orientational control by light of LC morphologies and pattern generation with sub-5 nm periodicities in thin films has not been reported.

4.2. Results & Discussion

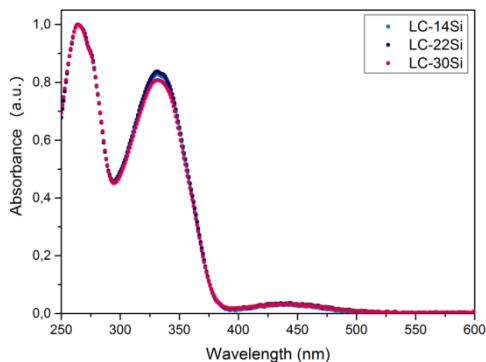
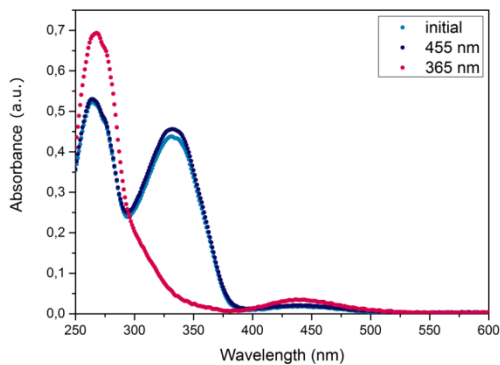
The molecular structure of the employed ODMS liquid crystals,^[48] is depicted in Scheme 1. The LCs consist of a photoresponsive *trans* azobenzene containing rigid core flanked by flexible ODMS coils. Due to the bulkiness of the ODMS coils, the molecules form columnar liquid crystalline phases in which the LC cylinder is considered to consist of a stacked arrangement of rigid rods, while the matrix consists of ODMS (chapter 2). The phase behavior and associated lattice parameters are dependent on the length of the ODMS coil and temperature (Table 1). Dilute solutions of the Az-liquid crystals with variant ODMS lengths displayed indistinguishable UV-vis absorption spectra (Figure 1) with the characteristic π - π^* transition absorption band of the *trans* isomers with a peak at 330 nm and a weaker n - π^* transition absorption band with a maximum at 439 nm. The LCs isomerized from *trans* to *cis* upon irradiation with 365 nm UV light, resulting in a decreased absorbance at 330 nm, and an increase of the weaker n - π^* band at 439 nm indicating the formation of the *cis* isomer (Figure 2). Subsequent irradiation with 455 nm light, at the low energy side of the n - π^* band, recovered the absorption spectra to the initial state consisting of predominantly *trans* isomers.



Scheme 1. Molecular structure of the ODMS liquid crystals, where n represents the length of the ODMS tail: **LC-14Si** ($n = 5$), **LC-22Si** ($n = 9$), **LC-30Si** ($n = 13$).

Table 1. Phase behavior and lattice parameters of the ODMS liquid crystals (see chapter 2).^[48]

	n	Phase behavior [$^{\circ}$ C] (Lattice parameters [nm])
LC-14Si	5	Col _{Rec} 109 (3.8, 7.4) Iso
LC-22Si	9	Col _{Rec} 49 (4.3, 8.5) Col _{Hex} 102 (4.5) Iso
LC-30Si	13	Col _{Hex} 95 (5.1) Iso

**Figure 1.** Normalized UV-vis absorption spectra of LC-14Si, LC-22Si, and LC-30Si in chloroform.**Figure 2.** UV-vis absorption spectra of LC-22Si in chloroform prior to irradiation, after irradiation with 365 nm light, and after subsequent irradiation with 455 nm light.

The photoresponsive properties of the Az liquid crystals were first studied in thin untreated quartz cells (thickness = $\sim 1.5 \mu\text{m}$). Figure 3a shows a schematic representation of the cylinder morphology, a polarized optical microscopy (POM) image, and polarized UV-vis spectroscopy data of **LC-22Si** in the cell. The observed birefringent texture under POM indicates that the optical axes of the domains (and also the columnar axes) are oriented randomly. Compared to its corresponding absorption in solution (Figure 2), the $\pi\text{-}\pi^*$ transition absorption peak exhibited some broadening, indicative of aggregated Az moieties in the LC state. However, no shift was observed, suggesting restricted Az aggregation in the LC state,^[29] potentially as an effect of the bulky ODMS matrix. Polarized UV-vis absorption spectroscopy of the absorption at 330 nm further shows equal absorbance of Az *trans* isomers across all polarization angles, signifying the random orientation of the Az in the plane of the cell.

In order to see if the cylindrical domains could be oriented through photoinduced *trans-cis-trans* isomerization cycles, the cell containing **LC-22Si** was subjected to 455 nm LPL (Figure 3b), while cooling ($0.1 \text{ }^\circ\text{C min}^{-1}$) from the isotropic state to room temperature and then, in a subsequent experiment, to unpolarized 455 nm light (Figure 3c), under the same thermal cooling conditions. In the case of LPL, the POM texture after irradiation was highly anisotropic, extinguishing light when E was oriented at 0° and 90° relative to crossed polarizers. At 45° to the polarizers, the sample exhibited a bright state, indicative of the preferential orientation of the mesogens in a planar fashion. The corresponding polarized absorption measurements were used to calculate a dichroic ratio (DR) as $DR = (A_{\perp} - A_{\parallel}) / (A_{\perp} + A_{\parallel})$, where A_{\perp} and A_{\parallel} represent the absorbance at the peak of the $\pi\text{-}\pi^*$ transition band (330 nm), measured with polarized light perpendicular and parallel to E . For randomly oriented Azs, $DR = 0$, while for perfectly oriented Azs perpendicular to E , $DR = 1$. In this case, $DR = 0.51$, indicating that the Az moieties are on average oriented perpendicular to E ,^[49] though the moderate value suggests that there is disorder around the preferential orientation direction. XRD experiments (Figure 4) reveal that the Az reorientation results in the alignment of the LC nanocylinders in a planar fashion ($a = 4.5 \text{ nm}$) with the cylindrical axis parallel to E .

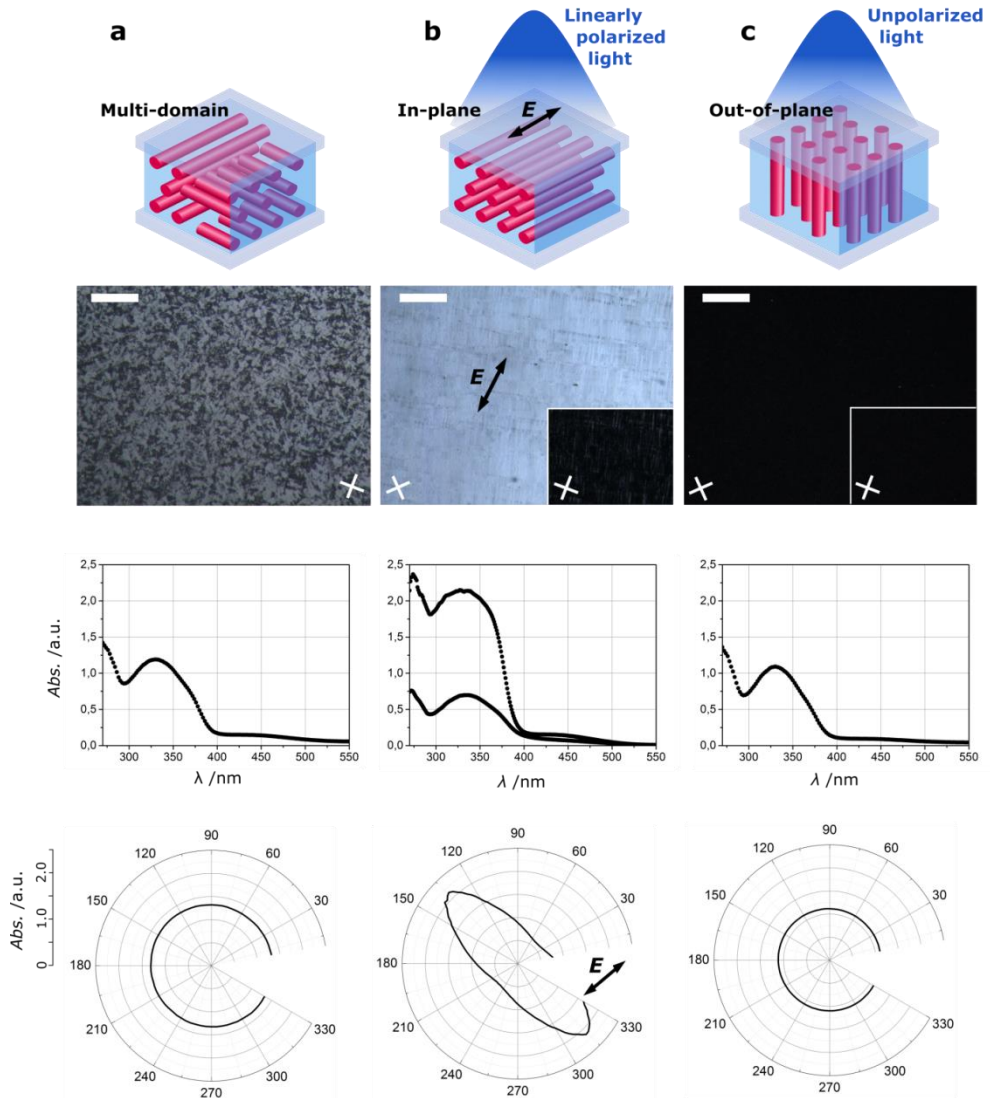


Figure 3. Schematic representations, room temperature POM images, room temperature polarized UV-vis absorption spectra, and corresponding polar plots, of LC-22Si contained in a quartz cell ($\sim 1.5 \mu\text{m}$) prior to photo-alignment (a), after exposure to linearly polarized light (b), and after exposure to unpolarized light (c). The E direction is indicated by the arrow. The crosses represent the transmission axes of the crossed polarizers. All scale bars: $100 \mu\text{m}$.

Next, the out-of-plane alignment was investigated (Figure 3c) by irradiating with unpolarized 455 nm light. In this case, the POM texture no longer exhibited birefringence (optically isotropic), and no in-plane dichroism was induced ($DR = 0$). XRD experiments (Figure 4b) reveal a hexagonal symmetry in the scattering, originating from the vertical orientation of LC nanocylinders ($a = 4.5 \text{ nm}$) in an

essentially mono-domain fashion. The out-of-plane cylinder orientation is characterized by a small decrease in the π - π^* transition absorption peak intensity when compared to the unaligned state and a large increase in absorption when the sample is tilted (Figure 5) which suggest the Azs have partially turned parallel to the propagation direction of light in accordance to literature.^[43,47,54] However, the significant remaining absorption intensity in the plane suggest that the effective photoinduced alignment of the azobenzene moieties perpendicular to the light polarization is compensated by a tendency of the Azs to align perpendicular to the axis of the cylinder. Interestingly, this suggests that only limited differences in the photoinduced Az orientation are responsible for the highly aligned LC mesophase morphologies in 3 dimensions, both in plane (moderate DR), and out-of-plane (limited deviation from horizontal). Overall these results show that light can be used to align the cylindrical mesophase morphology horizontally and vertically in a cell in a non-contact fashion. Furthermore, the photoinduced orientation, both at the chromophore and morphology level, are stable at room temperature and may be erased and reoriented.

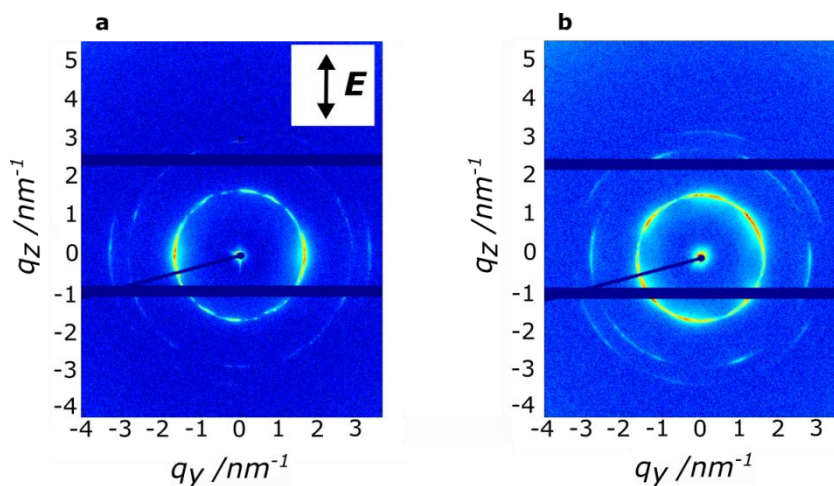


Figure 4. 2D medium-angle XRD of photo-aligned LC-22Si at 85 °C in a 1 mm capillary. The propagation direction of light during the alignment step is perpendicular to the detector plane. In the case of LPL (a), there is strong scattering perpendicular to E (indicated by the black arrow), indicating that the LC cylindrical axis is in the detector plane and parallel to E . In the case of unpolarized light (b), there is scattering with hexagonal symmetry, indicating the LC cylindrical axis is oriented out-of-plane in an essentially mono-domain fashion. The sample to detector distance is 441 mm.

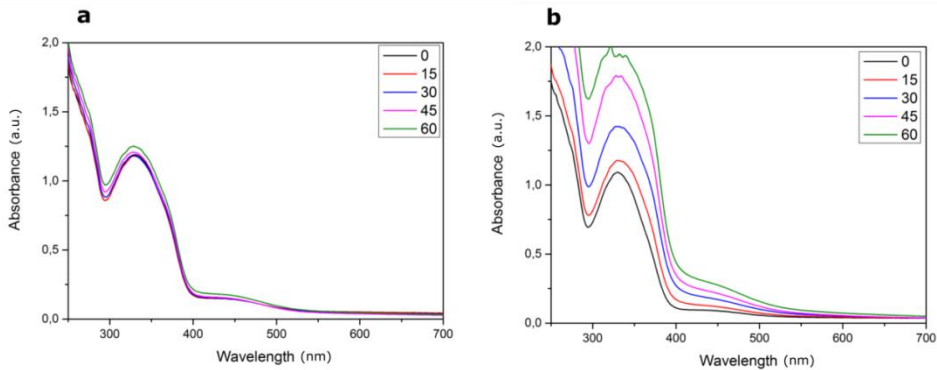


Figure 5. Tilted UV-vis spectra at room temperature of a LC-22Si cell before (a), and after (b) exposure to unpolarized 455 nm light. The numbers in the legend represent the tilt angle.

For most nanotechnology applications, the LC morphologies must be directed in sub- μm thin films. Therefore, LC thin films were prepared by spin-coating dilute solutions of liquid crystals in heptane onto PDMS-modified quartz substrates.^[48,55] A 10 mg/mL solution of LC-22Si resulted in films of 40 nm thickness, as determined by ellipsometry. The film surface consists of multi-layers of nanocylinders with a period of 4.3 nm,^[48] corresponding to the room temperature Col_{Rec} phase (Table 1). Without an external driving force for alignment, the cylinders are planar oriented over arbitrary azimuthal angles in a multi-domain fashion.

For the thin film photo-alignment experiments the films were heated up close to the clearing temperature. Figures 6a-d show 2D grazing-incidence X-ray diffraction (GIXRD) patterns of the LC-22Si thin film at 85 °C (Col_{Hex} phase, Table 1), before and after exposure to unpolarized light and LPL of 455 nm (1h., 0.6 J cm⁻² min⁻¹). Before photo-alignment (Figure 6a), periodic (q , $\sqrt{3}q$, $2q$) scattering peaks were observed at $q = 1.68 \text{ nm}^{-1}$, 2.90 nm^{-1} , and 3.36 nm^{-1} , corresponding to the Col_{Hex} phase ($a = 4.5 \text{ nm}$). The primary scattering peaks corresponding to the {1 0} planes were observed at azimuthal angles $\varphi \sim 30^\circ$, $\varphi \sim 90^\circ$, and $\varphi \sim 150^\circ$, confirming the self-assembly is exclusively in-plane.

After exposure to unpolarized light (Figure 6b), the periodicity remained at 4.5 nm, while the primary scattering peak appeared at azimuthal angles $\varphi \sim 0^\circ$, $\varphi \sim 180^\circ$. The in-plane scattering greatly diminished. This data suggests that the effect of unpolarized light is the re-orientation from in-plane cylinders to predominantly out-of-plane cylinders. However, it should be noted that the out-of-plane morphology could not be retained in thin films upon cooling to room temperature (*vide infra*).

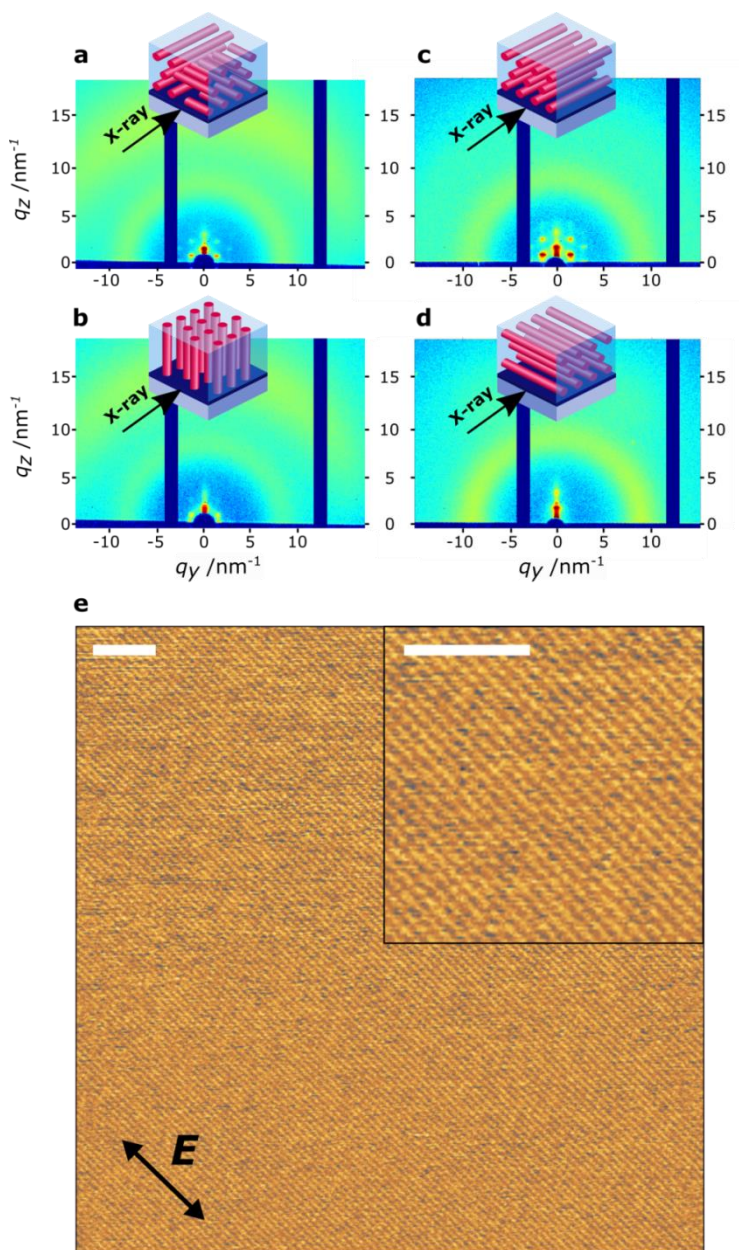


Figure 6. Thin film photo-alignment of LC-22Si: 2D GIWAXS profiles before photo-alignment (a), after photo-alignment with unpolarized light (b), and after photo-alignment with LPL (c-d) measured parallel (c) and perpendicular (d) to E ; High-resolution phase-mode AFM image of a planar aligned sample (e). The polarization direction of the LPL is indicated by the arrow. The inset corresponds to a 2x magnification. Scale bars: 50 nm.

In contrast, Figure 6c-d depicts GIXRD measurements recorded parallel (Figure 6c) and perpendicular (Figure 6d) to the E direction of LPL. Parallel to E , the diffraction pattern exhibits many higher order reflections corresponding to a hexagonal columnar lattice with high positional order. The periodicity remained at 4.5 nm. Perpendicular to E , the diffraction exhibits the total absence of reflections at $\varphi \sim 30^\circ$ and $\varphi \sim 150^\circ$. Scattering intensity is preserved only at the azimuthal angle of $\varphi \sim 90^\circ$. Together, this is consistent with the presence of vertically stacked layers of nanocylinders in which the cylinder axes are exclusively parallel to the E .

The aligned sample was subsequently cooled to room temperature (Col_{Rec} phase), and high-resolution atomic force microscopy (AFM) was performed in tapping mode. Figure 6e shows an AFM phase image, which exhibits a mono-axial array of periodic line structures with a periodicity of 4.3 nm. The LC cylinders are oriented parallel to the E direction, in accordance with the GIXRD data at 85 °C, indicating that the aligned planar morphology can be retained upon cooling to room temperature. Remarkably, there are no observable non-equilibrium defects that are usually found in photo-aligned glassy BCP systems,^[35,37,56] despite the value of DR to achieve this ($DR = 0.71$) differs from that of a perfectly ordered Az system ($DR = 1$).^[39]

Polarized UV-vis measurements (Figure 7) confirm that the corresponding alignment of Az moieties is perpendicular to the E direction ($DR = 0.71$), consistent with the results found in bulk (Figure 3b). These findings suggest that the Az moieties are on average perpendicular to the columnar axis and the effect of LPL is the net orientation of LC cylinders parallel to E . Furthermore, optical microscopy (Figure 8) reveals that the photoaligned thin films consist of large anisotropic domains which extend hundreds of micrometers in the direction parallel to E . Together, these results show that the alignment of LC cylinders can be achieved across large areas in sub-5 nm patterned thin films, and their 3 dimensional orientation can be controlled. However, in contrast to the behavior in a cell (Figure 3c), the out-of-plane morphology could not be retained in thin films, indicating the prominence of surface energy contributions to the free energy.^[56]

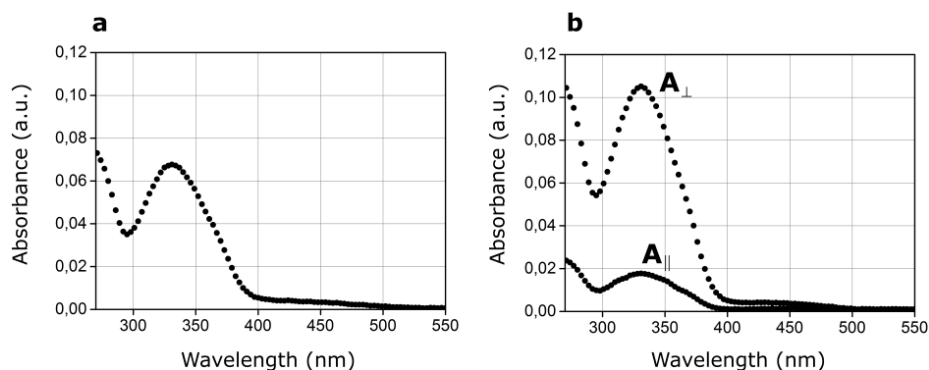


Figure 7. Room temperature polarized UV-vis absorption spectra of a **LC-22Si** thin film (thickness 40 nm) prior to (a) and after (b) exposure to polarized 455 nm light. The absorption parallel and perpendicular to E are indicated.

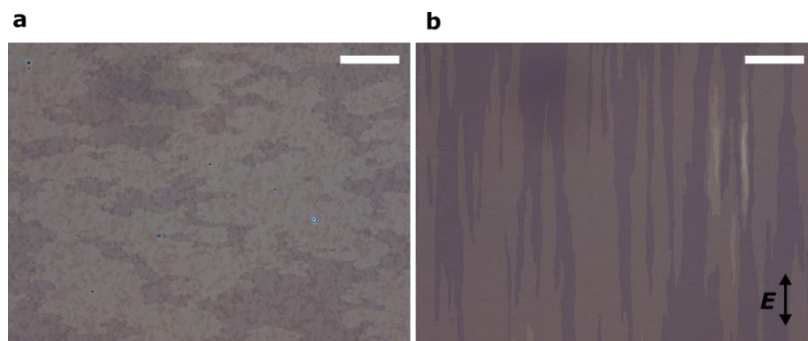


Figure 8. Optical microscopy of an **LC-22Si** thin film (thickness 40 nm) prior to (a) and after (b) exposure to polarized 455 nm light. The E is indicated by the arrow. Scale bars: 100 μm .

In order to gain insight into the three-dimensional photo-alignment process, thicker films were prepared (~ 150 nm), allowing combined time-resolved polarized UV-vis absorption spectroscopy and GIXRD measurements to correlate the orientation of photoresponsive azobenzene moieties with the alignment of the cylinders in time. First the in plane orientation at regular intervals (1 min, $0.6 \text{ J cm}^{-2} \text{ min}^{-1}$), during an initial alignment (5 min) and a subsequent orthogonal realignment process (10 min) was studied. In each case, the photo-alignment was performed at 85°C . For UV-vis absorption spectroscopy, the samples were quickly cooled to room temperature and at each interval, DR was calculated. In this case, the direction of E in the second exposure was chosen as the reference direction.^[37] For randomly oriented Azs, $DR = 0$, while for perfectly oriented Azs along the first and second alignment direction DR becomes -1 and $+1$ respectively.

Figure 9 shows the angular dependence of azobenzene absorbance at selected times during the alignment procedure. No optical anisotropy was observed prior to exposure to LPL (Figure 9a, $DR = 0$). After a 5 minute LPL exposure (3.0 J cm^{-2}), the azobenzene absorbance became highly anisotropic; with increased absorbance perpendicular to E and decreased absorbance in the parallel direction (Figure 9b, $DR = -0.56$). The sample was subsequently subjected to a second LPL irradiation in the orthogonal direction. After a 1 minute LPL exposure (0.6 J cm^{-2}), the polar plot regained its circular shape representing the almost complete loss of optical anisotropy (Figure 9c) ($DR = -0.12$). After a 5 minute LPL exposure (3.0 J cm^{-2}), the optical anisotropy was almost completely regained in the direction orthogonal to the initial direction (Figure 9d, $DR = 0.53$). The change in sign is representative for the change in orientation of the Az mesogens upon exposure in the orthogonal direction, and demonstrates the feasibility of the alignment process in arbitrary directions.

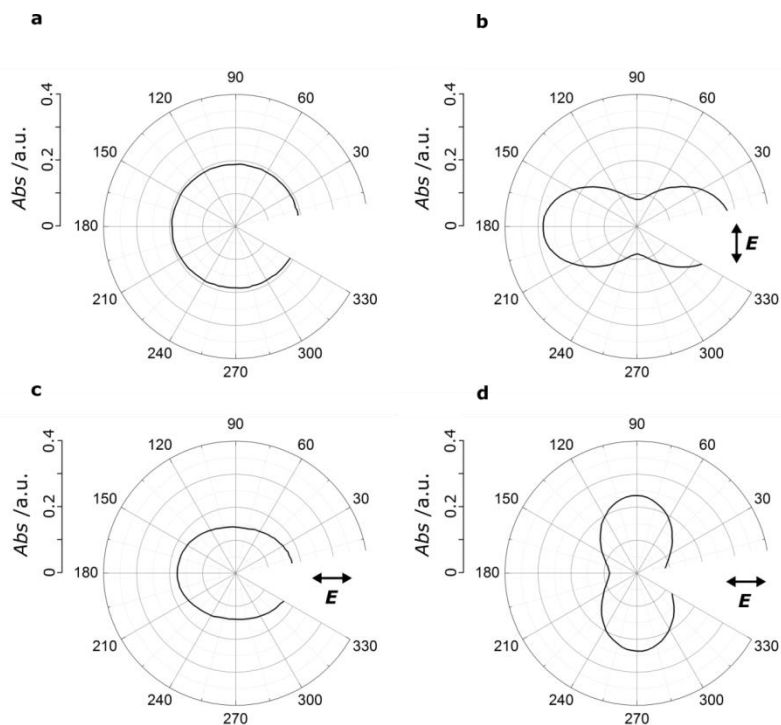


Figure 9. Room-temperature polarized UV-vis spectroscopic data for an **LC-22Si** thin film aligned using linearly polarized light at $85 \text{ }^\circ\text{C}$ ($0.6 \text{ J cm}^{-2} \text{ min}^{-1}$). Polar plots are shown for the film before irradiation (a), after the first 5 min LPL irradiation (b), after a short 1 min perpendicular LPL irradiation (c), and after a 5 min perpendicular LPL irradiation (d). The electric field vector of the LPL is indicated by the arrow.

GIXRD was used to examine the time-course evolution of the orientation of LC cylinders during the alignment and subsequent re-alignment process. Similar to the UV-vis experiments (Figure 9), the sample was irradiated at 85 °C, and data was collected over 1 min intervals ($0.6 \text{ J min}^{-1} \text{ cm}^{-2}$). The measurements were performed using two orthogonal X-ray incident directions (beam 1, beam 2), which were parallel to the E of the LPL in the first and second exposure, respectively.

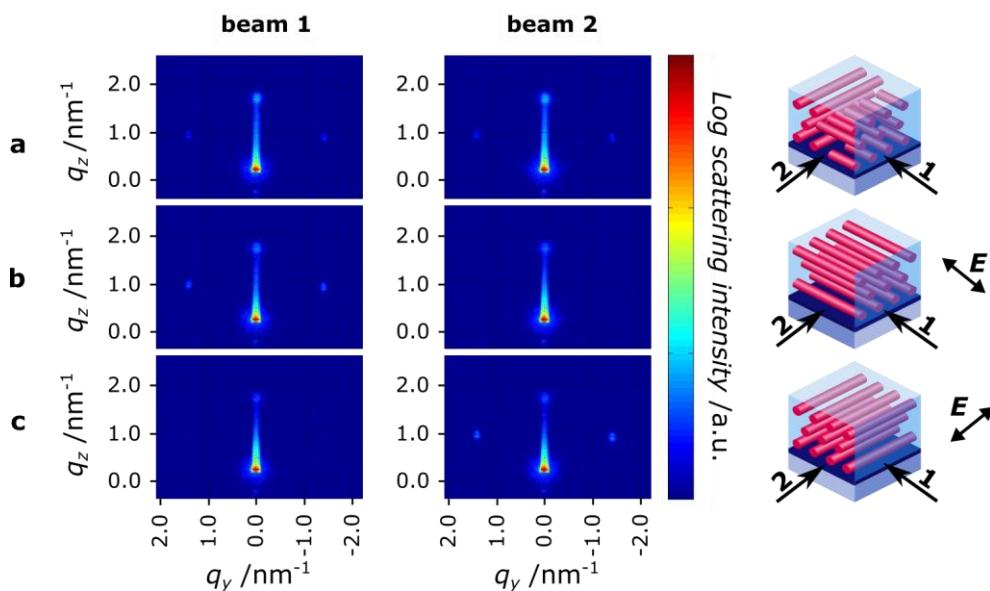


Figure 10. Snapshots of the 2D GIXRD profiles for the **LC-22Si** thin film aligned using LPL at $0.6 \text{ J min}^{-1} \text{ cm}^{-2}$, collected before irradiation (a), after the first 5 min. LPL irradiation (3.0 J cm^{-2}) (b), and after a second 5 min. perpendicular LPL irradiation (3.0 J cm^{-2}) (c), obtained using two orthogonal X-ray incident directions (beam 1, beam 2). The E is indicated by the arrow.

Figure 10 presents representative snapshots of the 2D scattering images collected before irradiation (a), after the first 5 min. LPL irradiation (3.0 J cm^{-2}) (b), and after a second 5 min. perpendicular LPL irradiation (3.0 J cm^{-2}) (c). Before irradiation, the scattering intensity was independent of the incident direction of the X-rays, signifying the initial multi-domain state of the film (Figure 8a). During the course of the first LPL irradiation, beam 1 resulted in increased scattering at azimuthal angle $\varphi \sim 30^\circ$ and $\varphi \sim 150^\circ$, while beam 2 resulted in a fast loss of scattering (Figure 10b). These features are indicative of the photoinduced mono-axial alignment of hexagonally well-packed LC cylinders parallel to E . Subsequent irradiation in the orthogonal direction resulted in the inverse situation (Figure 10c).

Scattering at azimuthal angle $\varphi \sim 90^\circ$ is maintained in all cases, consistent with the preservation layers of nanocylinders stacked in the plane.

To further examine the correlation between the polarized UV-vis spectroscopic data related to the azobenzene orientation (Figure 9), and the GIXRD measurements related to the LC nanocylinder orientation (Figure 10), over the course of the initial alignment (5 min) and subsequent orthogonal realignment (20 min) process, the data are plotted together in Figure 11. For simplicity we now refer to the second realignment process (beyond the dotted line in Figure 11). The *DR*, shown in Figure 11a, climbs exponentially from a negative to a positive value. The signal is almost saturated after 5 min. No lag period was resolved, indicating that the photo-stationary state is reached rapidly under these conditions (455 nm irradiation, $0.6 \text{ J min}^{-1} \text{ cm}^{-2}$).

The average GIXRD scattering intensities at azimuthal angle $\varphi \sim 30^\circ$ and $\varphi \sim 150^\circ$, which were obtained perpendicular (closed circles) (beam 1) and parallel (open circles) (beam 2) to the incidence of the LPL in the second alignment step, are plotted in Figure 11b. In the perpendicular direction (beam 1), the signal decays immediately after irradiation, and is lost rapidly (approx. 5 min.). The loss in scattering intensity rapidly follows the change in *DR*. In the parallel direction (beam 2), a short lag period is observed, and the signal continues to increase over a longer period (approx. 20 min.). This observation is different from previously reported observations for BCPs,^[37] in which the GIXRD intensity rises only after the *DR* has saturated. This finding suggests that the LCs are mostly re-oriented within the first few minutes (approx. 5 min.), and that the subsequent rise in GIXRD intensity likely corresponds to the fusion of separate re-oriented subdomains to form a monodomain. The faster dynamics in our system may be the result of the high mobility and low viscosity of the low molecular weight liquid crystalline phase.

In order to more directly compare *DR* with the GIXRD intensities, an order parameter of the cylinders was calculated as $S = (I_1 - I_2) / (I_1 + I_2)$, with I_1 and I_2 the average of the scattering intensities at azimuthal angles $\varphi \sim 30^\circ$ and $\varphi \sim 150^\circ$, recorded with beam 1 and beam 2, respectively. Similar to *DR*, for randomly aligned cylinders $S = 0$, while for perfectly aligned cylinders along directions 1 and 2 the order parameter becomes -1 and +1 respectively. Figure 11c shows that the trend of S is closely coupled to that of the *DR*. Hence, the change in order of the cylinders is coupled to the change in Az orientation. It is indeed expected that the nanocylinder order is more closely linked to the Az order (*DR*) than in the previously studied BCP system for this purpose,^[37] since the Azs are directly contained within the cylinder

nanostructures, as opposed to forming part of the surrounding matrix material.^[35-41] In contrast to the *DR*, *S* reaches the theoretical minimum (-1) and maximum (1) values, representative for a perfectly ordered system. In other words, despite the fact that the *Az* moieties show a local disorder around the preferential orientation direction (moderate *DR*), the degree of alignment of the self-assembled cylinders is very high (maximum *S*).

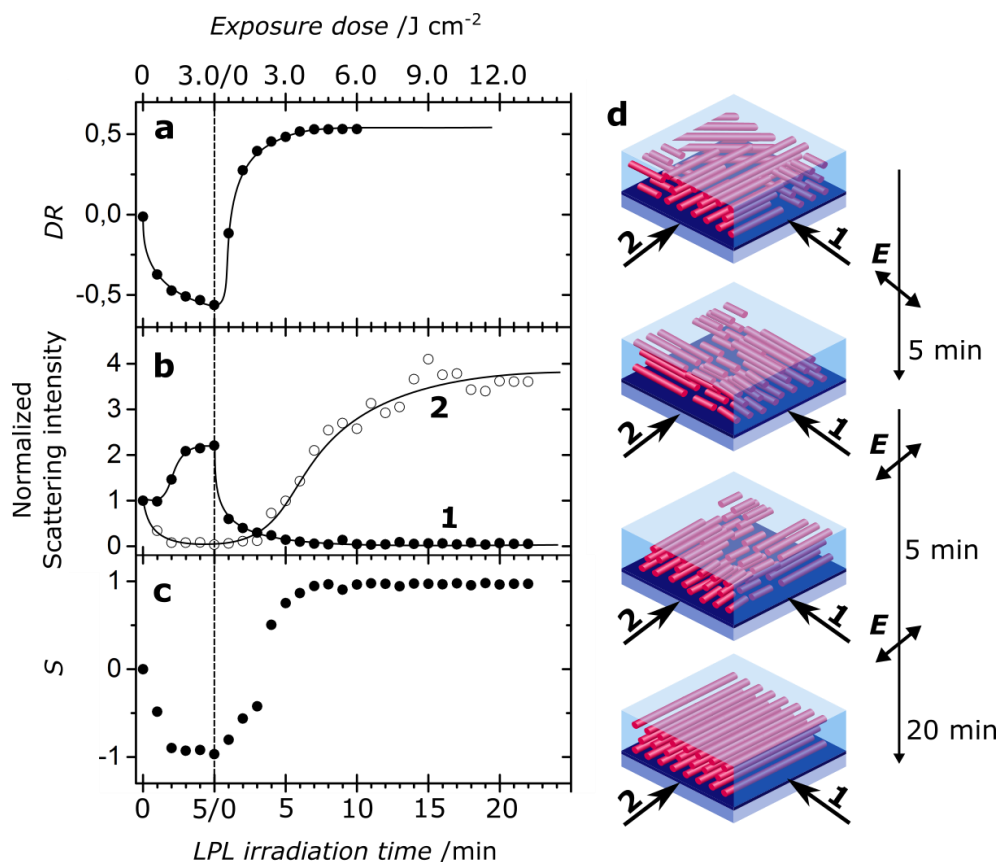


Figure 11. Time-course profiles of the dichroic ratio *DR* (a), average GIXRD scattering intensities at azimuthal angles $\varphi \sim 30^\circ$ and $\varphi \sim 150^\circ$ measured perpendicular (closed circles) (beam 1) and parallel (open circles) (beam 2) to the incidence of the LPL in the second exposure (b), order parameter *S* of the cylinders (c), and schematic representations of the nanocylinder orientation (d) at various times in the alignment procedure as a function of the irradiation time and exposure dose, for the **LC-22Si** thin film aligned using LPL at $0.6 \text{ J min}^{-1} \text{ cm}^{-2}$. The *E* and beam directions are indicated by the arrows.

It is expected that the temperature has a significant effect on the self-assembly processes during the photo-alignment procedure. In order to further elucidate this, the effects of temperature and the clearing temperature were investigated. Figure 12 shows the time-evolution of DR for **LC-14Si**, **LC-22Si**, and **LC-30Si**, exposed to LPL at $0.6 \text{ J cm}^{-2} \text{ min}^{-1}$, at temperatures between $70 - 95 \text{ }^\circ\text{C}$. In order to describe the phenomena and allow comparison of the different experiments and materials, the DR evolution was fitted to a single exponential saturation function $DR = DR_{max}(1 - e^{-t/\tau})$, in which DR_{max} is the calculated dichroic ratio after infinite exposure, t is the exposure time (min), and τ is the characteristic time to reach saturation (min). In order to more accurately compare the different LCs, the fitted alignment parameters were also plotted as a function of the reduced temperature $T_R = T/T_C$, with T_C the clearing temperature of the (all-*trans*) liquid crystal (Figure 13).

For **LC-14Si**, no order is photoinduced for temperatures below $80 \text{ }^\circ\text{C}$ ($DR_{max} = 0$). At $85 \text{ }^\circ\text{C}$, there is a limited induction of order ($DR_{max} = 0.31$), and at $90 \text{ }^\circ\text{C}$ and $95 \text{ }^\circ\text{C}$ a high degree of Az order is achieved around the preferential alignment direction ($DR_{max} = 0.84$). In contrast, **LC-30Si** reaches saturation DR values which are not so dependent on temperature, at the whole explored temperature range from $70 \text{ }^\circ\text{C}$ ($DR_{max} = 0.52$) to $85 \text{ }^\circ\text{C}$ ($DR_{max} = 0.70$). **LC-22Si** represents the intermediate case. The characteristic times (Figure 13b) are also a function of temperature, with very fast alignment just under T_C ($T_R > 0.85$), and slower molecular order build up at lower temperatures. Also in this case, the dependence is less marked in the large ODMS chain material **LC-30Si**. For each of the LCs, dewetting of the film occurred close to the clearing point ($T_R > 0.9$), which was observed by a decreased overall UV-vis absorbance. Likely, the point of dewetting coincides with the effective clearing temperature under irradiation, which is reduced by the presence of *cis* isomers in the photo-stationary state and concurrent photo-fluidization by irradiation, to result in a more mobile isotropic phase.

Together, it is observed that the highest degree of order (high DR_{max}) can be achieved fast (low τ) just below the dewetting conditions (Figure 13), where the system has the highest mobility, which suggests that the dominant energetic barrier in the alignment process is the destabilization of the LC domains.^[37,57] Moreover, the processing window for an optimal alignment is broadened by increased ODMS fractions (**LC-14Si** < **LC-22Si** < **LC-30Si**), which is in agreement with the observation that higher ordered phases are more able to resist photo-induced perturbation.^[44] Combined with the observations of a lower T_C and a lower DR_{max} (at the optimum T conditions, just below the dewetting conditions) for increased ODMS fractions, this suggests that the ODMS lowers the packing ability of Az moieties within each cylinder,

and hence, lowers the energetic barrier to domain destabilization required for alignment. Perhaps counterintuitively, this means that the lower order of Az moieties within the cylinders could be beneficial towards achieving a more effective alignment of nanostructures on a larger length scale.

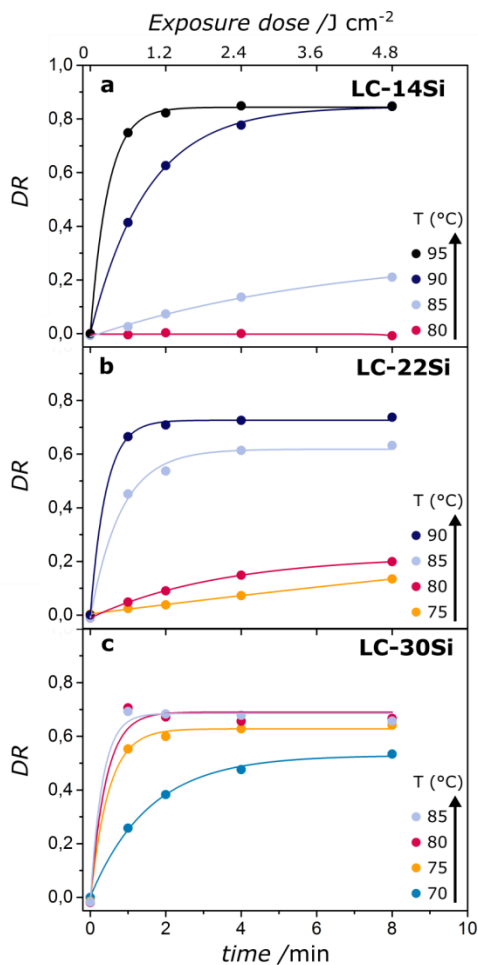


Figure 12. Polarized UV-vis spectroscopic data for LC-14Si (a), LC-22Si (b), and LC-30Si (c) thin films aligned at various temperatures using linearly polarized light at $0.6 \text{ J min}^{-1} \text{ cm}^{-2}$. The irradiation time and corresponding dose are indicated in the graphs. The lines correspond to exponential saturation fits.

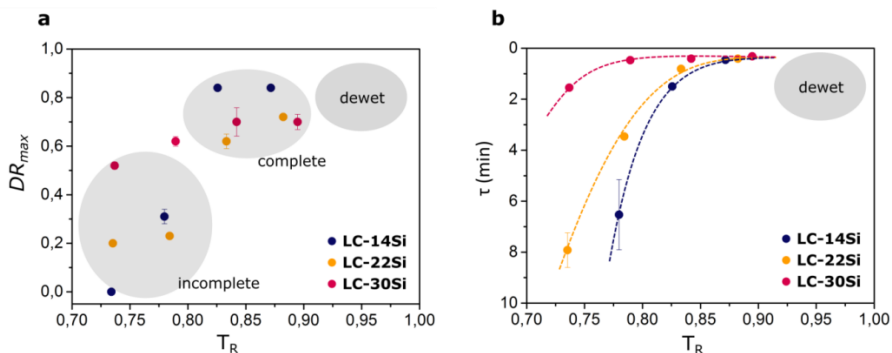


Figure 13. Temperature-dependent DR_{max} (a) and characteristic time τ (b) for the in-plane alignment of the ODMS liquid crystals obtained by polarized UV-vis spectroscopic measurements. The dotted lines serve as a guide to the eye.

Finally, the out-of-plane alignment process was investigated by GIXRD for a thin film (~ 150 nm) of **LC-30Si** (Figure 14), which was selected for its comparatively larger processing window (Figure 13). Prior to irradiation and at room temperature, azimuthal integration around the primary reflection ($1.45 \text{ nm}^{-1} < q < 1.55 \text{ nm}^{-1}$) (Figure 14a), results in a strong signal at $\varphi = 30^\circ$, stemming from the in-plane oriented LC cylinders. The LC film was subsequently exposed to unpolarized light (455 nm , $0.6 \text{ J min}^{-1} \text{ cm}^{-2}$) at various temperatures and for extended periods (60 min) to ensure equilibrium was reached. At 75°C , the reflections are broadened (Figure 14b), suggesting that the in-plane domains are perturbed and their orientation is less well-defined. This effect is further highlighted by the greatly diminished diffraction intensity of the first order ($1\ 0$) ($q = 1.51 \text{ nm}^{-1}$) and second order ($2\ 0$) ($q = 2.96 \text{ nm}^{-1}$) reflections perpendicular to the substrate ($q_y = 0$) (Figure 15a). At 80°C , this effect becomes more pronounced, and additional reflections appear at $\varphi = 0^\circ$ (Figure 14e), where $q_z = 0$ (Figure 15b). The reflections are situated at $q = 1.51 \text{ nm}^{-1}$, $q = 2.54 \text{ nm}^{-1}$, $q = 2.93 \text{ nm}^{-1}$, which are indexed as the $(0\ 1)$, $(1\ 1)$, and $(0\ 2)$ reflections respectively, indicating unequivocally the presence of out-of-plane orientated LC cylinder domains.^[32, 58] These domains are present alongside in-plane oriented domains (Figure 14e), and hence this state is intermediate. At higher temperatures, the fraction of out-of-plane domains is increased. At 90°C , the intensity corresponding to the in-plane oriented domains is significantly diminished, indicating that the domains are almost exclusively out-of-plane (Figure 14d). At 95°C , a drop in scattering intensity from all reflections was observed, likely due to the dewetting of the film (data not shown). Similar to the in-plane alignment, the optimal temperature for out-of-plane photo-alignment is just under T_c . However, when compared to the in-plane alignment of LC cylinders, it is clear that the processing

window for obtaining out-of-plane oriented LC cylinders is much narrower. Unfortunately, after halting the irradiation and cooling down to RT, the out-of-plane alignment partially returned to the in-plane alignment (Figure 16), an interface effect which has been observed in previous studies.^[58,59] These finding suggests a strong competition between the photo-induced out-of-plane orientation and the thermodynamically stable in-plane orientation. It shows that obtaining the out-of-plane orientation of cylinders is challenging due to the intrinsic surface energy mismatch between the mesogenic core and ODMS coils.^[48, 60]

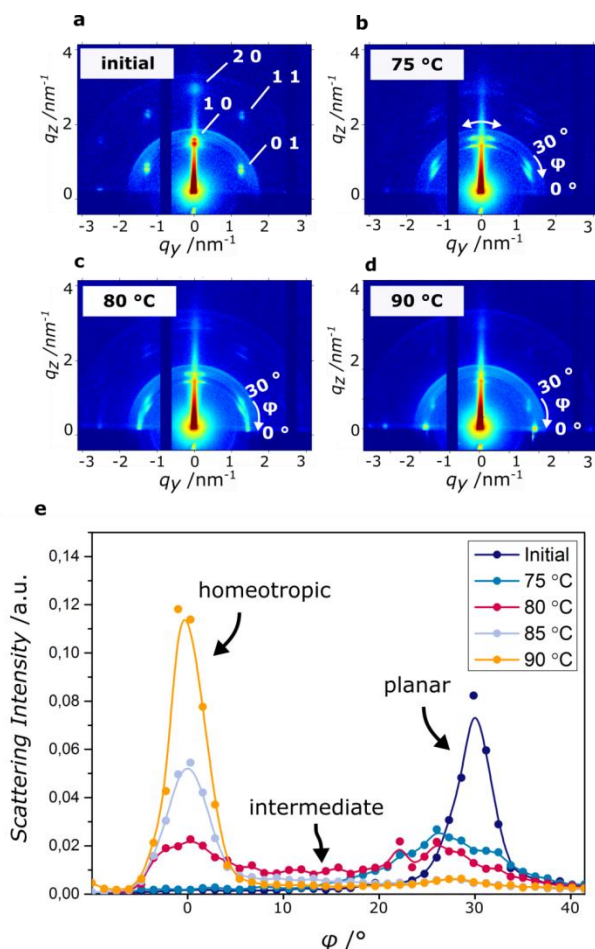


Figure 14. Out-of-plane alignment with unpolarized light: 2D GIXRD profiles of a LC-30Si thin film before (a) and after photo-alignment with unpolarized light at various temperatures (b-d); azimuthal integration over the primary (1 0) reflection (e).

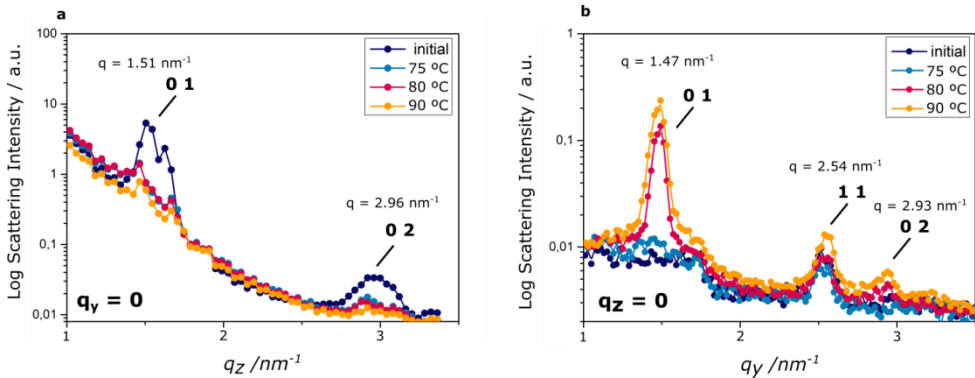


Figure 15. Line-cut integrations along q_z ($q_y = 0$) (a) and along q_y ($q_z = 0$) (b) obtained from 2D GIXRD profiles of a **LC-30Si** thin film before (initial) and after photo-alignment with unpolarized light at various temperatures. The temperatures are indicated in the graph.

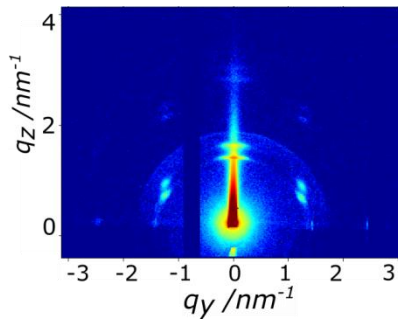


Figure 16. 2D GIXRD profile of a **LC-30Si** thin after photo-alignment with unpolarized light and subsequent cooling to room temperature without irradiation.

4.3. Conclusion

Highly-ordered sub-5 nm nanocylinder arrays were obtained over large areas by the photo-alignment of Az-containing liquid crystals. By using linearly polarized light, in-plane oriented nanocylinders were obtained in thin films. The in-plane photo-alignment was shown to proceed by a mechanism in which the nanocylinders are rapidly oriented, followed by fusion and growth of the re-oriented domains into a mono-domain. When performed just under the clearing temperature of the LC phase, the photo-alignment was demonstrated to proceed most efficiently, reaching completion within minutes. Since the Azs are contained directly in the cylinder nanostructures, the dichroism and nanocylinder order follow the same trend and appear closely linked. However, due to local disorder on the Az length scale, only a moderate dichroism is required to achieve high order on the length scale of the

nanostructures. Interestingly, while the local Az order decreases with increasing ODMS content in the LC series, this broadens the temperature processing window with which aligned nanostructures can be achieved.

Additionally, the LC nanocylinders could be oriented out-of-plane by exposure to unpolarized light, which is a promising alternative to solvent annealing^[61] or surface layers.^[62,63] However, while stable out-of-plane nanostructures were obtained in a cell, the morphology was not retained in thin films. Obtaining stable out-of-plane orientations remains challenging,^[64] particularly for high-etch contrast small molecules such as this. Chemical cross-linking^[34] or cooling through a glass transition^[35] are possible solutions. Overall, these results pave the way for generating defect-free sub-5 nm patterned thin films with three-dimensional orientational control by light. For integrated circuit production in particular, the LC mobility could be key to achieving both the low defect tolerance^[4] and fast alignment for high wafer throughput. Moreover, the planar photo-alignment could be extended to the micro-patterning of distinct domain orientations, or be applied in combination with other alignment methods to achieve the stringent lithography specifications required at future technology nodes.^[65,66]

4.4. Materials & Methods

The synthesis and characterization of the oligo(dimethylsiloxane) liquid crystals can be found in chapter 2.^[48] For thin film preparation, a hydroxy-terminated PDMS homopolymer from Polymer Source with molecular weight 5 kg/mol was applied onto quartz substrates from a 1-2 wt. % solution in heptane, baked at 150 °C for at least 24h, and rinsed with heptane. The liquid crystals were subsequently spin-coated from 10 g/L or 30 g/L solution in heptane (3000 RPM, 45s), resulting in film thicknesses of approximately 40 nm and 150 nm, as determined by ellipsometry. Linearly polarized light was obtained from a 455 nm LED (Thorlabs) equipped with a dichroic polarizing sheet (Polarizer Sheet XP44 - Linear Polarizer; ITOS GmbH, Mainz, Germany). The light intensity was 10.0 mW/cm². For bulk photo-alignment, the samples were heated to the isotropic phase and then slowly cooled (0.1 °C min⁻¹) under irradiation. In thin films, the photo-alignment was performed below the LC clearing temperature to avoid dewetting. Unless otherwise indicated, the thin film photo-alignment was performed at 85 °C. X-ray scattering measurements were performed on a Ganesha lab instrument equipped with a GeniX-Cu ultralow divergence source producing X-ray photons with a wavelength of 1.54 Å and a flux of 1x10⁸ phs⁻¹. Scattering patterns were collected using a Pilatus 300 K silicon pixel detector. The beam center and the q range were calibrated using the diffraction

peaks of silver behenate. Bulk XRD was performed on samples sealed in a 1mm glass capillary. GIXRD was performed at the critical angle ($\sim 0.16^\circ$). This may result in shadow peaks at higher q due to reflection + diffraction events just above the critical angle. The sample to detector distance was 91 mm for wide-angle measurements and 441 mm for medium-angle measurements. Time resolved measurements were the average of 60 s of exposure. The AFM data were recorded in ambient conditions using a Dimension ICON atomic force microscope (Bruker Nano Inc., Santa Barbara, CA) fitted with an NCHV silicon probe (Bruker, spring constant 42 N/m and a resonance frequency 320 kHz).

4.5. References

- [1] C. M. Bates, M. J. Maher, D. W. Janes, C. J. Ellison, C. G. Willson, *Macromolecules* **2014**, *47*, 2.
- [2] A. Nunns, J. Gwyther, I. Manners, *Polymer* **2013**, *54*, 1269.
- [3] S.-J. Jeong, J. Y. Kim, B. H. Kim, H.-S. Moon, S. O. Kim, *Mater. Today* **2013**, *16*, 468.
- [4] J. Bang, U. Jeong, D. Y. Ryu, T. P. Russell, C. J. Hawker, *Adv. Mater.* **2009**, *21*, 4769.
- [5] S.-M. Yang, S. G. Jang, D.-G. Choi, S. Kim, H. K. Yu, *Small* **2006**, *2*, 458.
- [6] X. Yu, K. Yue, I. F. Hsieh, Y. Li, X. H. Dong, C. Liu, Y. Xin, H. F. Wang, A. C. Shi, G. R. Newkome, R. M. Ho, E. Q. Chen, W. B. Zhang, S. Z. Cheng, *Proc Natl Acad Sci USA* **2013**, *110*, 10078.
- [7] Y. H. Kim, D. K. Yoon, H.-T. Jung, *J. Mater. Chem.* **2009**, *19*, 9091.
- [8] C. Tschierske, *J. Mater. Chem.* **2001**, *11*, 2647.
- [9] C. Tschierske, *Angew. Chem.-Int. Ed.* **2013**, *52*, 8828.
- [10] J. V. Barth, G. Costantini, K. Kern, *Nature* **2005**, *437*, 671.
- [11] G. M. Whitesides, B. Grzybowski, *Science* **2002**, *295*, 2418.
- [12] C. L. Gonzalez, C. W. M. Bastiaansen, J. Lub, J. Loos, K. Lu, H. J. Wondergem, D. J. Broer, *Adv. Mater.* **2008**, *20*, 1246.
- [13] M. Zhou, T. J. Kidd, R. D. Noble, D. L. Gin, *Adv. Mater.* **2005**, *17*, 1850.
- [14] X. Feng, M. E. Tousley, M. G. Cowan, B. R. Wiesenaus, S. Nejati, Y. Choo, R. D. Noble, M. Elimelech, D. L. Gin, C. O. Osuji, *ACS Nano* **2014**, *8*, 11977.
- [15] B. R. Kaafarani, *Chem. Mater.* **2011**, *23*, 378.
- [16] R. Ruiz, H. M. Kang, F. A. Detchevery, E. Dobisz, D. S. Kercher, T. R. Albrecht, J. J. de Pablo, P. F. Nealey, *Science* **2008**, *321*, 936.
- [17] T. Thurn-Albrecht, J. Schotter, C. A. Kastle, N. Emley, T. Shibauchi, L. Krusin-Elbaum, K. Guarini, C. T. Black, M. T. Tuominen, T. P. Russell, *Science* **2000**, *290*, 2126.
- [18] S. Park, D. H. Lee, J. Xu, B. Kim, S. W. Hong, U. Jeong, T. Xu, T. P. Russell, *Science* **2009**, *323*, 1030.
- [19] C. Sinturel, F. S. Bates, M. A. Hillmyer, *ACS Macro Lett.* **2015**, *4*, 1044.
- [20] C. M. Bates, F. S. Bates, *Macromolecules* **2017**, *50*, 3.

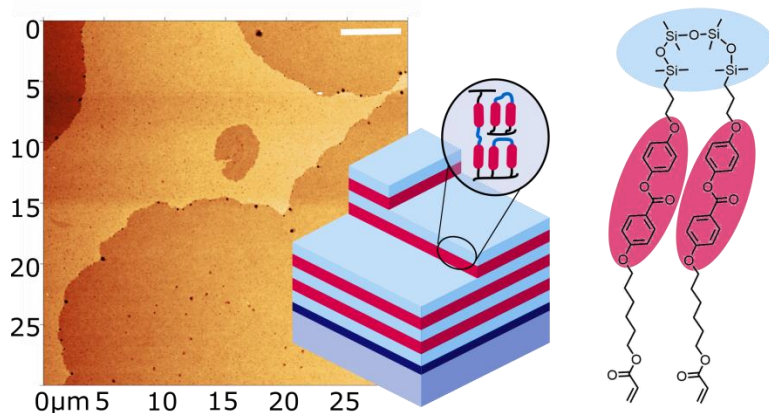
- [21] H. Siebert, I. Quijada-Garrido, J. Vermant, L. Noirez, W. R. Burghardt, C. Schmidt, *Macromol. Chem. Phys.* **2007**, *208*, 2161.
- [22] R. H. Zha, B. F. de Waal, M. Lutz, A. J. Teunissen, E. W. Meijer, *J. Am. Chem. Soc.* **2016**, *138*, 5693.
- [23] J. C. Wittmann, P. Smith, *Nature* **1991**, *352*, 414.
- [24] M. Hara, S. Nagano, T. Seki, *J. Am. Chem. Soc.* **2010**, *132*, 13654.
- [25] H. K. Bisoyi, Q. Li, *Chem. Rev.* **2016**, *116*, 15089.
- [26] K. Ichimura, *Chem. Rev.* **2000**, *100*, 1847.
- [27] T. Seki, *J. Mater. Chem. C* **2016**, *4*, 7895.
- [28] Y. Zakrevskyy, J. Stumpe, C. F. J. Faul, *Adv. Mater.* **2006**, *18*, 2133.
- [29] S. Pan, M. Ni, B. Mu, Q. Li, X.-Y. Hu, C. Lin, D. Chen, L. Wang, *Adv. Funct. Mater.* **2015**, *25*, 3571.
- [30] H. Monobe, K. Awazu, Y. Shimizu, *Adv. Mater.* **2006**, *18*, 607.
- [31] D. K. Yoon, S. R. Lee, Y. H. Kim, S.-M. Choi, H.-T. Jung, *Adv. Mater.* **2006**, *18*, 509.
- [32] K. Kwon, J. M. Ok, Y. H. Kim, J.-S. Kim, W.-B. Jung, S.-Y. Cho, H.-T. Jung, *Nano Lett.* **2015**, *15*, 7552.
- [33] J. Cattle, P. Bao, J. P. Bramble, R. J. Bushby, S. D. Evans, J. E. Lydon, D. J. Tate, *Adv. Funct. Mater.* **2013**, *23*, 5997.
- [34] X. Feng, S. Nejati, M. G. Cowan, M. E. Tousley, B. R. Wiesenaus, R. D. Noble, M. Elimelech, D. L. Gin, C. O. Osuji, *ACS Nano* **2016**, *10*, 150.
- [35] Y. Morikawa, T. Kondo, S. Nagano, T. Seki, *Chem. Mater.* **2007**, *19*, 1540.
- [36] K. Fukuhara, Y. Fujii, Y. Nagashima, M. Hara, S. Nagano, T. Seki, *Angew. Chem.-Int. Ed.* **2013**, *52*, 5988.
- [37] M. Sano, S. Nakamura, M. Hara, S. Nagano, Y. Shinohara, Y. Amemiya, T. Seki, *Macromolecules* **2014**, *47*, 7178.
- [38] T. Seki, *Polym. J.* **2014**, *46*, 751.
- [39] H. F. Yu, T. Iyoda, T. Ikeda, *J. Am. Chem. Soc.* **2006**, *128*, 11010.
- [40] T. Seki, *Macromol. Rapid Commun.* **2014**, *35*, 271.
- [41] M. Sano, M. Hara, S. Nagano, Y. Shinohara, Y. Amemiya, T. Seki, *Macromolecules* **2015**, *48*, 2217.
- [42] K. M. Lee, T. J. White, *Macromolecules* **2012**, *45*, 7163.
- [43] T. Ikeda, *J. Mater. Chem.* **2003**, *13*, 2037.
- [44] H. Yu, *J. Mater. Chem. C* **2014**, *2*, 3047.
- [45] S. Nagano, *Chem. Rec.* **2016**, *16*, 378.
- [46] S. Nagano, Y. Koizuka, T. Murase, M. Sano, Y. Shinohara, Y. Amemiya, T. Seki, *Angew. Chem.-Int. Ed.* **2012**, *51*, 5884.
- [47] K. Ichimura, S. Morino, H. Akiyama, *Appl. Phys. Lett.* **1998**, *73*, 921.
- [48] K. Nickmans, J. N. Murphy, B. de Waal, P. Leclère, J. Doise, R. Gronheid, D. J. Broer, A. P. H. J. Schenning, *Adv. Mater.* **2016**, *28*, 10068.
- [49] A. Natansohn, P. Rochon, *Chem. Rev.* **2002**, *102*, 4139.

- [50] J. Garcia-Amoros, A. Szymczyk, D. Velasco, *Phys. Chem. Chem. Phys.* **2009**, *11*, 4244.
- [51] S. Xie, A. Natansohn, P. Rochon, *Chem. Mater.* **1993**, *5*, 403.
- [52] C. Sanchez, R. Alcala, S. Hvilsted, P. S. Ramanujam, *J. Appl. Phys.* **2003**, *93*, 4454.
- [53] T. Ikeda, S. Horiuchi, D. B. Karanjit, S. Kurihara, S. Tazuke, *Macromolecules* **1990**, *23*, 36.
- [54] N. Kawatsuki, H. Takatsuka, T. Yamamoto, *Jpn. J. Appl. Phys.* **2000**, *39*, L230.
- [55] Y. S. Jung, C. A. Ross, *Nano Lett.* **2007**, *7*, 2046.
- [56] Y. Morikawa, S. Nagano, K. Watanabe, K. Kamata, T. Iyoda, T. Seki, *Adv. Mater.* **2006**, *18*, 883.
- [57] A. V. Bogdanov, A. K. Vorobiev, *J. Phys. Chem. B* **2013**, *117*, 13936.
- [58] E. Pouzet, V. D. Cupere, C. Heintz, J. W. Andreasen, D. W. Breiby, M. M. Nielsen, P. Viville, R. Lazzaroni, G. Gbabode, Y. H. Geerts, *J. Phys. Chem. C* **2009**, *113*, 14398.
- [59] V. De Cupere, J. Tant, P. Viville, R. Lazzaroni, W. Osikowicz, W. R. Salaneck, Y. H. Geerts, *Langmuir* **2006**, *22*, 7798.
- [60] J. G. Son, K. W. Gotrik, C. A. Ross, *ACS Macro Lett.* **2012**, *1*, 1279.
- [61] Y. S. Jung, J. B. Chang, E. Verploegen, K. K. Berggren, C. A. Ross, *Nano Lett.* **2010**, *10*, 1000.
- [62] C. M. Bates, T. Seshimo, M. J. Maher, W. J. Durand, J. D. Cushen, L. M. Dean, G. Blachut, C. J. Ellison, C. G. Willson, *Science* **2012**, *338*, 775.
- [63] T. Nakai, D. Tanaka, M. Hara, S. Nagano, T. Seki, *Langmuir* **2016**, *32*, 909.
- [64] Z. Chen, Y.-T. Chan, D. Miyajima, T. Kajitani, A. Kosaka, T. Fukushima, J. M. Lobe, T. Aida, *Nat. Commun.* **2016**, *7*, 13640.
- [65] C. C. Kathrein, W. Bai, J. A. Currihan-Incorvia, G. Lontos, K. Ntetsikas, A. Avgeropoulos, A. Boker, L. Tsarkova, C. A. Ross, *Chem. Mater.* **2015**, *27*, 6890.
- [66] ITRS, **2013**.

Chapter 5

Reactive oligo(dimethylsiloxane) mesogens and their micropatterned nanostructured thin films

Abstract. *Oligo(dimethylsiloxane)-based reactive mesogens were prepared and shown to form room-temperature smectic phases which were 'frozen-in' by photopolymerization. Homeotropically aligned, nanostructured thin films were obtained by spin-coating, and micropatterning was demonstrated. These hybrid reactive mesogens are suitable for the preparation of aligned nanostructured polymer thin films with potential applications ranging from stimuli responsive coatings to nanoporous membranes.*



This chapter is based on:

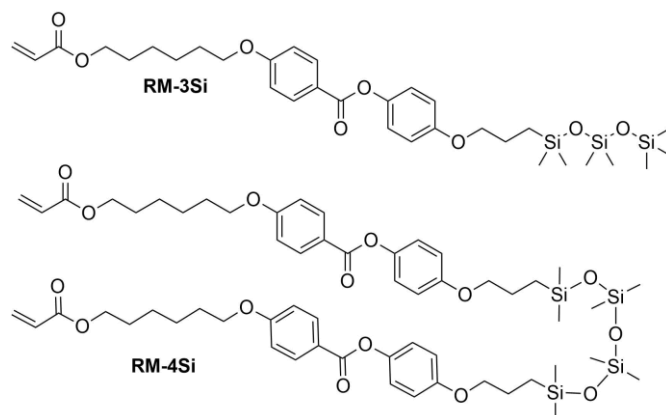
K. Nickmans, P. Leclère, J. Lub, D. J. Broer, A. P. H. J. Schenning, *Soft Matter* **2017**, *13*, 4357.

5.1. Introduction

While flat panel displays were the initial driving force behind the development of reactive mesogens (RMs), these materials are currently finding applications as functional nanostructured materials,^[1-3] for lab-on-a-chip systems,^[4] responsive coatings,^[5] actuators,^[6] membranes,^[7-9] and biosensors.^[10] In general, these applications rely on the self-assembly of reactive mesogenic precursors into an ordered LC state, their alignment into macroscopically oriented nanostructures, and the ‘freezing-in’ of the ordered state through polymerization to form temperature stable nanostructured polymers.^[11-14] In principle, the properties and functionality of the polymers can be tuned by the modification of the structures of the reactive mesogens.

Hybrid reactive mesogens containing organic and inorganic segments such as oligo(dimethylsiloxane) (ODMS) are of interest for various reasons.^[15] For example, due to the incompatibility and large surface tension mismatch of ODMS with most organic materials, nanophase segregation is promoted ^[16-18] which leads to gel formation,^[19] and highly ordered nanostructured morphologies.^[20-23] Since ODMS can act as a precursor to inorganic silicon oxides through plasma oxidation, these materials could act as templates in porous membranes or nanolithography (see chapter 1).^[20,24] Furthermore, the low glass transition temperature leads to self-healing properties,^[25] and advantageous thermoplastic behavior for polymeric actuator materials requiring a large response.^[26-29] While these materials are typically prepared in cells using alignment layers,^[6] the alignment and polymerization in thin films is crucial for smart coating applications. ODMS has been incorporated into calamitic-,^[30-33] discotic-,^[34-36] and bent-core mesogens,^[21,37] but anisotropic thin film coatings consisting of ODMS RMs have not been reported.

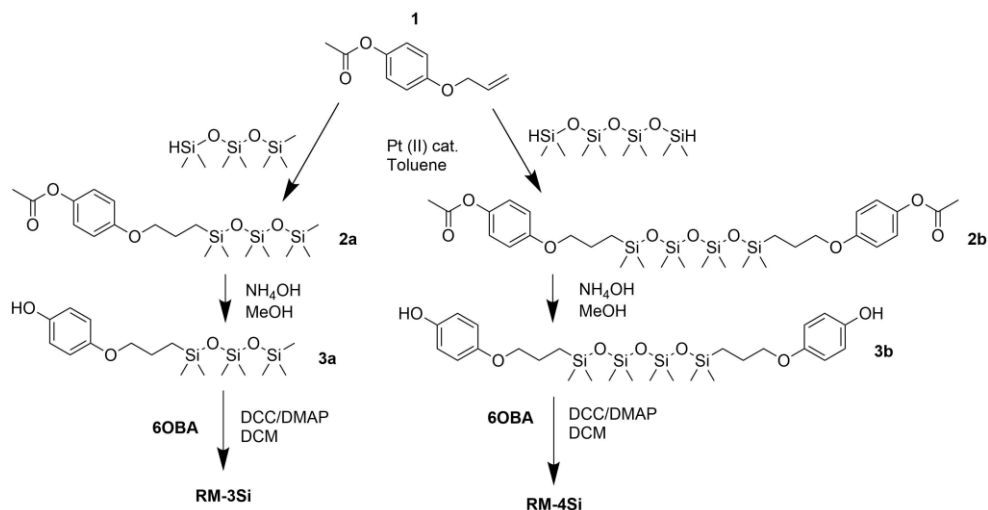
In this chapter, we prepared a mono-reactive liquid crystal with an ODMS end group, and a di-reactive liquid crystal based on an ODMS bridge **RM-3Si** and **RM-4Si**, respectively, (Scheme 1). The synthesis and characterization of the novel liquid crystals is presented, as well as a characterization of the liquid crystalline behavior of the mesogens and their derived polymers. The reactive mesogens were aligned in thin films driven by the low surface energy of oligo(dimethylsiloxane), and photopolymerized into nanostructured polymer films.



Scheme 1. Molecular structures of the reactive ODMS mesogens **RM-3Si** and **RM-4Si**.

5.2. Results & Discussion

Reactive mesogens **RM-3Si** and **RM-4Si** (Scheme 1) were synthesized according to **Scheme 2**. 4-(allyloxy)phenyl acetate **1** was prepared by acetylation of 4-(allyloxy)phenol.^[38] Protection of this phenol as an acetate was required for the subsequent catalytic hydrosilylation reaction with siloxane hydrides. To prepare **RM-3Si**, 1.1 eq of **1** was reacted with 1.0 eq. of 1,1,1,3,3,5,5-heptamethyltrisiloxane in the presence of dichloro(1,5-cyclooctadiene)platinum(II) in toluene, overnight at 60 °C in a Schlenk setup, to give **2a** (yield 50 %). The acetate protecting group was removed with ammonium hydroxide in methanol to obtain **3a** as a clear viscous fluid (yield 71%). Procedures described in the literature were used to obtain 4-(6-acryloyloxyhexyloxy)benzoic acid^[12] (6OBA), which was reacted with 1.0 eq. of **3a** in an esterification reaction using dicyclohexylcarbodiimide (DCC) and 4-dimethylaminopyridine (DMAP) to obtain **RM-3Si** (yield 28%). For preparation of the **RM-4Si**, 2.2 eq **1** was reacted with 1.0 eq. of 1,1,3,3,5,5,7,7-octamethyltetrasiloxane under identical conditions as the preparation of **2a** to obtain **2b** (yield 67%). After deprotection **3b** was obtained (yield 87%) which was reacted with 2.0 eq. 6OBA to form the desired product **RM-4Si** (yield 89%). The ODMS RMs were purified by column chromatography and characterized by TLC, NMR, TGA, and MALDI-TOF MS.



Scheme 2. Synthetic routes for the preparation of reactive mesogens **RM-3Si** and **RM-4Si**.

To investigate the LC phase behavior, the LCs were analyzed by differential scanning calorimetry (DSC), X-ray diffraction (XRD), and polarized optical microscopy (POM). Figure. 1a shows the DSC data obtained on second cooling of the two compounds. The phase transition temperatures of **RM-3Si** are $l \rightarrow 31.7 \text{ }^\circ\text{C}$ (7.93 J g^{-1}) $\rightarrow S_A \rightarrow 0.39 \text{ }^\circ\text{C}$ (36.79 J g^{-1}) $\rightarrow K$. Meanwhile, the phase transitions for **RM-4Si** are $l \rightarrow 58.4 \text{ }^\circ\text{C}$ (11.22 J g^{-1}) $\rightarrow S_A \rightarrow -4.5 \text{ }^\circ\text{C}$ (13.93 J g^{-1}) $\rightarrow K$. Here, K, S_A, and I denote the crystalline, smectic A, and isotropic phases, respectively, and the associated enthalpy changes are given in parentheses. In both cases, the compounds are liquid crystalline at room temperature. Compared to similar LCs without an ODMS segment, crystallization is suppressed,^[39] an effect likely due to the high flexibility of the siloxane oligomers.^[33,40] For the same reason, the isotropization temperature is suppressed.^[16] Figure. 1b shows the room temperature X-ray diffraction (XRD) spectra measured in both wide-angle and medium-angle configurations on kapton tape (see methods). For **RM-3Si**, two sharp diffraction peaks are found at medium angles ($q = 1.58 \text{ nm}^{-1}$ and $q = 3.15 \text{ nm}^{-1}$), which corresponds to a periodic layered structure with an interlayer distance of $d = 4.0 \text{ nm}$. Since this value is approximately equal to the molecular length (determined by MM2 molecular simulation), it follows that the LC phase of **RM-3Si** can be assigned as a smectic A phase. For **RM-4Si**, two sharp diffraction peaks are found at medium angles ($q = 1.71 \text{ nm}^{-1}$ and $q = 3.42 \text{ nm}^{-1}$), corresponding to a layered structure with an interlayer distance of $d = 3.6 \text{ nm}$. Since the interlayer distance is approximately equal to half the length of the extended dimer, the LC phase of **RM-4Si** is assigned as a smectic A phase, in which the siloxane bridge and organic tail moieties are partially mixed.^[32,41,42] For both LCs, a broad peak is observed in the wide-angle region, signifying a combination of

siloxane-siloxane interactions at 0.70 nm,^[37] organic-organic interactions at 0.45 nm, and intermediate organic-siloxane interactions at 0.55 nm. This indicates that there is partial nanophase segregation between siloxane and organic units, which is presumably the driving force behind the formation of the smectic layered morphologies,^[16] rather than the lower-order nematic ordering.^[39] Schematic representations of the liquid crystal phases are included in Figure 1c, in which the mesogenic core (red) form layers with the partially phase separated siloxane (blue) and reactive aliphatic tails (black).

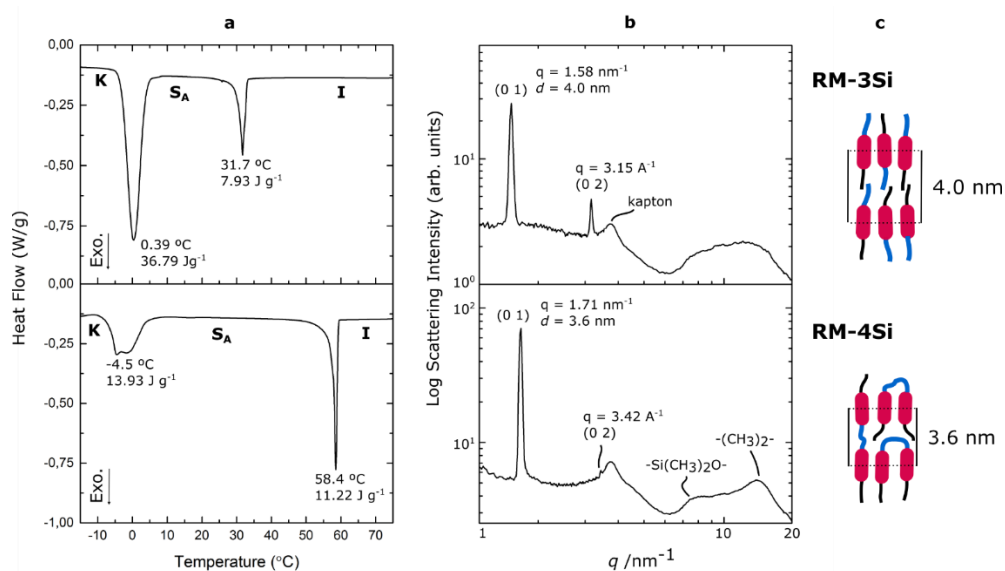


Figure 1. a) DSC thermographs and b) room-temperature x-ray diffraction spectra of the reactive siloxane liquid crystals. The assigned Miller indices and the respective intermolecular scatterings are indicated, as well as the assigned lattices. c) Schematic representation of the room-temperature smectic phases formed by the liquid crystals; mesogenic core (red), ODMS (blue) and reactive aliphatic tails (black).

To photopolymerize the reactive hybrid mesogenes, a cell ($\sim 7 \mu\text{m}$) was filled with the LCs containing a small amount of photoinitiator. When observed under crossed polarizers in a POM experiment (Figure 2a), the LCs exhibit a fan-shape texture characteristic of the smectic A phase. The cell was subsequently exposed to UV for 20 mins at room temperature. Under these conditions, Fourier Transform Infrared Spectroscopy (FTIR) indicated the complete conversion of reactive acrylate groups, by the disappearance of the peak at 1635 cm^{-1} that corresponds to the $\text{C}=\text{C}$ bond of the acrylates (Figure 3). The birefringence is largely maintained in the polymerized samples (Figure 2b), indicating the ‘freeze-in’ of the S_A phase in the polymeric

material. The polymerized samples were further heated under the POM to explore the stability of the LC phase (Figure 2c). In this case, the thermal transitions of the monomers were not observed. Instead, the linear **RM-3Si** polymer showed a reversible isotropic phase transition at 175 °C, which represents a significant increase compared to the corresponding monomer. The crosslinked liquid crystal network of **RM-4Si** did not become isotropic within the studied temperature range (< 250 °C). However, it showed a reversible phase transition at 175 °C, accompanied by a lower birefringence. DSC performed on the polymeric material further confirm the stability of the polymerized films (Figure 4).

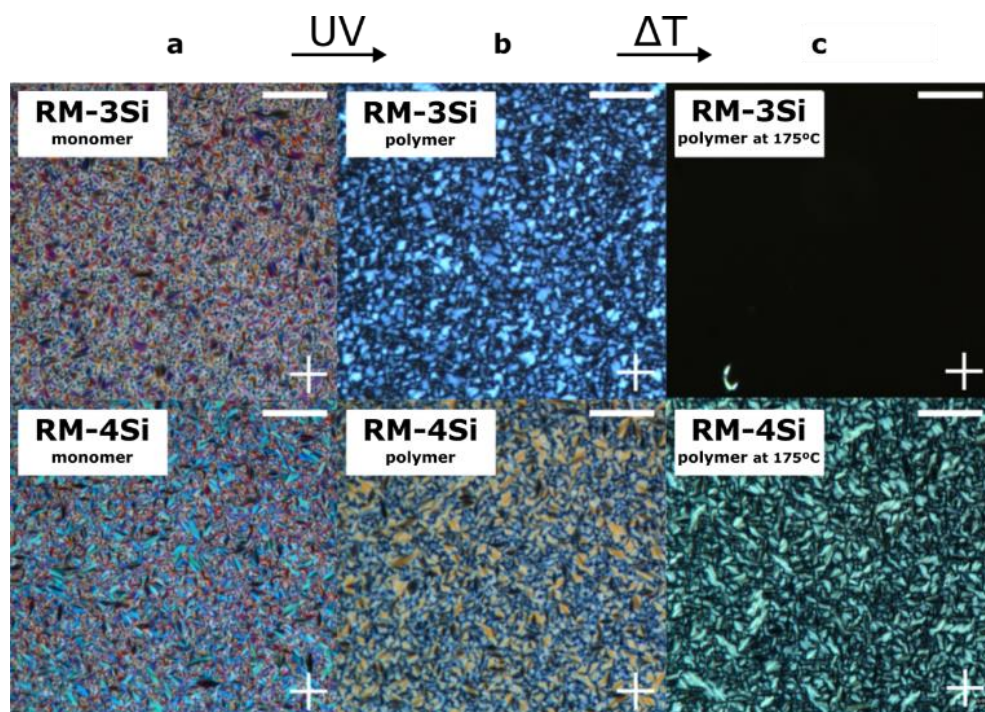


Figure 2. POM images obtained between crossed polarizers of the LCs in a cell a) before photopolymerization, b) after photopolymerization, and c) after heating the samples. Crossed polarizer axes are indicated with a cross. All scale bars: 100 μm .

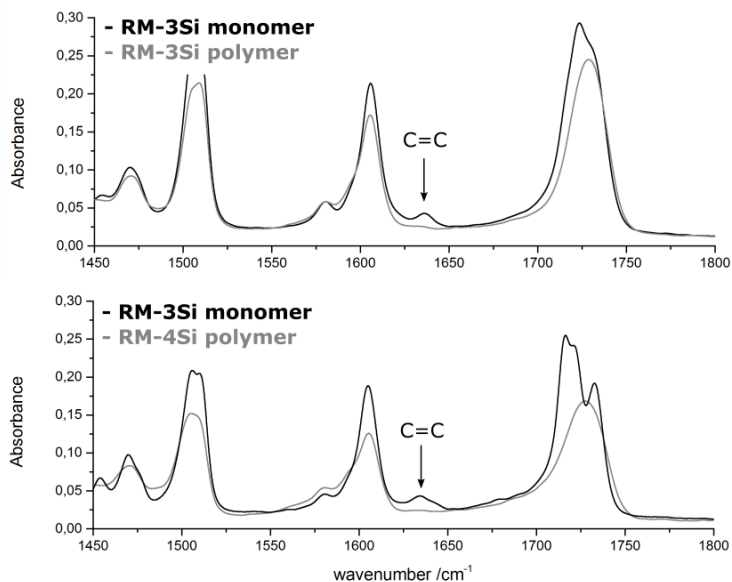


Figure 3. FTIR data for the reactive mesogens and corresponding polymers. Upon photopolymerization the C=C bond of the acrylate groups at 1635 cm⁻¹ disappears.

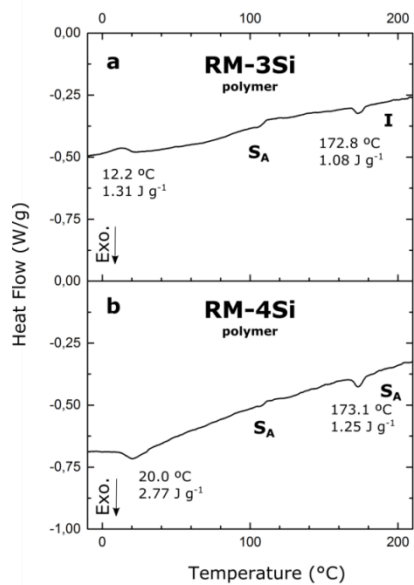


Figure 4. DSC thermographs of a) RM-3Si, and b) RM-4Si, after photopolymerization.

In order to prepare nanostructured thin films, dilute solutions of **RM-4Si** were spin coated on a Si wafer containing an Anti-Reflective Coating (ARC), and subsequently polymerized (see experimental). The solution concentration was varied between 0.25 wt.% and 1 wt. %, to yield film thicknesses after polymerization between 11 nm (~ 3 smectic layers) and 60 nm (~ 17 smectic layers) (Figure 5). Across the thickness range, the static contact angle (H_2O) of the polymerized films was equal to 105° (Figure 5). Since this value is approximate to the contact angle for PDMS ($\sim 107^\circ$),^[43] it suggests the predominant presence of siloxanes at the air interface.

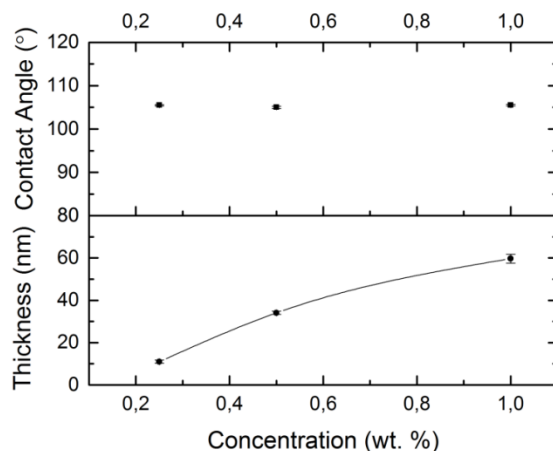


Figure 5. Film thickness profiles and static contact angle of polymerized **RM-4Si** thin films, as function of the spin-coating concentration (chloroform).

The polymerized film of 60 nm thickness was studied with wide-angle grazing-incidence x-ray diffraction (GIWAXS) to determine the through-film morphology (Figure 6a). In the small-angle region, scattering peaks are observed at $q = 1.84 \text{ nm}^{-1}$ and $q = 3.66 \text{ nm}^{-1}$, perpendicular to the substrate, corresponding to a layered structure with a periodicity of 3.4 nm. Hence, the smectic LC phase is maintained in the thin polymerized film, and organized preferentially in a homeotropic orientation. Likely, the homeotropic orientation is driven by the low surface energy of PDMS ($\gamma_{\text{PDMS}} = 20.5 \text{ mN/m}$),^[43] as previously reported for siloxane-based LC thin films.^[20] The broad reflections at $7 \text{ nm}^{-1} < q < 14 \text{ nm}^{-1}$ signify that the isotropic nature of the respective intermolecular interactions (siloxane-siloxane and organic-organic) is maintained upon photopolymerization. Comparison to the sample prior to photopolymerization (Figure 6b) reveals that the smectic LC order is maintained upon photopolymerization.

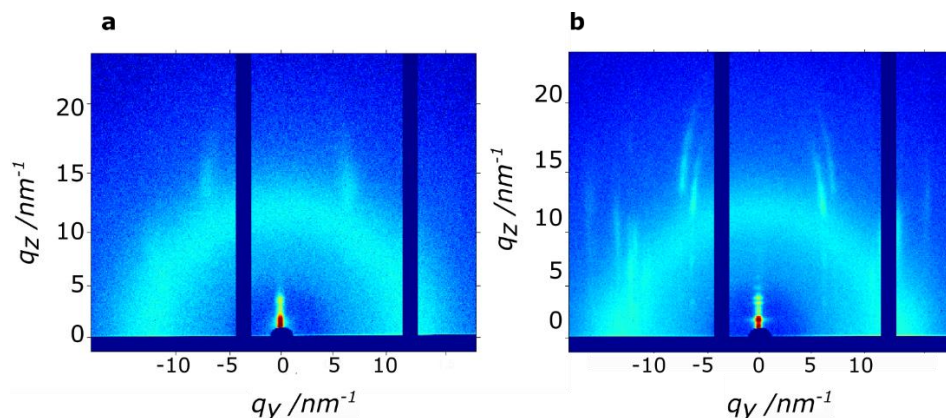


Figure 6. Grazing-incidence x-ray diffraction data, obtained before (a) and after (b) photopolymerization, of a 60 nm **RM-4Si** thin film. The data was obtained around the critical angle and at room temperature.

Low-resolution AFM height images of the 60 nm thin film show a layered hole-island morphology (Figure 7a) with a step-height of approximately 3.5 nm, confirming the presence of smectic layers at the film surface. Together, these findings unequivocally demonstrate the presence of 1D layered structures with the dimension corresponding to the length of the RM. A schematic representation of the lamellar sheets is depicted in Figure 7b.

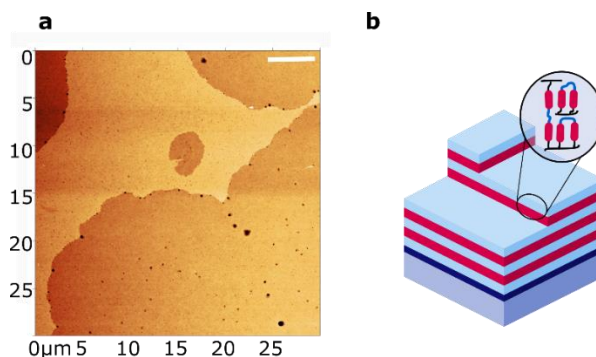


Figure 7. a) Low-resolution AFM height image, obtained at room temperature, of a photopolymerized 60 nm **RM-4Si** thin film. Scale bar: 5 μm . b) Schematic representation of the nanostructured thin film.

While the films are generally smooth (RMS roughness ~ 0.55 nm), holes of approximately 10 – 100 nm diameter are present on the film surface. High-resolution AFM images, obtained in peakForce tapping mode, further indicate the presence of small defects (5 – 20 nm diameter) on the film surface (Figure 8).

Several areas are marked by a lower adhesion compared to the rest of the film, which suggests they consist of a different chemical composition.

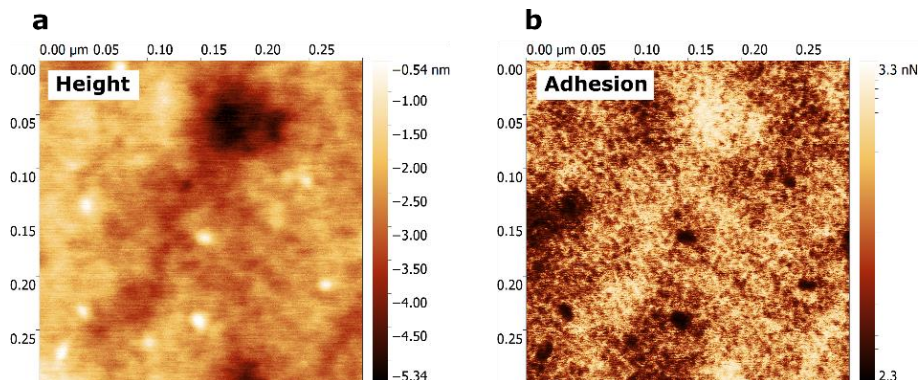


Figure 8. High-resolution Peakforce tapping AFM data, a) height, and b) adhesion, for a polymerized **RM-4Si** thin film of a thickness of 60 nm.

Finally, micropatterning was achieved by exposing a 60 nm film of **RM-4Si** through a mask (25 μm diameter circular holes). After the mask exposure, the nonpolymerized material was removed by developing the film in the casting solvent. Optical microscopy revealed the presence of circular features corresponding to the dimensions of the mask (Figure 9a). Interestingly, the features are surrounded by an additional structure at the edges, observable as a yellow ring. Since the optical contrast arises due to height differences in the film, the film was further characterized by optical profilometry (Figure 9b). Here, the rings appear as protrusions which rise up to 50 nm above the circular features, which is remarkable considering the initial height of the film (60 nm). This phenomenon is likely due to the diffusion of reactive mesogens to areas of low concentration during the polymerization process.^[44] A cross-section across the circular features (black line) (Figure 9c) indicates that the height of the circular features is approximately 30 - 40 nm, which is lower than the initial height of the film (60 nm). This may be due to (limited) polymerization in the unexposed areas due to diffuse light.

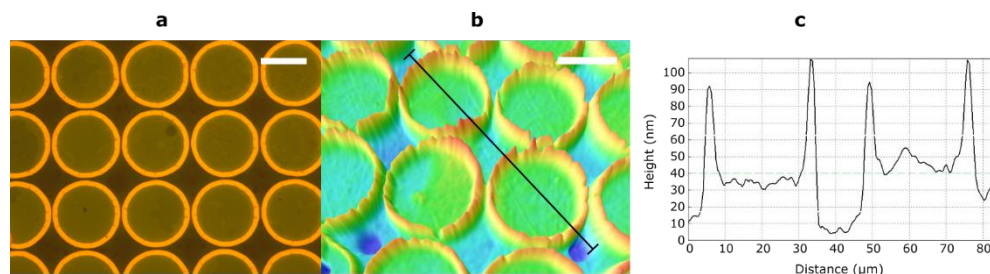


Figure 9. Characterization of a micropatterned thin film of **RM-4Si** of 60 nm thickness. a) Optical microscopy image. b) Optical profilometric image with cross-section (black line) c) Cross-section profile corresponding to (b). Scale bars: 20 μm

5.3. Conclusion

In this chapter, an oligo(dimethylsiloxane)-based reactive monoacrylate and a similar diacrylate were prepared and fully characterized. The room-temperature smectic phases formed by these compounds were shown to be ‘frozen-in’ through photopolymerization, resulting in the preparation of stable nanostructured polymers. Aligned thin films were fabricated by spin-coating and subsequent photopolymerization. These films exhibit smectic layers aligned parallel throughout the film (GIWAXS) and at the surface (AFM), likely driven by the low surface energy of the ODMS. Finally, the *in-situ* polymerization approach allows for micropatterning. Hence, this fabrication method is highly suitable for the preparation of aligned nanostructured polymers with applications as thin film actuators, well-defined membrane materials, or nanolithography. For nanolithography, reactive ODMS mesogens could be used to ‘freeze-in’ desirable morphologies or unstable alignment

5.4. Materials & Methods

The reactive LC mixtures used for the experiments contain the reactive mesogens as well as 2 wt. % of photo initiator 1-hydroxy-cyclohexyl-phenyl ketone (Irgacure 184, Ciba Speciality Chemicals). To make homogenous blends, the components were dissolved in chloroform and the solvent was evaporated. For thin film preparation, dilute solutions were spin coated at 3000 RPM for 45 seconds. For photopolymerization, the LCs were irradiated while under nitrogen atmosphere for 20 minutes, at room temperature with 365 nm light from a Mercury lamp ($\sim 5 \text{ mW cm}^{-2}$). Film thickness was obtained using a Bruker DektakXT stylus profiler. Film thickness was obtained from polymerized films only due to the very soft nature of the as-deposited films. Polarized optical microscopy (POM) was performed with

crossed polarizers using a Leica DM6000M equipped with a DFC420C camera and a Linkam THMS600 hot-stage for temperature control. For characterization of the LC textures, a small amount of LC material was placed between microscope slides, heated to the isotropic phase, and cooled ($5\text{ }^{\circ}\text{C min}^{-1}$) to room temperature. Phase transition temperatures of the reactive mesogens were determined using a TA Instrument Q1000 differential scanning calorimeter (DSC). 3-4 mg of material was hermitically sealed in aluminum pans. The heating and cooling rate was $5\text{ }^{\circ}\text{C min}^{-1}$ and the second cooling curve was used to determine the transition temperatures. X-ray scattering measurements were performed on a Ganesha lab instrument equipped with a GeniX-Cu ultralow divergence source producing X-ray photons with a wavelength of 1.54 \AA and a flux of $1 \times 10^8\text{ phs}^{-1}$. Scattering patterns were collected using a Pilatus 300 K silicon pixel detector. The beam center and the q range were calibrated using the diffraction peaks of silver behenate. Due to the sticky nature of the LCs, XRD samples were prepared by placing a small amount of LC between kapton tape, leading to a background signal at $q = 0.39$. The sample to detector distance was 91 mm for wide-angle measurements and 441 mm for medium-angle measurements, and the spectra were concatenated at $q = 0.36$. Grazing incidence XRD was performed at the critical angle ($\sim 0.18^{\circ}$). The AFM data were recorded in ambient conditions using a Dimension ICON atomic force microscope (Bruker Nano Inc., Santa Barbara, CA) fitted with an NCHV silicon probe (Bruker, spring constant 42 Nm^{-1} and a resonance frequency 320 kHz). Fourier transform infrared spectroscopy (FTIR) spectra were obtained using a FTS 6000 spectrometer from Bio-Rad equipped with Specac Golden gate diamond ATR and were signal-averaged over 50 scans at a resolution of 1 cm^{-1} . Optical profilometric measurements were performed on a Sensofar Plj 2300 microscope equipped with a lens with 150x zoom using blue light.

5.5. Synthetic procedures

4-(allyloxy)phenyl acetate (**1**)

To 1.8 g (12 mmol) of 4-(allyloxy)phenol in 20 ml of dichloromethane was added 1.8 ml of triethylamine. The reaction mixture was stirred under nitrogen atmosphere. The solution was cooled in an ice-water bath. Subsequently 0.8 ml of acetyl chloride in 10 ml of dichloromethane were added dropwise and the reaction mixture was stirred for 10 minutes. The mixture was washed once with 30 ml of water and once with 30 ml of 2 N HCl solution and dried over MgSO_4 . The organic solution was filtered through celite and the solvent was evaporated to yield 2 g of 4-(allyloxy)phenyl acetate (**1**) as a yellow oil. Yield: 86.8%; $^1\text{H-NMR}$ (400 MHz, CDCl_3): δ 7.00 – 6.89 (m, 4H); 6.09-5.96 (m, 1H); 5.41 (dq, 1H); 5.29 (dq, 1H); 4.51 (ddd,

2H); 2.27 (s, 3H). ^{13}C -NMR (100 MHz, CDCl_3): δ 169.82, 156.28, 144.33, 133.20, 122.32, 117.67, 115.33, 69.18, 21.04.

4-(3-(1,1,3,3,5,5,5-heptamethyltrisiloxanyl)propoxy)phenyl acetate (2a)

1.3g (6.76 mmol) of **1** and 1.5g of heptamethyltrisiloxane (6.74 mmol) were brought under Argon atmosphere and dissolved in 7 ml of dry toluene. To this 200 μL of a 1 mg/mL solution in dry DCM of dichloro(1,5-cyclooctadiene)platinum(II) catalyst was added. The mixture was heated to 60 $^\circ\text{C}$ and stirred overnight. After evaporation, the compound was purified by column chromatography on silica gel (n-hexane/ethyl acetate = 16:1 v/v) to yield 1.39 g (3.35 mmol) of the siloxane-acetate (**2a**) as an oil. Yield: 50%; ^1H -NMR (400 MHz, CDCl_3): δ 6.95 – 6.81 (m, 4H); 3.85 (t, 2H); 2.27 (s, 3H); 1.76 (m, 2H); 0.61 (m, 2H); 0.09-0.05 (m, 21H).

4-(3-(1,1,3,3,5,5,5-heptamethyltrisiloxanyl)propoxy)phenol (3a)

1.05g (2.54 mmol) of **2a** was dissolved in 60 mL methanol. 3 mL of ammonium hydroxide (28%) in 10 mL water was added. The mixture was stirred under argon atmosphere overnight at room temperature. Roughly 50 ml of water and 100 ml of diethyl ether were added to the solution and the organic phase was separated. The aqueous phase was extracted twice with roughly 50 mL diethyl ether. The organic fractions were combined and the solvent evaporated. Water remained present, and therefore the sample was extracted twice with 50mL DCM. The sample was dried over magnesium sulfate and solvent removed in vacuo. Purification by column chromatography on silica gel (n-hexane/ethyl acetate = 7:1 v/v) gave 676.4 mg (1.81 mmol, 71%) **3a** as a clear viscous fluid. ^1H -NMR (400 MHz, CDCl_3): δ 6.80 – 6.74 (m, 4H); 3.87 (t, 2H); 1.79 (m, 2H); 0.64 (m, 2H); 0.09-0.05 (m, 21H); ^{13}C -NMR (100 MHz, CDCl_3): δ 153.18, 149.35, 116.02, 115.66, 71.30, 23.28, 14.15, 1.82, 1.28, 1.13.

4-(3-(1,1,3,3,5,5,5-heptamethyltrisiloxanyl)propoxy)phenyl 4-(4-(acryloyloxy)butoxy)benzoate (RM-3Si)

208mg (0.56 mmol) of **3a** was added to 163 mg (0.56 mmol) 4-(6-acryloyloxyhexyloxy) benzoic acid (**6OBA**) and 1 mg of 4-dimethylaminopyridine (DMAP) in a few mL dry DCM. The solution was put under Argon gas and placed in an ice bath. After cooling for several minutes, 115.2 mg (0.56 mmol) of dicyclohexylcarbodiimide DCC dissolved in dry DCM was added to the solution. The reaction was kept for 5 hours, after which the solvent was removed. The crude product was purified on column chromatography on silica gel (n-hexane/ethyl acetate = 10:1 v/v), to yield 100 mg (0.155 mmol) **RM-3Si**. Yield: 28%; ^1H -NMR (400 MHz, CDCl_3): δ 8.13 (d, 2H); δ 7.09 (d, 2H); δ 6.97 – 6.91 (m, 4H); δ 6.40 (d, 1H);

δ 6.12 (m, 1H); δ 5.82 (d, 1H); δ 4.18 (t, 2H); δ 4.03 (t, 2H); δ 3.92 (t, 2H); δ 1.87 – 1.69 (m, 6H); δ 1.56 – 1.45 (m, 4H); δ 0.67 (m, 2H); 0.12-0.04 (m, 21H); $^{13}\text{C-NMR}$ (100 MHz, CDCl_3): δ 153.18, 149.35, 116.02, 115.66, 71.3, 23.28, 14.15, 1.82, 1.28, 1.13. MALDI-TOF ($[\text{M}+\text{Na}]^+$): 669,23 g/mol). MALDI-TOF MS (m/z): $[\text{M}+\text{Na}]^+$ calcd for $\text{C}_{32}\text{H}_{50}\text{O}_8\text{Si}_3$ 669.27, found 669.23.

(((1,1,3,3,5,5,7,7-octamethyltetrasiloxane-1,7-diyl)bis(propane-3,1-diyl))bis(oxy))bis(4,1-phenylene) diacetate (2b)

1.47 g (7.66 mmol) of **1** and 1.03 g (3.64 mmol) of 1,1,3,3,5,5,7,7-octamethyltetrasiloxane were dissolved in 5 ml of dry toluene. To this 500 μL of a 1 mg/mL solution in dry DCM of dichloro(1,5-cyclooctadiene)platinum(II) catalyst was added. The mixture was heated at 60°C and stirred under argon atmosphere for 7h. Solvent was removed and the crude product was purified by column chromatography on silica gel (n-hexane/ethyl acetate = 5:1 v/v) to yield 1.62 g (2.43 mmol, 67%) **2b** as a viscous fluid. $^1\text{H-NMR}$ (400 MHz, CDCl_3): δ 6.99-6.82 (m, 8H); 3.89 (t, 4H); 2.27 (s, 6H); 1.82 (m, 4H); 0.66 (m, 4H); 0.13-0.08 (m, 24H); $^{13}\text{C-NMR}$ (100 MHz, CDCl_3): δ 170.39, 157.32, 144.51, 122.76, 71.34, 23.73, 14.69, 1.76, 0.70.

4,4'-(((1,1,3,3,5,5,7,7-octamethyltetrasiloxane-1,7-diyl)bis(propane-3,1-diyl))bis(oxy))diphenol (3b)

1.33 g (1.99 mmol) of **2b** was dissolved in 40mL methanol, and 3mL of ammonium hydroxide (28%) in 10 mL water was added. The mixture was stirred under argon atmosphere overnight at room temperature, after which 30 mL of water and 60 mL of diethyl ether were added. The organic phase was separated, dried, and removed in vacuo to yield 1.08 g (1.71 mmol, 85%) **3b** as a viscous fluid. $^1\text{H-NMR}$ (400 MHz, CDCl_3): δ 6.94 (br s, 2H); 6.79 (m, 8H); 3.89 (t, 4H); 1.83 (m, 4H); 0.68 (m, 4H); 0.18-0.10 (m, 24H); $^{13}\text{C-NMR}$ (100 MHz, CDCl_3): δ 152.85, 149.62, 116.16, 115.76, 71.41, 23.24, 14.12, 1.23, 0.16.

(((1,1,3,3,5,5,7,7-octamethyltetrasiloxane-1,7-diyl)bis(propane-3,1-diyl))bis(oxy))bis(4,1-phenylene) bis(4-((6-(acryloyloxy)hexyl)oxy)benzoate) (RM-4Si)

522 mg (0.89 mmol) of **3b**, 525 mg (1.80 mmol) of 6OBA, 20 mg (0.16 mmol) 4-dimethylaminopyridine (DMAP), and 3 mg (0.01 mmol) butylated hydroxytoluene (BHT) were dissolved in dry DCM, brought under Ar atmosphere, and cooled in an ice bath. 370 mg (1.79 mmol) dicyclohexylcarbodiimide (DCC) was dissolved in dry DCM and slowly added to the reaction vessel and the reaction was left overnight. The solution was filtered, evaporated and purified through a silica column with hexane/ethyl acetate (50:50) as the eluent to yield 905 mg (0.80 mmol) **RM-4Si** as a clear paste. Yield: 89%. $^1\text{H-NMR}$ (400 MHz, CDCl_3): δ 8.13 (d, 4H); δ 7.08 (d, 4H);

δ 6.97 – 6.89 (m, 8H); δ 6.24 (d, 2H); δ 6.13 (m, 2H); δ 5.82 (d, 2H); δ 4.19 (t, 4H); δ 4.02 (t, 4H); δ 3.92 (t, 4H); δ 1.86 – 1.68 (m, 12H); δ 1.53 – 1.43 (m, 8H); δ 0.71 (m, 4H); 0.13-0.08 (m, 24H); $^{13}\text{C-NMR}$ (100 MHz, CDCl_3): δ 166.27, 165.27, 163.30, 156.74, 144.32, 132.20, 130.56, 128.54, 122.44, 121.76, 115.02, 114.20, 70.87, 68.02, 64.45, 28.98, 28.54, 25.72, 23.22, 14.18, 1.84, 1.30. MALDI-TOF MS (m/z): $[\text{M}+\text{Na}]^+$ calcd for $\text{C}_{58}\text{H}_{82}\text{O}_{15}\text{Si}_4$ 1153.46, found 1153.47.

5.6. References

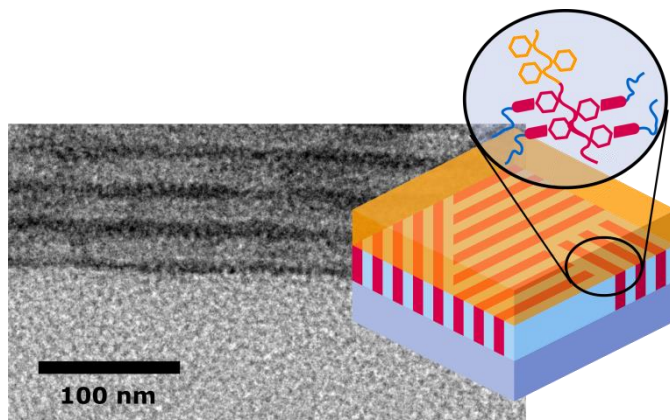
- [1] D. J. Broer, C. M. W. Bastiaansen, M. G. Debije, A. P. H. J. Schenning, *Angew. Chem.-Int. Ed.* **2012**, *51*, 7102.
- [2] J. P. F. Lagerwall, G. Scalia, *Curr. Appl. Phys.* **2012**, *12*, 1387.
- [3] T. Kato, N. Mizoshita, K. Kishimoto, *Angew. Chem. Int. Ed.* **2006**, *45*, 38.
- [4] C. L. van Oosten, C. W. M. Bastiaansen, D. J. Broer, *Nat. Mater.* **2009**, *8*, 677.
- [5] D. Liu, D. J. Broer, *Nat. Commun.* **2015**, *6*, 8334.
- [6] H. Shahsavan, S. M. Salili, A. Jákli, B. Zhao, *Adv. Mater.* **2015**, *27*, 6828.
- [7] X. D. Feng, M. E. Tousley, M. G. Cowan, B. R. Wiesenauer, S. Nejati, Y. Choo, R. D. Noble, M. Elimelech, D. L. Gin, C. O. Osuji, *ACS Nano* **2014**, *8*, 11977.
- [8] C. L. Gonzalez, C. W. M. Bastiaansen, J. Lub, J. Loos, K. Lu, H. J. Wondergem, D. J. Broer, *Adv. Mater.* **2008**, *20*, 1246.
- [9] H. P. C. van Kuringen, G. M. Eikelboom, I. K. Shishmanova, D. J. Broer, A. P. H. J. Schenning, *Adv. Funct. Mater.* **2014**, *24*, 5045.
- [10] S. J. Woltman, G. D. Jay, G. P. Crawford, *Nat. Mater.* **2007**, *6*, 929.
- [11] J. Lub, V. Recaj, L. Puig, P. Forcén, C. Luengo, *Liq. Cryst.* **2004**, *31*, 1627.
- [12] D. J. Broer, J. Boven, G. N. Mol, G. Challa, *Makromol. Chem.* **1989**, *190*, 2255.
- [13] J. Lub, D. Broer, in *Cross-Linked Liq. Cryst. Syst.*, CRC Press, **2011**, pp. 3–47.
- [14] I. Dierking, *Adv. Mater.* **2000**, *12*, 167.
- [15] For silsesquioxane based hybrid liquid crystals and functional materials, see: G. H. Mehl, I. M. Saez, *Appl. Organomet. Chem.* **1999**, *13*, 261; Q. Ye, H. Zhou, J. Xu, *Chem. – Asian J.* **2016**, *11*, 1322; X. Wang, C. M. Cho, W. Y. Say, A. Y. X. Tan, C. He, H. S. O. Chan, J. Xu, *J. Mater. Chem.* **2011**, *21*, 5248.
- [16] C. Pugh, J. Y. Bae, J. Dharia, J. J. Ge, S. Z. D. Cheng, *Macromolecules* **1998**, *31*, 5188.
- [17] I. Dierking, L. Komitov, S. T. Lagerwall, T. Wittig, R. Zentel, *Liq. Cryst.* **1999**, *26*, 1511.
- [18] S. Westphal, S. Diele, A. Mädicke, F. Kuschel, U. Scheim, K. Rühlmann, B. Hisgen, H. Ringsdorf, *Makromol. Chem. Rapid Commun.* **1988**, *9*, 489.
- [19] A. Noro, M. Hayashi, A. Ohshika, Y. Matsushita, *Soft Matter* **2011**, *7*, 1667.
- [20] K. Nickmans, J. N. Murphy, B. de Waal, P. Leclère, J. Doise, R. Gronheid, D. J. Broer, A. P. H. J. Schenning, *Adv. Mater.* **2016**, *28*, 10068.

- [21] R. Achten, A. Koudijs, M. Giesbers, A. Marcelis, E. Sudholter, *Mol. Cryst. Liq. Cryst.* **2007**, *477*, 169.
- [22] M. Funahashi, *Mater. Chem. Front.* **2017**, *1*, 1137
- [23] M. Funahashi, A. Sonoda, *J. Mater. Chem.* **2012**, *22*, 25190.
- [24] C. A. Ross, Y. S. Jung, V. P. Chuang, F. Ilievski, J. K. W. Yang, I. Bitá, E. L. Thomas, H. I. Smith, K. K. Berggren, G. J. Vancso, J. Y. Cheng, *J. Vac. Sci. Technol. B Microelectron. Nanometer Struct.* **2008**, *26*, 2489.
- [25] S. J. Clarson, J. E. Mark, in *Polym. Sci. Technol.* (Eds.: S.J. Clarson, J.A. Semlyen), Prentice Hall PTR, Englewood Cliffs, NJ, **1993**, pp. 616–648.
- [26] M. Wang, L.-X. Guo, B.-P. Lin, X.-Q. Zhang, Y. Sun, H. Yang, *Liq. Cryst.* **2016**, *0*, 1.
- [27] S. Guo, K. Matsukawa, T. Miyata, T. Okubo, K. Kuroda, A. Shimojima, *J. Am. Chem. Soc.* **2015**, *137*, 15434.
- [28] A. Sanchez-Ferrer, A. Merekalov, H. Finkelmann, *Macromol Rapid Comm* **2011**, *32*, 671.
- [29] H. Finkelmann, H.-J. Kock, G. Rehage, *Makromol. Chem. Rapid Commun.* **1981**, *2*, 317.
- [30] D. J. Gardiner, H. J. Coles, *J. Appl. Phys.* **2006**, *100*, 124903.
- [31] L. Li, C. D. Jones, J. Magolan, R. P. Lemieux, *J. Mater. Chem.* **2007**, *17*, 2313.
- [32] W. K. Robinson, P. S. Kloess, C. Carboni, H. J. Coles, *Liq. Cryst.* **1997**, *23*, 309.
- [33] E. Corsellis, D. Guillon, P. Kloess, H. Coles, *Liq. Cryst.* **1997**, *23*, 235.
- [34] T. J. Zhang, D. M. Sun, X. K. Ren, L. L. Liu, G. Y. Wen, Z. J. Ren, H. H. Li, S. K. Yan, *Soft Matter* **2013**, *9*, 10739.
- [35] M. García-Iglesias, B. F. M. de Waal, I. de Feijter, A. R. A. Palmans, E. W. Meijer, *Chem. Eur. J.* **2015**, *21*, 377.
- [36] A. Zelcer, B. Donnio, C. Bourgoigne, F. D. Cukiernik, D. Guillon, *Chem. Mater.* **2007**, *19*, 1992.
- [37] C. Keith, R. A. Reddy, U. Baumeister, C. Tschierske, *J. Am. Chem. Soc.* **2004**, *126*, 14312.
- [38] R. Murashige, Y. Hayashi, S. Ohmori, A. Torii, Y. Aizu, Y. Muto, Y. Murai, Y. Oda, M. Hashimoto, *Tetrahedron* **2011**, *67*, 641.
- [39] M. Portugall, H. Ringsdorf, R. Zentel, *Makromol. Chem.* **1982**, *183*, 2311.
- [40] M. Ibn-Elhaj, A. Skoulios, D. Guillon, J. Newton, P. Hodge, H. Coles, *J. Phys. II* **1996**, *6*, 271.
- [41] N. Olsson, B. Helgee, G. Andersson, L. Komitov, *Liq. Cryst.* **2005**, *32*, 1139.
- [42] N. Olsson, M. Schröder, S. Diele, G. Andersson, I. Dahl, B. Helgee, L. Komitov, *J. Mater. Chem.* **2007**, *17*, 2517.
- [43] S. Wu, *Polymer Handbook*, Wiley-Interscience, New York, New York, **1989**.
- [44] B. M. I. van der Zande, J. Steenbakkers, J. Lub, *J. Appl. Phys.* **2005**, *97*, 123519.

Chapter 6

Vertically aligned, hybrid organic/inorganic sub-5 nm structured thin films by hydrogen bonded oligo(dimethylsiloxane) liquid crystals and polymers

Abstract. This chapter describes the synthesis and characterization of a novel class of hydrogen-bonding oligo(dimethylsiloxane)-based thermotropic liquid crystals (LCs). Polymeric supramolecular assemblies were obtained when combined with poly(4-vinylpyridine) homopolymer or poly(styrene)-b-poly(4-vinylpyridine) block copolymer (BCP). By adjusting the molar fraction of the LCs, glassy smectic and columnar hexagonal morphologies were obtained with sub-5 nm features. The hierarchical self-assembly afforded by LC/BCP complexes further resulted in the vertical orientation of LC features in thin films.



6.1. Introduction

As discussed in chapter 1, small molecules are an emerging class of nanomaterials for applications at the sub-5 nm scale, including organic electronics,^[1-5] nanoporous membranes,^[6-9] and ultra-fine nanolithographic resists.^[10,11] Unlike traditional block copolymers (BCPs), the self-assembly of small molecules is not limited by an order-disorder transition at low molecular weight, allowing the formation of sub-5 nm features.^[11-13] Hybrid organic/inorganic small molecules consisting of polyhedral oligomeric silsesquioxane (POSS)^[14,15] or oligo(dimethylsiloxane) (ODMS)^[11,12] are highly advantageous, since their chemical immiscibility leads to phase separation into highly ordered nanostructures, and a high etch contrast between molecular components. In principle, these materials could be used to fabricate inorganic nanostructure arrays with sub-5 nm features by etching. However, there are still major challenges concerning this novel class of materials; including control over the self-assembled nanostructured morphology, the formation of defect-free patterns in thin films with a predetermined orientation, and their conversion into functional materials and devices.

In previous chapters, we reported a series of ODMS liquid crystals (LCs) which form columnar (chapter 2) and lamellar (chapter 3) morphologies with sub-5 nm dimensions. The high mobility of LC phases makes these materials amenable to directed self-assembly processes for the formation of large-area ordered structures,^[8,11,16,17] such as graphoepitaxy (chapter 2), and photoalignment (chapter 5). However, obtaining vertically oriented features remains challenging given the low surface energy of ODMS ($\gamma_{\text{PDMS}} \sim 20.4 \text{ mN m}^{-1}$).^[18] Moreover, the low glass transition temperature associated with these materials ($T_{\text{g, PDMS}} \sim -127 \text{ }^\circ\text{C}$)^[19] leads to the deformation of the patterns during processing,^[20] and the ‘freezing-in’ of metastable structures is hindered (chapter 5). To address these challenges, it would be desirable to combine the sub-5 nm feature sizes of hybrid organic/inorganic small molecules with the properties and processing of glassy polymeric materials.

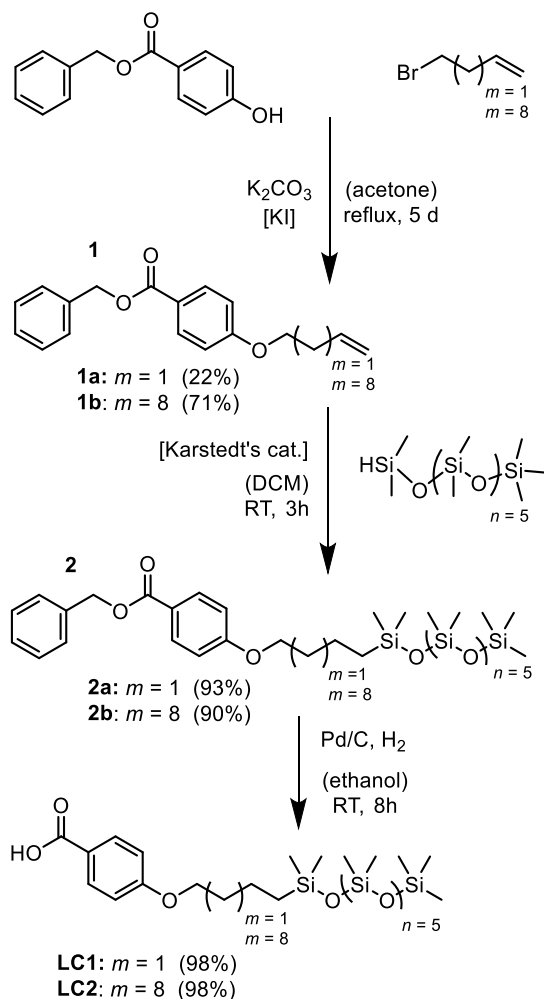
Polymeric supramolecular assemblies (PSA) have been constructed through the linking of small molecules to polymer side chains *via* noncovalent interactions such as hydrogen bonding, electrostatic interactions, or metal ligation.^[21-29] The main advantage of PSAs is that they enable morphological control through a modular mixing approach,^[30-32] as opposed to cumbersome organic synthesis. Extensive studies have been carried out on PSA systems consisting of *n*-alkylphenols in combination with poly(4-vinylpyrine) (P4VP)^[33,34] or poly(styrene)-*b*-poly(4-vinylpyrine) (PS-*b*-P4VP).^[31,35,36] Early work by the group of Ikkala^[24,25,31] showed that

pentadecylphenol (PDP) can form a smectic (Sm) LC phase in the microdomains of PS-*b*-P4VP. A key aspect of the hierarchical self-assembly is that the BCP features are oriented perpendicular to those formed by PDP on a smaller length scale.^[31] Moreover, PDP could be removed by washing with selective solvent, providing nanoscopic channels in the major component matrix.^[37] Since this pioneering work, other small molecules have been combined with P4VP to form PSA materials with more complex morphologies,^[38,39] or to embed specific functionalities.^[35] For example, perfluorocarbons,^[40] oligo(thiophenes),^[41] and azobenzenes^[42–45] have been incorporated. With the large range of materials that has been explored, hybrid organic/inorganic PSAs have not been reported. Moreover, while most studies have reported only bulk phase behaviour, the phenomenon of hierarchical self-assembly provides opportunities for controlling the thin film orientation of features.^[46]

In this chapter, we report glassy ODMS-based PSAs which are obtained by the hydrogen bonding of ODMS LCs with P4VP and PS-*b*-P4VP. First, the synthesis and characterization of the novel ODMS LC is discussed, followed by the hierarchical self-assembly behaviour. By adjusting the molar fraction of the LCs within the PSA, smectic and columnar hexagonal morphologies were obtained with sub-5 nm features. Finally, the ultra-fine features were oriented vertically in thin films by using the hierarchical self-assembly approach.

6.2. Results & Discussion

The synthetic scheme for the preparation of hydrogen bonding ODMS liquid crystals (**LC1**, **LC2**) is shown in Scheme 1. Benzyl paraben was reacted with different alkyl bromides in a Williamson ether synthesis to form intermediate **1**. The alkyl spacer length was varied by using 4-bromobut-1-ene (**1a**, $m=1$) and 11-bromoundec-1-ene (**1b**, $m=8$). Heptasiloxane monohydride was received from the group of Meijer,^[47] and coupled to **1** using Karstedt's catalyst to yield intermediate **2**. Finally, intermediate **2** was deprotected using catalytic hydrogenation with palladium on carbon to produce **LC1** ($m=1$) and **LC2** ($m=8$). The full synthetic procedures and characterization are provided in the experimental section.



Scheme 1. Synthetic scheme for the preparation of hydrogen bonding ODMS liquid crystals, where m represents the length of the alkyl spacer. **LC1** ($m = 1$), **LC2** ($m = 8$). The yields are indicated in brackets.

The phase behaviour of compound **LC1** and **LC2** was investigated by temperature dependent polarized optical microscopy (POM) and differential scanning calorimetry (DSC). Figure 1a shows the DSC data obtained on second cooling of the compounds ($10\text{ }^{\circ}\text{C}/\text{min}$). **LC1** shows a phase transition at $14\text{ }^{\circ}\text{C}$, with an associated enthalpy of 4.3 J g^{-1} . **LC2** shows a phase transition at $49\text{ }^{\circ}\text{C}$, with an associated enthalpy of 0.4 J g^{-1} , and an additional phase transition at $1\text{ }^{\circ}\text{C}$, with an associated enthalpy of 9.8 J g^{-1} . POM images obtained just under the isotropization temperature show birefringent multidomains which are typical for liquid crystals

(Figure 1b). Only **LC2** was found to crystallize within the measured range (at 1°C). We conclude that the longer alkyl spacer in **LC2** is responsible for the crystallization at lower temperatures and the higher isotropization temperature.

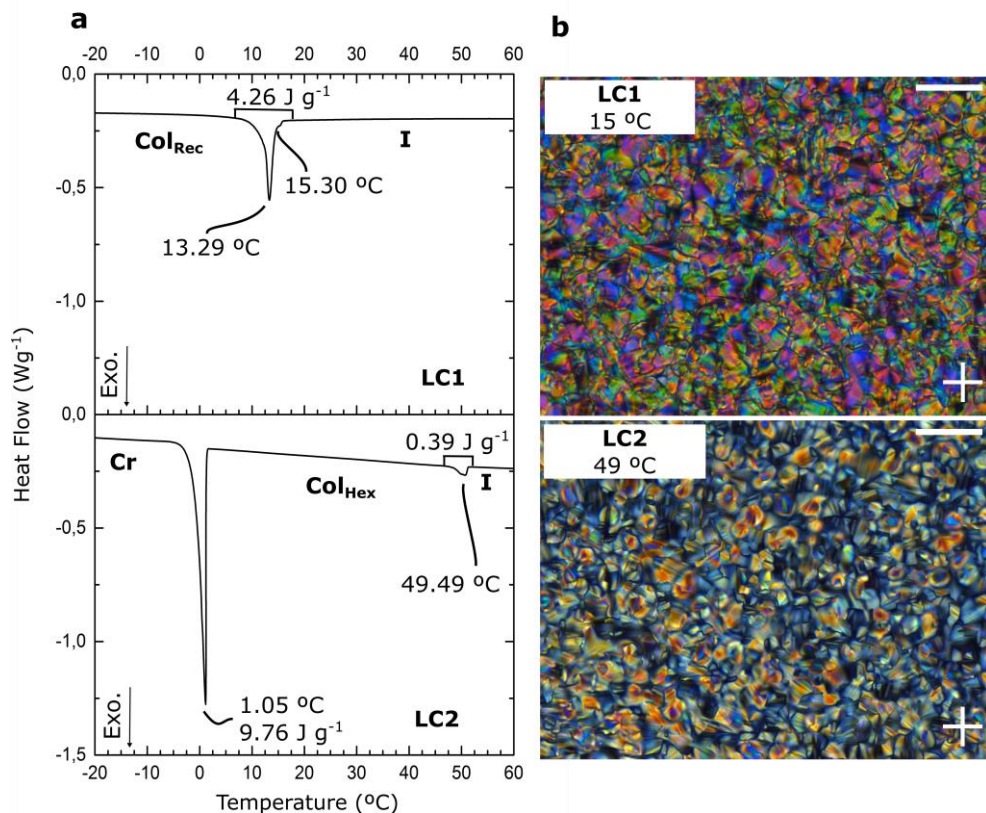


Figure 1. DSC thermographs and POM images of the hydrogen bonding ODMS liquid crystals. The POM images were obtained under crossed polarizers just under the isotropization temperature (polarizer axes are indicated in the images with a cross). All scale bars: 50 μm

The LC phases of **LC1** and **LC2** were further investigated by temperature dependent bulk x-ray diffraction (XRD) in both wide-angle and medium-angle configurations (Figure 2). For each compound, two broad peaks were observed in the wide-angle region ($6 \text{ nm}^{-1} < q > 20 \text{ nm}^{-1}$), signifying nano-phase separation between the ODMS ($q = 9 \text{ nm}^{-1}$, $d = 0.70 \text{ nm}$) and organic ($q = 13.4 \text{ nm}^{-1}$, $d = 0.45 \text{ nm}$) molecular components. The medium angle reflections ($1 \text{ nm}^{-1} < q > 6 \text{ nm}^{-1}$) were used to assign the LC lattice parameters indicated in Figure 2. **LC1** forms a rectangular columnar phase (Col_{Rec}) (plane group $c2nm$). At 10 °C, the lattice constants are: $a = 6.32 \text{ nm}$, $b = 3.43 \text{ nm}$. **LC2** forms a hexagonal columnar phase

(Col_{Hex}) (plane group p6mm). At room temperature, the lattice constant is: $a = 4.69$ nm. The formation of a lower-order Col_{Hex} phase in **LC2** is likely a consequence of the increased coil-to-rod volume fraction.^[48]

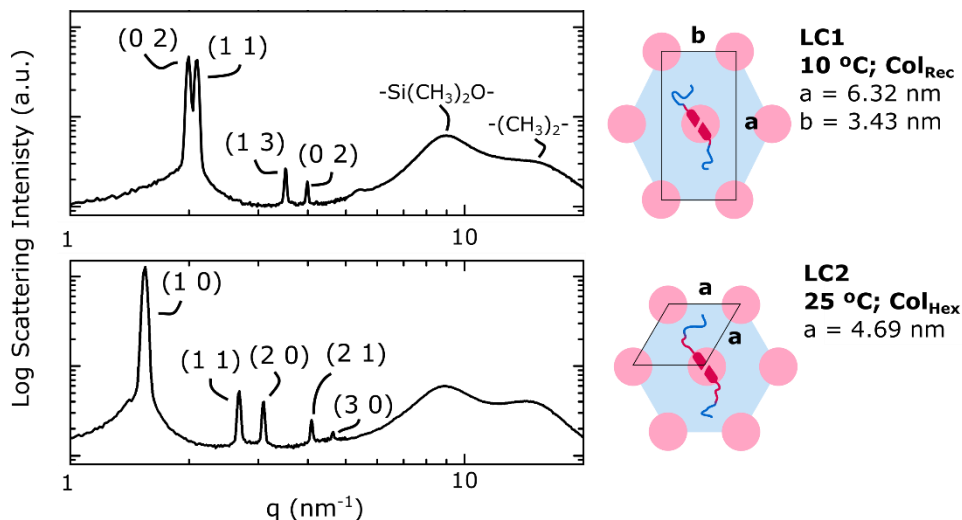


Figure 2. Bulk x-ray diffraction data of the hydrogen bonding ODMS liquid crystals. The XRD spectra were collected in both wide- and medium-angle configurations. The assigned Miller indices and the respective intermolecular scatterings are indicated, as well as the corresponding lattices.

LC2 was selected for subsequent mixing experiments with poly(4-vinyl pyridine) (P4VP) and poly(styrene)-*b*-poly(4-vinylpyridine) (PS-*b*-P4VP) given its accessible LC temperature range and LC behavior at room temperature. To prepare polymeric supramolecular assemblies, **LC2** was first mixed with **P4VP**_{15k} (PDI=1.25) in various molar ratios x of LC2:P4VP ($0 \leq x < = 1$). Figure 3 shows the example of a fully complexed case ($x = 1$) in which LC2 is hydrogen bonded with the pyridine moieties of P4VP.

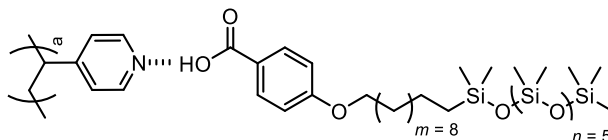


Figure 3. Chemical structures of the polymer supramolecular assembly of **LC2** and **P4VP**. The carboxylic group on **LC2** associates with the pyridine group on **P4VP** via hydrogen bonding.

To investigate the hydrogen bond formation, **LC2**, **P4VP**, and supramolecular assemblies **P4VP(LC2)_x** were characterised with Fourier transform infrared spectroscopy (FTIR). Figure 4 shows the 1700 cm^{-1} and 1400 cm^{-1} regions of the FTIR spectra. **LC2** exhibits a carbonyl stretch vibration at 1682 cm^{-1} which is characteristic for the formation of hydrogen bonded benzoic acid dimers.^[49,50] In the supramolecular assemblies **P4VP(LC2)_x**, the band shifts to 1695 cm^{-1} , because the C=O groups are not involved anymore in hydrogen bonding (Figure 3).^[33,51] The characteristic band at 1414 cm^{-1} corresponds to the stretching mode of the free pyridine ring on pristine **P4VP**. The vibrational mode is perturbed due to the formation of hydrogen bonds, causing a decreased absorption intensity and a shift to 1418 cm^{-1} .^[49] Therefore, as the degree of polymer supramolecular assembly is increased, the intensity of the shifted peak at 1418 cm^{-1} increases, while the intensity of the original peak at 1414 cm^{-1} decreases.

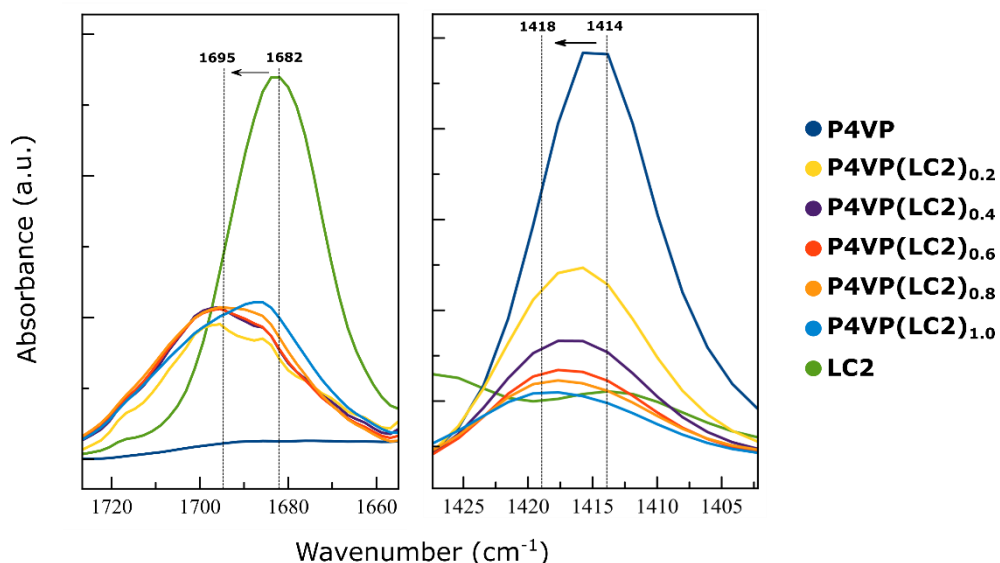


Figure 4. FTIR spectra of **LC2**, **P4VP**, and **PV4P(LC2)_x** samples.

The areas under the peaks and the peak positions were estimated by deconvolution of the FTIR data using Voigt-type functions. The fraction of hydrogen-bonded 4-vinylpyridines (f_{HB}) was estimated using the formula:^[50]

$$f_{HB} = \frac{A_{1418}}{A_{1418} + \frac{\alpha_{1414}}{\alpha_{1418}} A_{1414}} \quad [1]$$

where A and α are the peak areas and absorption coefficients, respectively. As shown by Lee *et. al.*, the absorption cross sections of free and hydrogen bonded P4VP bands do not change upon hydrogen bonding,^[50] such that $\alpha_{1414}/\alpha_{1418} \approx 1$, allowing f_{HB} to be calculated. Figure 5 shows f_{HB} in function of molar ratio x , obtained using equation 1. For $x \leq 0.8$, a linear 1:1 regime is observed. At $x = 1.0$, deviation from the linear behaviour is observed, indicating a maximal complexation between **LC2** molecules and the pyridine moieties. Comparable results were obtained by analyzing the absorption bands at 1682 and 1695 cm^{-1} . The inability to attain a 1:1 stoichiometry deviates from behaviour seen in n-alkylphenols,^[34] and is likely due to dimerization of **LC2**.^[33]

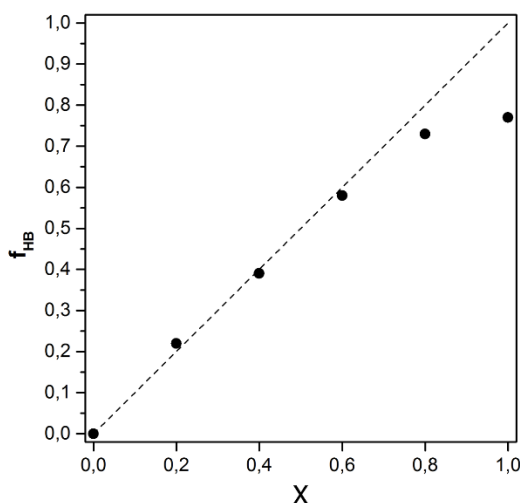


Figure 5. Fraction of hydrogen-bonded pyridines (f_{HB}) as a function of molar ratio x (LC2:P4VP) for the **P4VP(LC2)_x** supramolecular assemblies.

POM images of blends in the $x \leq 0.8$ regime show grainy birefringent textures, consistent with formation of homogenous blends of **PVP** and **LC2** with LC behaviour (Figure 6). DSC measurements show that the polymer supramolecular assemblies are glassy at room temperature. For neat P4VP, $T_g \sim 150$ °C, in agreement with literature.^[19] For $0.2 \leq x \leq 0.8$, T_g is reduced to ~ 75 °C. None of the

supramolecular assemblies are found to crystallize. For $x = 0.4, 0.6, 0.8$, an isotropization temperature is observed which decreases with increasing x .

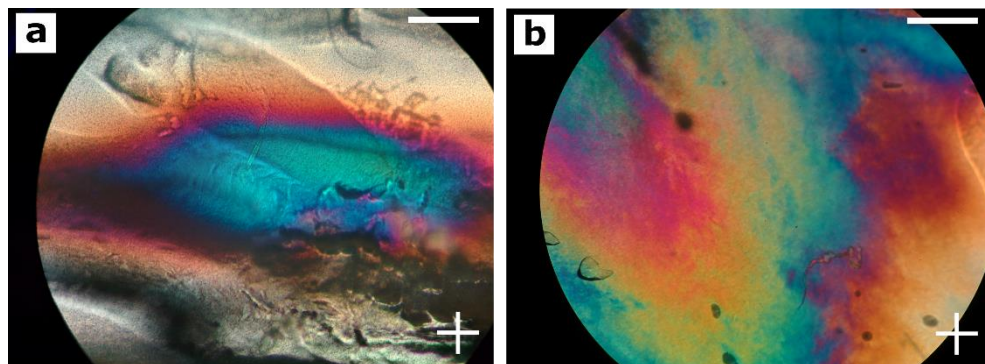


Figure 6. POM images of the P4VP(LC2)_x supramolecular assemblies. a) $x = 0.4$. b) $x = 0.6$. The POM images were obtained under crossed polarizers just below the isotropization temperature (polarizer axes are indicated in the images with a cross). All scale bars: 500 μm

The room temperature PSAs were further investigated using XRD (Figure 7). To promote the formation of long range order, the materials were annealed at 85 °C for approximately 1h. Figure 7 shows the medium angle scattering data ($1 \text{ nm}^{-1} < q > 5 \text{ nm}^{-1}$) alongside the assigned miller indices and LC lattice parameters. As indicated by the 1:2 peak ratio, a Sm phase is formed at $x = 0.4$ ($a = 6.21 \text{ nm}$). At higher x , Col_{Hex} phases are observed by the $1:\sqrt{3}$ peak ratios. The Sm to Col_{Hex} transition can be understood by volumetric arguments,^[30] and suggests that the vinyl(pyridines) are at the center of the supramolecular cylinders. As can be seen in Figure 7, the lattice parameter of the Col_{Hex} phase is dependent on x , and changes from 6.51 nm ($x = 0.6$) to 6.43 nm ($x = 0.8$), and 6.41 nm ($x = 1.0$). At the maximum loading ($x = 1.0$), macrophase separation is observed by the presence of an additional scattering peak at $q = 1.5 \text{ nm}^{-1}$, which corresponds to the primary scattering vector of pure **LC2** (indicated by the grey shadow in Figure 7). The observation of macrophase separation is in agreement with FTIR, DSC, and POM. Together, the scattering data reveals that the morphology and lattice spacing can be tuned by adjusting the molar ratio x .

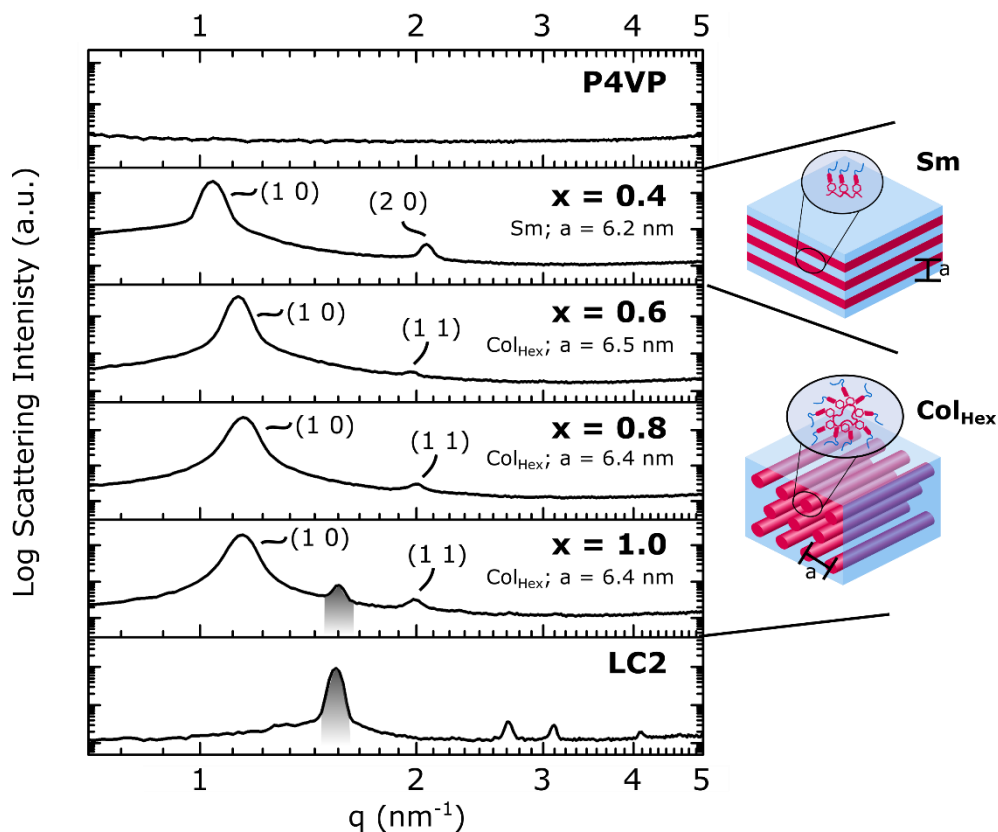


Figure 7. Bulk x-ray diffraction data of the P4VP(LC2)_x supramolecular assemblies. The XRD spectra were collected in the medium-angle configuration. The assigned Miller indices and the respective intermolecular scatterings are indicated, as well as the corresponding lattices. The primary scattering peak of **LC2** is indicated by a grey shadow.

Next, a $\text{PS}_{33k}\text{-b-P4VP}_{8k}$ ($f_{\text{PS}} \sim 0.8$) (PDI=1.06) block copolymer was selected for the preparation of hierarchical PSAs. This BCP hydrogen bonds selectively with **LC2** via the PVP blocks (Figure 8). Neat $\text{PS}_{33k}\text{-b-P4VP}_{8k}$ exhibits a hexagonal (HEX) morphology in bulk (P4VP minority phase), but is expected to form a lamellar (LAM) morphology upon addition of **LC2**, by the increase of volume fraction of the combined P4VP(LC2)_x block.^[36] Hierarchical PSAs were prepared with molar ratios $x = 0.3$, $x = 0.4$, and $x = 0.5$. With FT-IR, comparable hydrogen-bonding behaviour was observed as for the PVP PSAs. Using DSC, comparable thermal transitions were observed, with the exception of an additional glass transition at 120 °C, which corresponds to the **PS** domains.^[19] The presence of distinct glass transition temperatures for **PS** (120 °C) and P4VP(LC2)_x (75 °C) already indicates the immiscibility of the blocks.

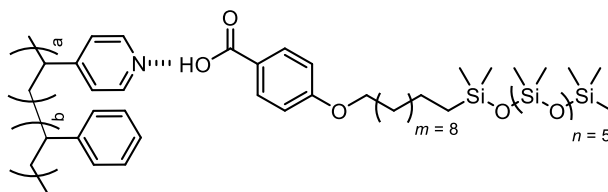


Figure 8. Chemical structures of polymeric supramolecular assembly of **PS-b-P4VP** and **LC2**. The carboxylic group on **LC2** associates selectively with the pyridine group on **P4VP** via hydrogen bonding.

The **PS-b-P4VP(LC2)_x** materials were investigated by bulk XRD. To capture the hierarchical multi-scale self-assembly, scattering data was obtained in small-angle and medium-angle configurations. Figure 9 shows the combined data (concatenated at $q = 0.7 \text{ nm}^{-1}$) together with the assigned lattice constants and miller indices. For $x = 0.3$, a smectic-in-lamellar (Sm-in-LAM) phase is observed ($d = 37.0 \text{ nm}$, $a = 5.81 \text{ nm}$). For $x = 0.5$, a (Col_{Hex}-in-LAM) phase is observed ($d = 40.6 \text{ nm}$, $a = 6.3 \text{ nm}$) and at the intermediate molar ratio ($x = 0.4$) a combination of medium angle scatterings are observed in addition to the LAM morphology of the BCP, indicating the co-existence of Sm and Col_{Hex} morphologies (mixed-in-LAM). Overall, the lamellar spacing increases slightly with increasing x , likely due to the increase in combined molecular weight ($d \propto N^{2/3}$). The transition from Sm to Col_{Hex} morphologies agrees with the behaviour observed in the homopolymer system, and similar lattice spacings are observed. 2D XRD plots of shear-aligned samples further indicate the orthogonal nature of the hierarchical self-assembly. Figure 10 shows an example 2D plot for **PS-P4VP(LC2)_{0.3}** in which the BCP and LC scattering peaks are perpendicular to each other, thereby validating the schematic representation of the lattices shown in Figure 9.

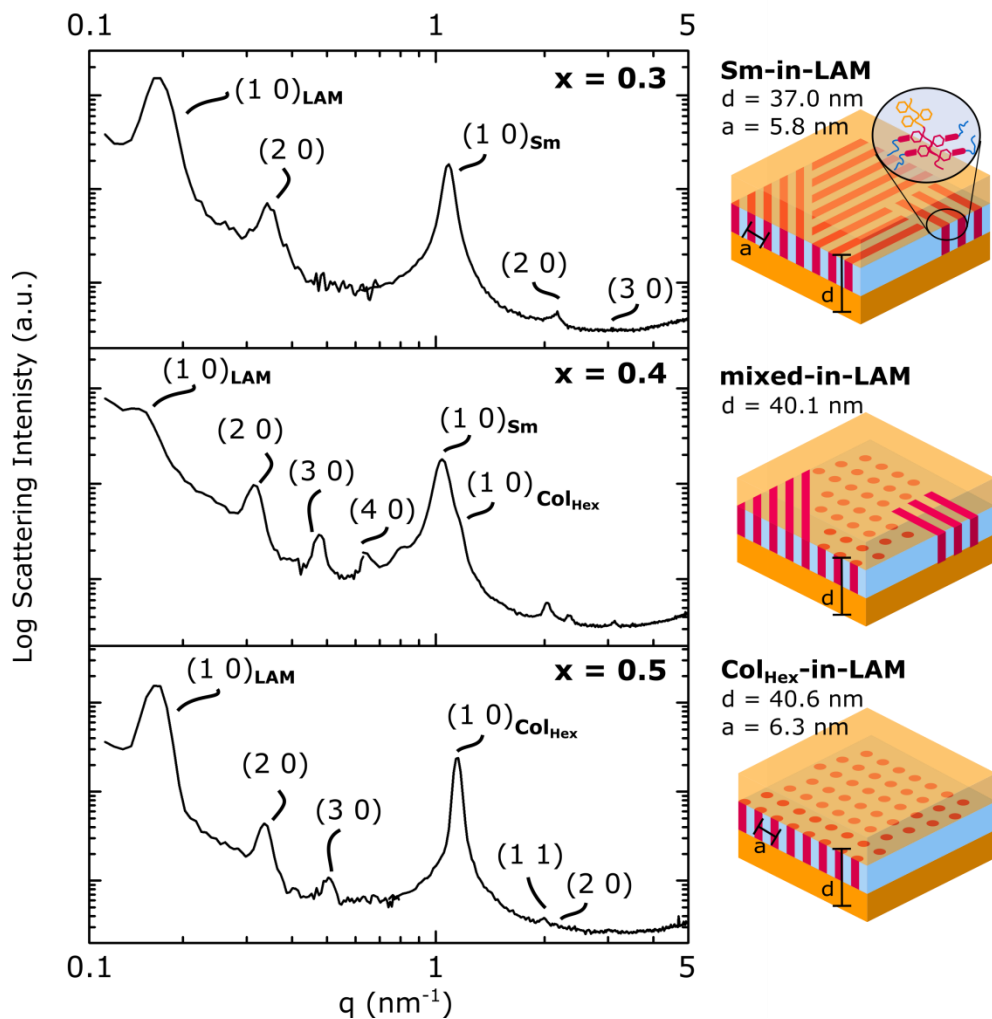


Figure 9. Bulk x-ray diffraction data of the PS-P4VP(LC2)_x polymeric supramolecular assemblies. The XRD spectra were collected in the small-angle and medium-angle configuration, and concatenated at $q = 0.7$ nm⁻¹. The assigned Miller indices and the respective intermolecular scatterings are indicated, as well as the corresponding lattices.

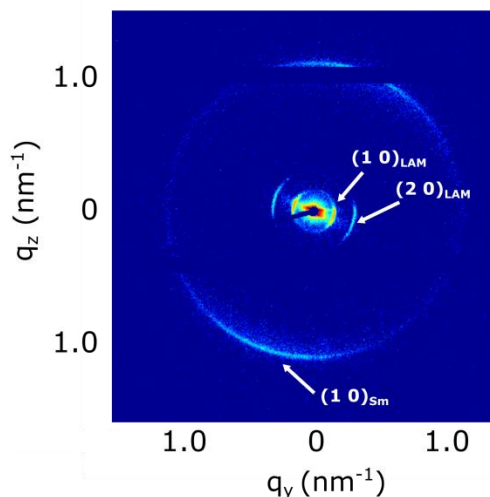


Figure 10. Small-angle XRD data of **PS-P4VP(LC2)_{0.3}** complex. The assigned miller indices are indicated in the figure.

To further investigate the hierarchical nature of the self-assembly, transmission electron microscopy (TEM) was performed on a **PS_{33k}-b-P4VP_{4k}(LC2)_{0.5}** thin film (Figure 11). To this end, thick films were prepared by dropcasting on an epoxy substrate, and solvo-thermal annealed with chloroform to promote ordering. Large area TEM images of different unstained polymer sections (Figure 11a-b) reveal the presence of alternating layered structures with high lateral order across the image. Within the layers, smaller features are contained. Analysis of a zoomed in image (Figure 11c) reveals that the layered structures have a periodicity of ca. 35 nm, corresponding to the BCP lattice spacing. Perpendicular to these lamellae, features with a periodicity of ca. 6 nm are observed, corresponding the LC phase of the **P4VP(LC2)_{0.5}** component. Interestingly the morphology at the interface between the PSA and the epoxy substrate (Figure 11d) shows that the PSA is directed at the substrate interface. The BCP lamellae are oriented parallel to the epoxy substrate, and by extension, the LC features are oriented in a perpendicular fashion. Moreover, the interface layer appears to consist of an LC layer.

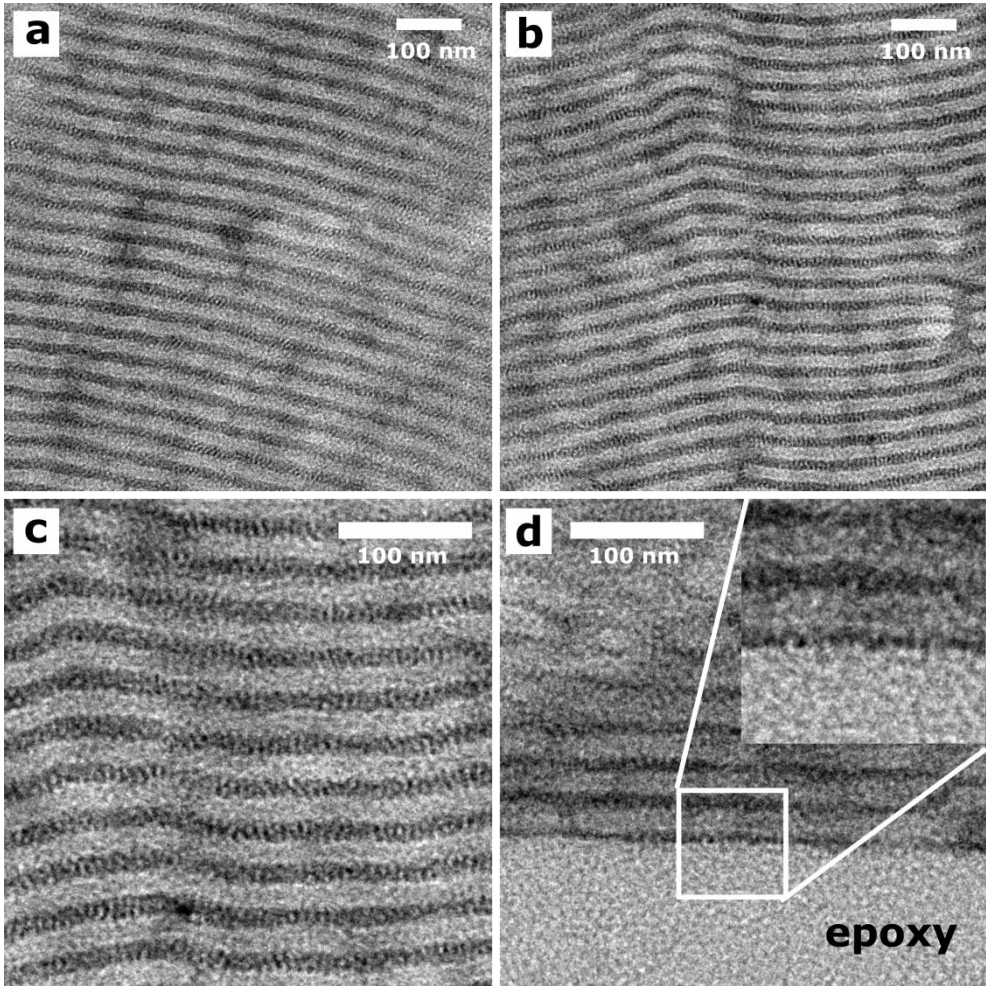


Figure 11. a-c) Transmission electron micrographs of $\text{PS}_{33\text{k}}\text{-b-P4VP}_{4\text{k}}(\text{LC2})_{0.5}$ on an epoxy substrate. PS lamellae are light; ODMS side chains are dark. d) TEM image of the PSA at the epoxy interface (inset = 4x magnification).

For nanofabrication purposes, thin PSA films are desired. In order to prepare such films, dilute solutions of PSAs were prepared using $\text{P4VP}_{15\text{k}}$ and $\text{PS}_{33\text{k}}\text{-b-P4VP}_{8\text{k}}$ in combination with **LC2** and spin-coated on Si wafers bearing an antireflective coating. Solutions of 2 wt % in chloroform resulted in ca. 80 nm thin films, according to ellipsometry. To promote lateral ordering of the features, the samples were thermally annealed at 85 °C for 1h. The annealing temperature was chosen to be above the glass transition temperature of $\text{P4VP}(\text{LC2})_x$ (75 °C), but under the glass transition temperature of **PS** (120 °C).

To investigate the through-film morphology of the annealed films, small-angle grazing-incidence x-ray diffraction (GIXRD) was performed (Figure 12). Figure 12a shows that the scattering data for **P4VP(LC2)_{0.4}** can be fitted assuming a smectic phase ($a = 5.8$ nm), which is in line with bulk observations. For **P4VP(LC2)_{0.4}**, the scattering peaks are perpendicular to the substrate, indicating that the smectic layers are oriented parallel to the surface. Since the surface energy of the ODMS tails is presumed to be very low ($\gamma_{\text{PDMS}} = 20.5$ mN/m),^[23] the siloxane tails are anticipated to wet the air interface, driving the parallel orientation. In contrast, for **PS-P4VP(LC2)_{0.3}**, (Figure 12b) the scattering peaks are oriented parallel to the substrate, indicating that the smectic features are oriented normal to the surface. The absence of diffraction rods originating from the BCP lamellae, indicate indirectly that they are oriented planar to the surface.^[46] For the LC cylinders in the Col_{Hex} phase PSAs, similar observations are made (Figure 12c-d). For **P4VP(LC2)_{0.6}** (Figure 12c) the scattering data is fitted with a Col_{Hex} phase ($a = 6.8$ nm) in which the cylinders are oriented planar to the substrate. For **PS-P4VP(LC2)_{0.5}** (Figure 12c), the primary scattering peak is oriented normal to the surface. Together, these findings indicate that the presence of the **PS** block causes the vertical alignment for both Sm and Col_{Hex} LC features.

The surfaces of the thin films were further characterized with atomic force microscopy (AFM). Figure 13a shows the AFM height map for **P4VP(LC2)_{0.4}** which shows the presence of plateaus. According to the cross-section (shown by the black line, and plotted in the inset), the height of the plateaus are *ca.* 6 nm, which corresponds to the smectic layer spacing expected for this material. This finding indicates the presence of smectic layers which are oriented parallel to the surface, in agreement with GIXRD observations (Figure 12a). In contrast, for **PS-P4VP(LC2)_{0.3}**, (Figure 13b) plateaus are observed with a height of *ca.* 37 nm, corresponding to the BCP layer spacing. This finding implies the parallel orientation of BCP features, and by extension, the vertical alignment of LC features inside the film, corresponding to the GIXRD findings (Figure 12b). Together, the GIXRD and AFM data unequivocally demonstrate that the vertical alignment of sub-5 nm smectic features.

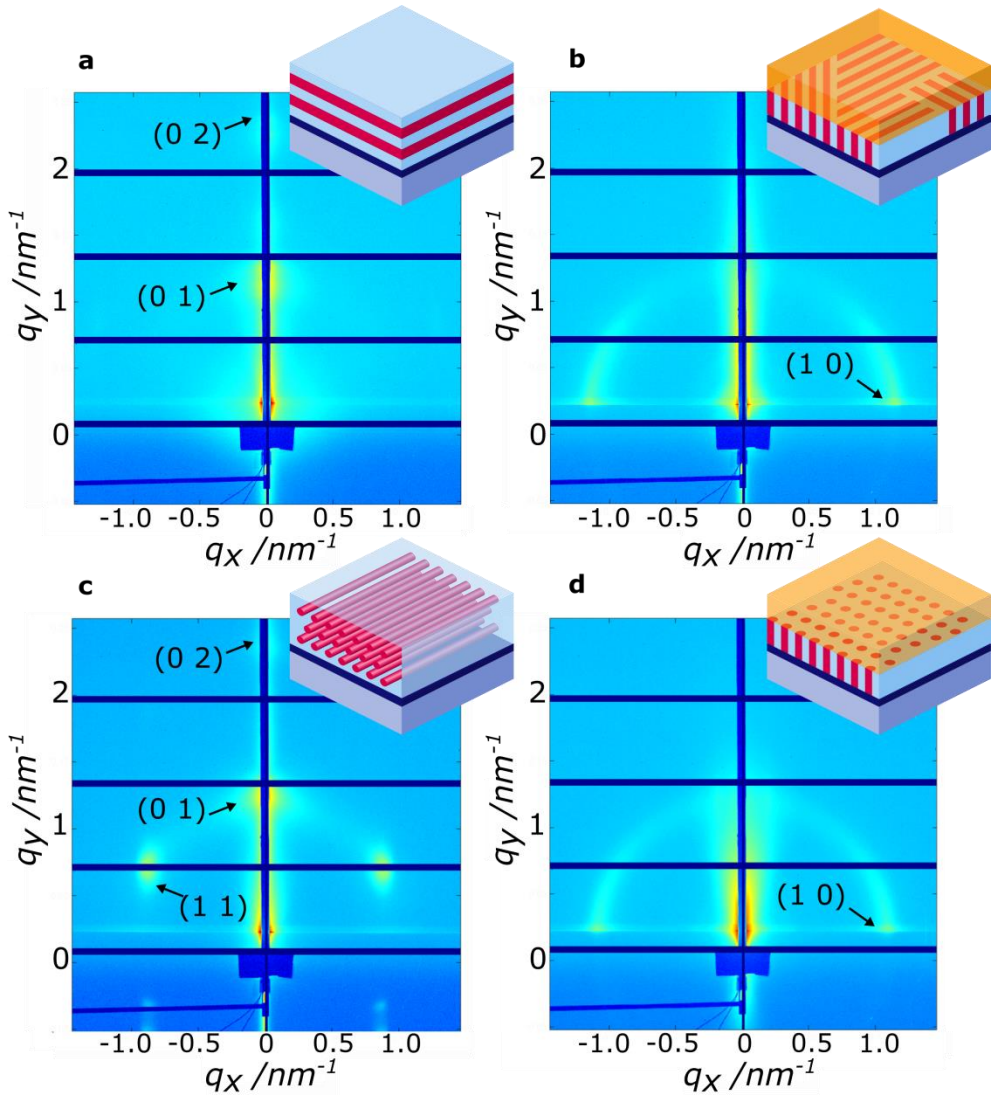


Figure 12. Grazing-incidence x-ray diffraction data in small-angle configuration for PSA thin films of thickness ~ 80 nm, measured around the critical angle. a) P4VP(LC) $_{0.4}$ (Sm), b) PS-P4VP(LC) $_{0.4}$ (Sm-in-LAM), c) P4VP(LC) $_{0.6}$ (Col $_{\text{Hex}}$), d) PS-P4VP(LC) $_{0.5}$ (Col $_{\text{Hex}}$ -in-LAM). Schematic representations of the thin film structure from combined GIXRD and AFM observations are shown in the inset.

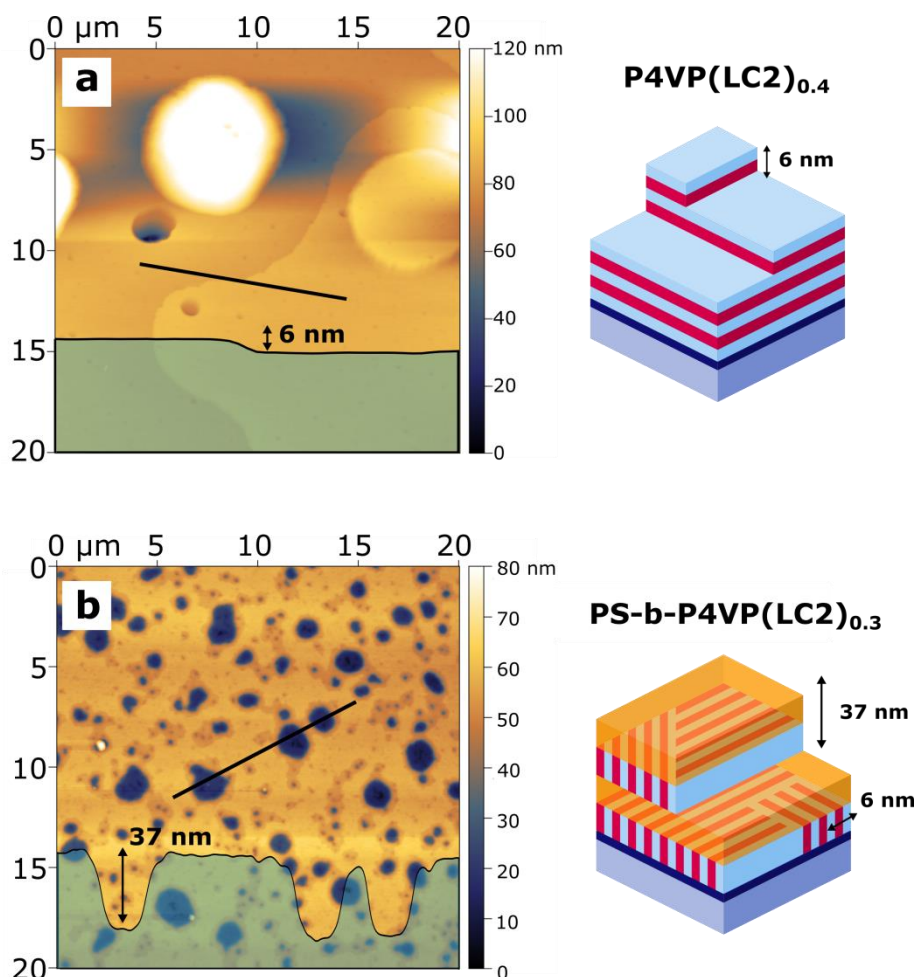


Figure 13. Atomic force microscopy height images of annealed PSA thin films of thickness ~ 80 nm. a) $\text{P4VP(LC2)}_{0.4}$ (Sm), b) $\text{PS-P4VP(LC2)}_{0.3}$ (Sm-in-LAM). Cross-sections are indicated by the line and are shown in the inset.

6.3. Conclusion

In this chapter, novel hydrogen bonding ODMS LCs were prepared, characterized, and their thermotropic phase behavior was investigated. The LCs were subsequently mixed with a glassy hydrogen-bond accepting polymer (P4VP) and selectively hydrogen-bond accepting block copolymer (PS-b-P4VP) in various molar ratios. This modular approach results in the formation of a range of glassy nanostructured morphologies in which the phase behavior can be controlled by the mixing ratio. By

mixing the LCs with a block copolymer, oriented hierarchical structures were generated, including Sm-in-LAM and Col_{Hex}-in-LAM morphologies. The synergistic co-assembly was used to obtain vertical alignment of the sub-5 nm Sm and Col_{Hex} features, which could lead to the fabrication of dense line spaces and contact holes, respectively.

In perspective, the sandwiching of the sub-5 nm LC features between PS lamellae has potential to eliminate not only the need for both a top-coat (to control surface-air interactions)^[52-54], but also the need for a neutral brush layer at the interface of the substrate. Shown here for orienting a low surface energy material, it suggests that this novel approach of orienting is generally applicable to a broad range of materials. Moreover, the method presents a facile approach towards the preparation of monolayers, which is generally applicable, and less sensitive to spin-coating conditions. Removal of the polymeric top layer by conventional dry etching techniques would result in glassy resist material with sub-5 nm features and high etch contrast.

6.4. Materials & Methods

Heptasiloxane monohydride was obtained from the group of Meijer. All other solvents and standard chemicals were obtained from commercial sources and were used as received. Reactions with air or moisture sensitive reagents were performed under argon atmosphere with flame-dried glassware using standard Schlenk techniques. Nuclear magnetic resonance spectra (NMR spectra) were measured on a Varian Mercury 400Vx and a Bruker 400MR NMR apparatus at 300 K. Chemical shifts are indicated as δ values in parts per million (ppm) and are reported relative to CHCl₃. Mass spectra were measured on a Bruker ST-A2130 mass spectrometer with matrix-assisted laser desorption ionization and a time-of-flight analyzer (MALDI-TOF) using a 2 kHz laser. Depending on the measured substance, α -cyano-4-hydroxycinnamic acid (CHCA) or 2-[(2E)-3-(4-tert-butylphenyl)-2-methylprop-2-enylidene]malononitrile (DCTB) in tetrahydrofuran (THF) were applied as matrices. Substances were detected with a Bruker Flash Detector. Polarized optical microscopy (POM) was performed with crossed polarizers using a Leica DM6000M equipped with a DFC420C camera and a Linkam THMS600 hot-stage for temperature control. For characterization of the LC textures, a small amount of LC material was placed between microscope slides, heated to the isotropic phase, and cooled (5 °C min⁻¹) to room temperature. Phase transition temperatures of the reactive mesogens were determined using a TA Instrument Q1000 differential scanning calorimeter (DSC). 3-4 mg of material was hermitically

sealed in aluminum pans. The heating and cooling rate was 5 °C min⁻¹ and the second cooling curve was used to determine the transition temperatures. X-ray scattering measurements were performed on a Ganesha lab instrument equipped with a GeniX-Cu ultralow divergence source producing X-ray photons with a wavelength of 1.54 Å and a flux of 1x10⁸ phs⁻¹. Scattering patterns were collected using a Pilatus 300 K silicon pixel detector. The beam center and the q range were calibrated using the diffraction peaks of silver behenate. The sample to detector distance was 91 mm for wide-angle measurements, 441 mm for medium-angle measurements, and 1041 mm for small-angle measurements. The spectra were concatenated at q = 0.7 nm⁻¹ and q = 5 nm⁻¹. Small-angle grazing incidence XRD was performed at the DUBBLE beamline at ESRF in Grenoble. Samples were measured at the critical angle (~ 0.18°). The AFM data were recorded in ambient conditions using a Dimension ICON atomic force microscope (Bruker Nano Inc., Santa Barbara, CA) fitted with an NCHV silicon probe (Bruker, spring constant 42 Nm⁻¹ and a resonance frequency 320 kHz). Fourier transform infrared spectroscopy (FTIR) spectra were obtained using a FTS 6000 spectrometer from Bio-Rad equipped with Specac Golden gate diamond ATR and were signal-averaged over 50 scans at a resolution of 1 cm⁻¹. The degree of hydrogen bonding was generated using formula 1 with the inert FT-IR absorption at 1498 cm⁻¹ as an internal reference.

6.5. Synthetic procedures

Benzyl 4-(but-3-en-1-yloxy)benzoate (1a)

A solution of 4.50 g of benzyl paraben (19.7 mmol, 1.0 eq.), 8.17 g of potassium carbonate (59.1 mmol, 3.0 eq.), 2.65g of 4-bromobut-1-ene (19.6 mmol, 0.99 eq.), and 0.010 g of potassium iodide (0.06 mmol, 0.003 eq.) in 100 mL of acetone is stirred is refluxed under argon for 24h . The solution is washed with 1M NaOH and brine, and dried over magnesium sulfate. Column chromatography (heptane: ethyl acetate = 10:1, [UV]) was performed to give 22% of benzyl 4-(but-3-en-1-yloxy)benzoate (**1a**) (1.22 g, 4.32 mmol) as a transparent liquid. ¹H-NMR (400 MHz, CDCl₃, 300 K): δ [ppm] = 8.07 – 7.98 (m, 2H), 7.48 – 7.29 (m, 5H), 6.95 – 6.87 (m, 2H), 5.90 (ddt, J = 17.1, 10.2, 6.7 Hz, 1H), 5.34 (s, 1H), 5.23 – 5.08 (m, 2H), 4.06 (t, J = 6.7 Hz, 2H), 2.56 (qt, J = 6.7, 1.4 Hz, 2H). ¹³C NMR (100 MHz, CDCl₃, 300 K): δ [ppm] = 166.15, 162.77, 136.30, 134.01, 131.71, 128.54, 128.12, 128.09, 122.48, 117.32, 117.31, 114.12, 77.33, 77.01, 76.69, 67.34, 66.37, 33.45. (MALDI-TOF): *m/z* = calculated (C₁₇H₁₆O₃): 268.11; found: 268.35 [M+H]⁺.

Benzyl 4-(undec-10-en-1-yloxy)benzoate (1b)

A solution of 4.2 g of benzyl paraben (18.4 mmol, 1.0 eq.), 7.50 g of potassium carbonate (54.3 mmol, 2.95 eq.), 4.30 g of 11-bromoundec-1-ene (18.8 mmol, 1.02 eq.), and 0.010 g of potassium iodide (0.06 mmol, 0.003 eq.) in 100 mL of acetone is stirred and refluxed under argon for 48 h. The solution is washed with 1 M NaOH and brine, and dried over magnesium sulfate. Column chromatography (heptane: ethyl acetate = 20:1, [UV]) was performed to give 71% of benzyl 4-(but-3-en-1-yloxy)benzoate (**1b**) (4.95 g, 13.0 mmol) as a transparent liquid. ¹H-NMR (400 MHz, CDCl₃, 300 K): δ [ppm] = 8.02 (dd, *J* = 8.8, 1.7 Hz, 2H), 7.48 – 7.29 (m, 5H), 6.94 – 6.86 (m, 2H), 5.34 (s, 2H), 5.05 – 4.89 (m, 2H), 4.00 (t, *J* = 6.6 Hz, 2H), 2.10 – 1.99 (m, 2H), 1.79 (dt, *J* = 14.7, 6.6 Hz, 2H), 1.52 – 1.27 (m, 14H). ¹³C NMR (100 MHz, CDCl₃, 300 K): δ [ppm] = 166.20, 163.04, 139.17, 136.34, 131.70, 128.53, 128.07, 122.24, 114.12, 68.19, 66.33, 33.79, 29.47, 29.39, 29.32, 29.09, 28.91, 25.96. (MALDI-TOF): *m/z* = calculated (C₂₅H₃₂O₃): 403.23; found: 403.26 [M+Na]⁺.

Benzyl 4-(4-(pentadecamethylheptasiloxanyl)butoxy)benzoate (**2a**)

A flame-dried Schlenk flask is charged with 730 mg of compound **1a** (2.59 mmol, 1.05 eq.), 1278 mg of 1,1,1,3,3,5,5,7,7,9,9,11,11,13,13-pentadecamethylheptasiloxane (2.46 mmol, 1.0 eq.) and one drop of Karstedt's catalyst (2% Platinum(0)-1,3-divinyl-1,1,3,3-tetramethyldisiloxane complex solution in xylene) in 1 mL of dry dichloromethane under argon. The reaction mixture is stirred at room temperature for 3 hours under argon and then quenched with 40 mL of methanol. The solvents are removed under vacuum. Chromatography (heptane:ethyl acetate 20:1, [UV]) was performed to give 93% (1.84 g, 2.30 mmol) of **2a** as a colourless oil. ¹H-NMR (400 MHz, CDCl₃, 300 K): δ [ppm] = 8.08 – 7.96 (m, 2H), 7.51 – 7.29 (m, 5H), 6.99 – 6.80 (m, 2H), 5.34 (s, 2H), 4.01 (t, *J* = 6.4 Hz, 2H), 1.83 (p, *J* = 6.7 Hz, 2H), 1.59 – 1.44 (m, 2H), 0.70 – 0.51 (m, 2H), 0.14 – 0.02 (m, 45H). ¹³C NMR (100 MHz, CDCl₃, 300 K): δ [ppm] = 166.21, 163.07, 136.33, 131.68, 128.53, 128.06, 122.22, 114.05, 67.81, 66.32, 32.58, 19.71, 17.91, 1.78, 1.17, 1.14, 1.06, 0.16. (MALDI-TOF): *m/z* = calculated (C₃₃H₆₄O₉Si₇): 800.29; found: 823.30 [M+Na]⁺.

4-((11-(Pentadecamethylheptasiloxanyl)undecyl)oxy)benzoate (**2b**)

A flame-dried Schlenk flask is charged with 704 mg of compound **1b** (1.85 mmol, 1.00 eq.), 988 mg of 1,1,1,3,3,5,5,7,7,9,9,11,11,13,13-pentadecamethylheptasiloxane (1.90 mmol, 1.03 eq.) and one drop of Karstedt's catalyst (2% Platinum(0)-1,3-divinyl-1,1,3,3-tetramethyldisiloxane complex solution in xylene) in 3 mL of dry dichloromethane under argon. The reaction mixture is stirred

at room temperature for 3 hours under argon and then quenched with 40 mL of methanol. The solvents are removed under vacuum. Chromatography (heptane : ethyl acetate 20:1, [UV]) was performed to give 90% benzyl 4-(4-(pentadecamethylheptasiloxanyl)butoxy)benzoate (**2b**) (1.50 g, 1.67 mmol) as a colourless oil. $^1\text{H-NMR}$ (400 MHz, CDCl_3 , 300 K): δ [ppm] = δ 8.08 – 7.96 (m, 2H), 7.51 – 7.29 (m, 5H), 6.99 – 6.80 (m, 2H), 5.33 (s, 2H), 3.99 (t, J = 6.4 Hz, 2H), 1.79 (m, 2H), 1.52 – 1.27 (m, 16H), 0.53 (dd, J = 9.5, 5.7 Hz, 2H), 0.14 – 0.02 (m, 45H). $^{13}\text{C NMR}$ (100 MHz, CDCl_3 , 300 K): δ [ppm] = 166.21, 163.05, 136.33, 131.69, 128.53, 128.06, 122.22, 114.05, 68.21, 66.32, 33.45, 29.62, 29.58, 29.56, 29.38, 29.10, 25.98, 23.21, 18.25, 1.78, 1.14, 1.05, 0.18. (MALDI-TOF): m/z = calculated ($\text{C}_{40}\text{H}_{78}\text{O}_9\text{Si}_7$): 898.40; found: 921.42 [$\text{M}+\text{Na}$] $^+$.

4-(4-(Pentadecamethylheptasiloxanyl)butoxy)benzoic acid (LC1)

A 100 mL flask is charged with 1.47 g (1.63 mmol) of compound **2a**, and 2 mL of ethyl acetate. To this is added 100 mg Pd/C 30% in 6 mL of ethanol. The flask is fitted with a rubber stopper and stirred overnight under H_2 atmosphere. The solution is filtered over celite and solvents are removed under vacuum to yield 98% of **LC1** (1.29 g, 1.60 mmol) as a transparent liquid. $^1\text{H-NMR}$ (400 MHz, CDCl_3 , 300 K): δ [ppm] = 8.13 – 7.98 (m, 2H), 7.06 – 6.83 (m, 2H), 4.03 (t, J = 6.4 Hz, 2H), 1.84 (m, 2H), 1.52 (m, 2H), 0.68 – 0.55 (m, 2H), 0.13 – 0.02 (m, 45H). $^{13}\text{C NMR}$ (100 MHz, CDCl_3 , 300 K): δ [ppm] = 171.66, 163.68, 132.29, 121.34, 114.16, 67.88, 32.56, 19.72, 17.90, 1.77, 1.16, 1.13, 1.07, 1.05, 0.16. (MALDI-TOF): m/z = calculated ($\text{C}_{26}\text{H}_{58}\text{O}_9\text{Si}_{11}$): 733.24; found: 733.23 [$\text{M}+\text{Na}$] $^+$.

4-(11-(Pentadecamethylheptasiloxanyl)undecyl)oxy)benzoic acid (LC2)

A 100 mL flask is charged with 1.47 g (1.63 mmol) of compound **2b**, and 2 mL of ethyl acetate. To this is added 100 mg Pd/C 30% in 6 mL of ethanol. The flask is fitted with a rubber stopper and stirred overnight under H_2 atmosphere. The solution is filtered over celite and solvents are removed under vacuum to yield 98% of **LC2** (1.29 g, 1.60 mmol) as a transparent paste. $^1\text{H-NMR}$ (400 MHz, CDCl_3 , 300 K): δ [ppm] = δ 8.05 (m, 2H), 6.93 (m, 2H), 4.02 (t, J = 6.4 Hz, 2H), 1.81 (m, 2H), 1.52 – 1.27 (m, 16H), 0.54 (dd, J = 9.5, 5.7 Hz, 2H), 0.14 – 0.02 (m, 45H). $^{13}\text{C NMR}$ (100 MHz, CDCl_3 , 300 K): δ [ppm] = 171.91, 163.66, 132.30, 121.40, 114.15, 68.27, 33.45, 29.59, 29.39, 29.09, 25.98, 23.22, 18.26, 1.77, 1.16, 1.05, 0.18. (MALDI-TOF): m/z = calculated ($\text{C}_{33}\text{H}_{72}\text{O}_9\text{Si}_7$): 831.35; found: 831.35 [$\text{M}+\text{Na}$] $^+$.

6.6. References

- [1] M. O'Neill, S. M. Kelly, in *Liq. Cryst. Semicond.* (Eds.: R.J. Bushby, S.M. Kelly, M. O'Neill), Springer Netherlands, **2013**, pp. 247–268.
- [2] S. Sergeev, W. Pisula, Y. H. Geerts, *Chem. Soc. Rev.* **2007**, *36*, 1902.
- [3] M. Kumar, S. Kumar, *Polym. J.* **2017**, *49*, 85.
- [4] Y. Shimizu, in *Nanosci. Liq. Cryst.* (Ed.: Q. Li), Springer International Publishing, **2014**, pp. 257–280.
- [5] M. O'Neill, S. M. Kelly, in *Liq. Cryst. Semicond.* (Eds.: R.J. Bushby, S.M. Kelly, M. O'Neill), Springer Netherlands, **2013**, pp. 219–245.
- [6] C. L. Gonzalez, C. W. M. Bastiaansen, J. Lub, J. Loos, K. Lu, H. J. Wondergem, D. J. Broer, *Adv. Mater.* **2008**, *20*, 1246.
- [7] M. Zhou, T. J. Kidd, R. D. Noble, D. L. Gin, *Adv. Mater.* **2005**, *17*, 1850.
- [8] X. D. Feng, M. E. Tousley, M. G. Cowan, B. R. Wiesnauer, S. Nejati, Y. Choo, R. D. Noble, M. Elimelech, D. L. Gin, C. O. Osuji, *ACS Nano* **2014**, *8*, 11977.
- [9] J. R. Werber, C. O. Osuji, M. Elimelech, *Nat. Rev. Mater.* **2016**, *1*, 16018.
- [10] S. Hara, H. Wada, A. Shimojima, K. Kuroda, *ACS Nano* **2017**, *11*, 5160.
- [11] K. Nickmans, J. N. Murphy, B. de Waal, P. Leclère, J. Doise, R. Gronheid, D. J. Broer, A. P. H. J. Schenning, *Adv. Mater.* **2016**, *28*, 10068.
- [12] R. H. Zha, B. F. de Waal, M. Lutz, A. J. Teunissen, E. W. Meijer, *J. Am. Chem. Soc.* **2016**, *138*, 5693.
- [13] J. A. Berrocal, R. H. Zha, B. F. M. de Waal, J. A. M. Luggner, M. Lutz, E. W. Meijer, *ACS Nano* **2017**, *11*, 3733.
- [14] Q. Ye, H. Zhou, J. Xu, *Chem. – Asian J.* **2016**, *11*, 1322.
- [15] X. Yu, K. Yue, I. F. Hsieh, Y. Li, X. H. Dong, C. Liu, Y. Xin, H. F. Wang, A. C. Shi, G. R. Newkome, R. M. Ho, E. Q. Chen, W. B. Zhang, S. Z. Cheng, *Proc. Natl. Acad. Sci. USA* **2013**, *110*, 10078.
- [16] X. Feng, K. Kawabata, G. Kaufman, M. Elimelech, C. O. Osuji, *ACS Nano* **2017**, *11*, 3911.
- [17] K. Kwon, J. M. Ok, Y. H. Kim, J.-S. Kim, W.-B. Jung, S.-Y. Cho, H.-T. Jung, *Nano Lett.* **2015**, *15*, 7552.
- [18] J. G. Son, K. W. Gotrik, C. A. Ross, *ACS Macro Lett.* **2012**, *1*, 1279.
- [19] S. Wu, *Polymer Handbook*, Wiley-Interscience, New York, New York, **1989**.
- [20] K. Lee, M. Kreider, W. Bai, L.-C. Cheng, S. S. Dinachali, K.-H. Tu, T. Huang, K. Ntetsikas, G. Lontos, A. Avgeropoulos, C. A. Ross, *Nanotechnology* **2016**, *27*, 465301.
- [21] I. Davidi, D. Patra, D. Hermida-Merino, G. Portale, V. M. Rotello, U. Raviv, R. Shenhar, *Macromolecules* **2014**, *47*, 5774.
- [22] S. Valkama, O. Lehtonen, K. Lappalainen, H. Kosonen, P. Castro, T. Repo, M. Torkkeli, R. Serimaa, G. ten Brinke, M. Leskelä, O. Ikkala, *Macromol. Rapid Commun.* **2003**, *24*, 556.

- [23] S. Valkama, T. Ruotsalainen, A. Nykänen, A. Laiho, H. Kosonen, G. ten Brinke, O. Ikkala, J. Ruokolainen, *Macromolecules* **2006**, *39*, 9327.
- [24] J. Ruokolainen, R. Makinen, M. Torkkeli, T. Makela, R. Serimaa, G. ten Brinke, O. Ikkala, *Science* **1998**, *280*, 557.
- [25] O. Ikkala, G. ten Brinke, *Science* **2002**, *295*, 2407.
- [26] O. Ikkala, G. ten Brinke, *Chem. Commun.* **2004**, 2131.
- [27] M. Faber, A. H. Hofman, E. Polushkin, G. A. van Ekenstein, J. Seitsonen, J. Ruokolainen, K. Loos, G. ten Brinke, *Macromolecules* **2013**, *46*, 500.
- [28] A. H. Hofman, M. Reza, J. Ruokolainen, G. ten Brinke, K. Loos, *Macromolecules* **2014**, *47*, 5913.
- [29] G. ten Brinke, J. Ruokolainen, O. Ikkala, in *Hydrog. Bond. Polym.* (Ed.: W. Binder), Springer Berlin Heidelberg, **2007**, pp. 113–177.
- [30] S.-J. Wang, Y.-S. Xu, S. Yang, E.-Q. Chen, *Macromolecules* **2012**, *45*, 8760.
- [31] J. Ruokolainen, M. Saariaho, O. Ikkala, G. ten Brinke, E. L. Thomas, M. Torkkeli, R. Serimaa, *Macromolecules* **1999**, *32*, 1152.
- [32] Y. Cai, M. Zheng, Y. Zhu, X.-F. Chen, C. Y. Li, *ACS Macro Lett.* **2017**, *6*, 479.
- [33] T.-Y. Lai, C.-Y. Cheng, W.-Y. Cheng, K.-M. Lee, S.-H. Tung, *Macromolecules* **2015**, *48*, 717.
- [34] A. H. Hofman, Y. Chen, G. ten Brinke, K. Loos, *Macromolecules* **2015**, *48*, 1554.
- [35] G. T. Brinke, O. Ikkala, *Chem. Rec.* **2004**, *4*, 219.
- [36] B. K. Kuila, E. B. Gowd, M. Stamm, *Macromolecules* **2010**, *43*, 7713.
- [37] R. Mäki-Ontto, K. de Moel, W. de Odorico, J. Ruokolainen, M. Stamm, G. ten Brinke, O. Ikkala, *Adv. Mater.* **2001**, *13*, 117.
- [38] W.-T. Chuang, T.-Y. Lo, Y.-C. Huang, C.-J. Su, U.-S. Jeng, H.-S. Sheu, R.-M. Ho, *Macromolecules* **2014**, *47*, 6047.
- [39] I. Vukovic, T. P. Voortman, D. H. Merino, G. Portale, P. Hiekkataipale, J. Ruokolainen, G. ten Brinke, K. Loos, *Macromolecules* **2012**, *45*, 3503.
- [40] R. Bertani, P. Metrangolo, A. Moiana, E. Perez, T. Pilati, G. Resnati, I. Rico-Lattes, A. Sassi, *Adv. Mater.* **2002**, *14*, 1197.
- [41] B. J. Rancatore, C. E. Mauldin, J. M. J. Fréchet, T. Xu, *Macromolecules* **2012**, *45*, 8292.
- [42] A. Priimagi, J. Vapaavuori, F. J. Rodriguez, C. F. J. Faul, M. T. Heino, O. Ikkala, M. Kauranen, M. Kaivola, *Chem. Mater.* **2008**, *20*, 6358.
- [43] J. del Barrio, E. Blasco, C. Toprakcioglu, A. Koutsioubas, O. A. Scherman, L. Oriol, C. Sanchez-Somolinos, *Macromolecules* **2014**, *47*, 897.
- [44] J. del Barrio, E. Blasco, L. Oriol, R. Alcalá, C. Sánchez-Somolinos, *J. Polym. Sci. Part Polym. Chem.* **2013**, *51*, 1716.
- [45] J. de Wit, G. A. van Ekenstein, E. Polushkin, K. Kvashnina, W. Bras, O. Ikkala, G. ten Brinke, *Macromolecules* **2008**, *41*, 4200.
- [46] S. H. Tung, N. C. Kalarickal, J. W. Mays, T. Xu, *Macromolecules* **2008**, *41*, 6453.

- [47] B. van Genabeek, B. F. M. de Waal, M. M. J. Gosens, L. M. Pitet, A. R. A. Palmans, E. W. Meijer, *J. Am. Chem. Soc.* **2016**, *138*, 4210.
- [48] M. Lee, B. K. Cho, H. Kim, J. Y. Yoon, W. C. Zin, *J. Am. Chem. Soc.* **1998**, *120*, 9168.
- [49] H. Takahashi, K. Mamola, E. K. Plyler, *J. Mol. Spectrosc.* **1966**, *21*, 217.
- [50] J. Y. Lee, P. C. Painter, M. M. Coleman, *Macromolecules* **1988**, *21*, 954.
- [51] J. Gao, Y. He, F. Liu, X. Zhang, Z. Wang, X. Wang, *Chem. Mater.* **2007**, *19*, 3877.
- [52] C. M. Bates, T. Seshimo, M. J. Maher, W. J. Durand, J. D. Cushen, L. M. Dean, G. Blachut, C. J. Ellison, C. G. Willson, *Science* **2012**, *338*, 775.
- [53] C. Sinturel, F. S. Bates, M. A. Hillmyer, *ACS Macro Lett.* **2015**, *4*, 1044.
- [54] H. S. Suh, D. H. Kim, P. Moni, S. Xiong, L. E. Ocola, N. J. Zaluzec, K. K. Gleason, P. F. Nealey, *Nat. Nanotechnol.* **2017**, *12*, 575.



Chapter 7

Epilogue

This chapter is based on:

K. Nickmans, A. P. H. J. Schenning, *Adv. Mater* (*accepted*)

7.1. Introduction

This thesis describes the development of a novel class of oligo(dimethylsiloxane) liquid crystals that form ordered hybrid organic/inorganic thin film nanostructures with ultrafine sub-5 nm dimensions, their directed self-assembly into macroscopically oriented patterns by grapho-epitaxy and photoalignment, and retention of the patterns by covalent photo cross-linking or cooling through a glass transition. In this chapter, we provide an outlook for this novel class of materials in the form of next challenges. We further reflect more broadly on the work described in this thesis and discuss opportunities, with a specific focus on their use as self-assembled resists for nanopatterning.

7.2. Future challenge of sub-5 nm patterning using liquid crystals

With respect to feature sizes, the sub-5 nm features reported in this thesis are far ahead of the scaling curve pursued by the semiconductor industry (Figure 1). This observation suggests that several critical challenges must be overcome for these materials to be integrated into existing patterning technologies. Most notably, the critical challenges are related to the development of suitable pattern transfer techniques, mechanical stability of the ultra-fine features, the application of appropriate metrology tools, and the integration of the required processing operations into fabrication facilities.

7.2.1. Integration

As shown in chapter 2, oligo(dimethylsiloxane) liquid crystals, and by extension all liquid crystals, are highly compatible with graphoepitaxial processes, the most well-established alignment and pattern registration technique in block copolymer directed self-assembly.^[1] In principle, this allows the integration of LC materials with existing patterning techniques for their extension through directed self-assembly (Figure 1). However, the graphoepitaxial features produced by optical lithography are not perfect, but contain their own variations known as line edge roughness (LER). LER is caused by a number of statistically fluctuating effects at small dimensions such as photon flux variations, statistical distributions of chemical species in the resist, and the nonzero size of polymers being dissolved during development. For the precise registration of LC patterns within a trench of varying width, the LER must be smaller than the feature size (<1 nm). Currently, the LER tolerance for logic patterning (transistors) is approximately 1.5 nm (3 σ), which is set to decrease to 0.7

nm by 2025. This would enable integration with LC materials.^[2] As indicated in Figure 1, the LER requirement for extension of DSA to LC materials might be provided by optical immersion lithography, EUV lithography, or e-beam lithography.

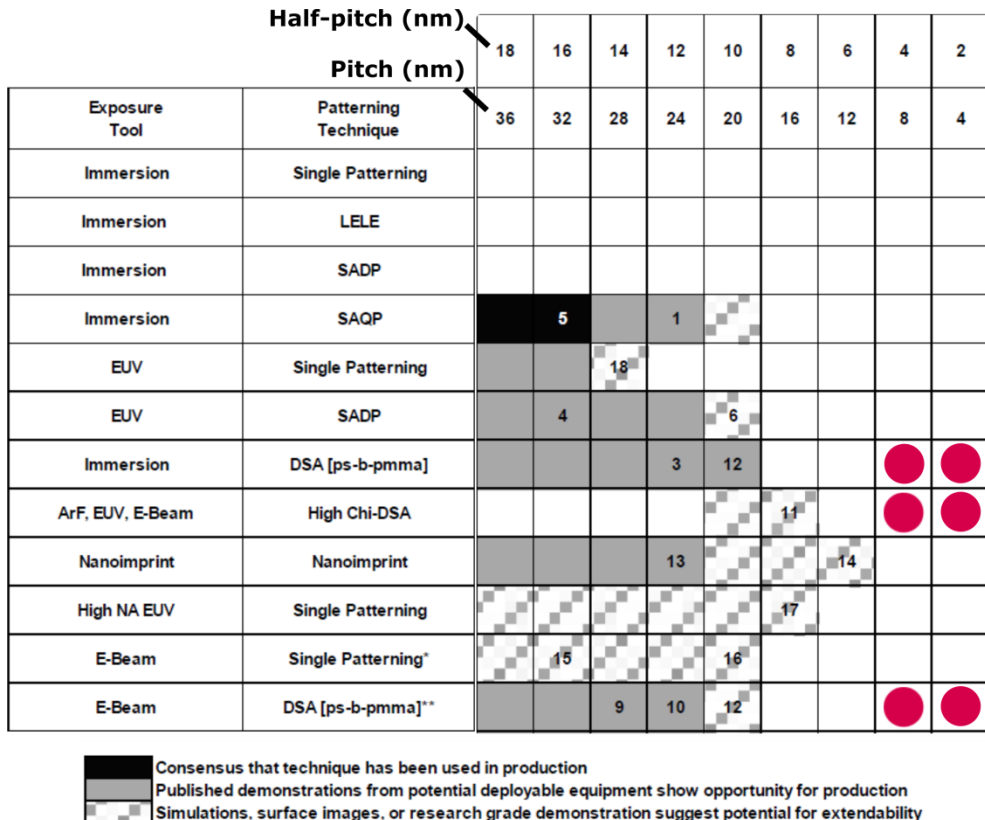


Figure 1. Demonstrated resolution of potential new patterning techniques, adapted from ^[2]. Possible applications of ODMS LCs are indicated with a circle.

7.2.2. Pattern transfer

Pattern transfer is by far the most widely recognized bottleneck for sub-5 nm patterning. Common pattern transfer methods, such as plasma etching, become more precarious at these length scales, since the processing requirements become increasingly stringent and the processing windows are narrowed.^[3] These processes will have to be severely optimized to allow high fidelity pattern transfer, which represents a formidable challenge. Fortunately, there is still room for etch

optimization of the self-assembled materials through molecular design, or through the selective incorporation of inorganic precursors after the self-assembly.

For block copolymers, the latter method has established itself as a promising technique to improve pattern transfer.^[3-7] The method, commonly referred to as sequential infiltration synthesis (SIS), is related to atomic layer deposition (ALD). It is a cyclic, gas phase process based on self-limiting chemical reactions of a metal precursor with a specific domain after infiltration into a block copolymer thin film. Darling et al. first demonstrated SIS on a PS-*b*-PMMA block copolymer film using alternate cycles of tetramethylaluminium (TMA) and water vapor. TMA forms localized Al-OH and Al-CH₃ sites on the PMMA carbonyl moieties, while water produces layers of Al₂O₃. After the SIS process, sufficient etch contrast was embedded in the film to allow the production of high aspect ratio features by plasma etching (Figure 2). More recent work by Hillmyer and coworkers demonstrated the extension of the SIS process with a high- χ BCP with sub-10 nm feature sizes.^[8] To date, SIS has not been demonstrated for sub-5 nm phases.

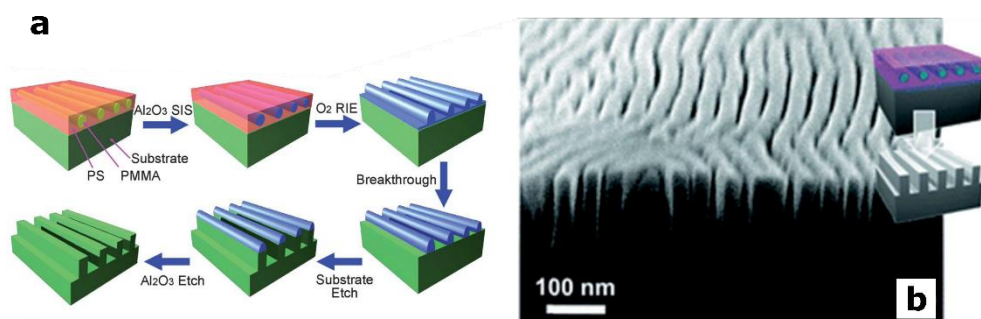


Figure 2. a) Schematic description of sequential infiltration synthesis for the fabrication of nanowires. The self-assembled nanodomains are selectively infiltrated with metals (by SIS) that enhances the etch contrast, and subsequently used for pattern transfer to develop high-aspect ratio features. b) Nanowires fabricated using SIS on a PS-*b*-PMMA block copolymer. Reproduced from ^[7] with permission from The Royal Society of Chemistry.

In order to obtain inorganic nanostructure arrays at the sub-5 nm scale, it is essential for pattern transfer processes such as plasma etching and SIS to proceed in a controlled fashion with high selectivity, and at defined positions within the self-assembled building blocks. The key herein will be the preparation of well-defined supramolecular architectures with a one-to-one registration of molecular components or reactive sites, and extremely sharp interfaces.^[9-11] LC materials are ideally suited to address these challenges because, besides the sub-5 nm

periodicities, control over the chemical functionality allows for site-selective chemistry such as cross-linking, selective swelling or complexation.^[12,13] Supramolecular interactions such as hydrogen bonding may direct individual reactive sites, positively impacting the processes of selective plasma etching or inorganic material growth with sub-nanometer resolution. Moreover, the multiple orthogonal supramolecular interactions at the root of the self-assembly, in combination with a chemical monodispersity, result in highly ordered mesophases with well-defined lattices and sharp interfaces. This stands in contrast with low molecular weight BCPs which exhibit ill-defined interfaces due to composition fluctuation effects in the weak segregation regime ($\chi N \sim 10.5$).^[14]

Mechanical stability of the sub-5 nm patterns is required for their utilization as templates for pattern transfer. For LCs, this is typically achieved by chemical crosslinking of reactive mesogens to form a nanostructured polymer, usually by UV-polymerization, since it can be performed at the temperature corresponding to the desired mesophase (chapter 5). For pattern transfer in nanolithography, the in-situ polymerization of reactive LC monomers is highly challenging since defects can originate from the multi-component nature of the reactive thin films (LC, photoinitiator, inhibitor), and the polymerization shrinkage effect (chapter 5). An alternate approach consists of engineering an appropriate glass transition into the LC material through molecular design. Unfortunately, while glass transition behavior is observed in some LCs, it is not well understood, and additional fundamental research is required.^[15] From this perspective, the complexation of LCs with glassy polymers through supramolecular interactions could be a more practical method to fabricate systems with tunable dimensions (chapter 6).^[16,17]

7.2.3. Defect density & alignment

Defect densities are another major concern for the semiconductor industry.^[18] While defects like dislocations and disclinations become thermodynamically more favorable with low molecular weight materials, the kinetic barrier associated with defect annihilation is greatly reduced. In practice therefore, low molecular weight materials display long range order, even when undirected, as typified by POM birefringence experiments of thermotropic liquid crystals. In addition, low defect densities are observed as a result of the improved ability to anneal away defects and direct the self-assembly (see chapter 2). Particularly near the order-disorder transition, where the barrier associated with defect annihilation becomes $\ll k_B T$, fast self-assembly dynamics are observed.^[19] For liquid crystals, a common method to obtain monolithically oriented samples is by transitioning through several phases

from a low to high order. The design of materials with nematic phases (orientational order only), in addition to higher-order phases at lower temperatures, may therefore aid in obtaining monolithic alignment. As demonstrated in chapter 4, photo-alignment is a promising method to remove defects in a noncontact manner. The extension of computer simulation methods currently applied to BCP systems, would enable both further understanding of the mechanisms of defect annihilation and optimal LC design for high order and minimal defectivity.

Having demonstrated the graphoepitaxy of planar-oriented LC cylinders in chapter 2, it would be beneficial to develop this approach for the vertical orientation of sub-5 nm features which would allow the maximization of etch contrast throughout the thickness of the film. Studies show that control over the surface energy of the template bottom and sidewall is crucial for achieving vertically oriented features, which can be achieved by selectively modifying the surfaces with a polymer brush.^[20,21] Extension of the graphoepitaxy process explored in chapter 2 to these vertically oriented systems would be highly interesting. As shown in chapter 6, vertically oriented features could also be obtained by using the hierarchical self-assembly of supramolecular LC/BCP systems. Obtaining vertically oriented features becomes increasingly challenging for soft building blocks with highly immiscible components, such as high- χ , low-N BCPs or hybrid organic/inorganic LCs. Since the respective surface energies are increasingly disparate, the development of interfaces which are neutral to both components is increasingly difficult. The development of surface active components, in the form of additives ^[22] or built-in components, ^[23] may help to achieve this goal, although they will need to be tailored to each supramolecular system. In this context, hierarchical materials produced by block copolymer supramolecular assemblies present an exciting opportunity, since these materials self-assemble with an inherent orthogonality (chapter 6). Modifying a substrate surface to be attractive to a polymer block may therefore be a general method by which to control the orientation of the liquid crystal mesophase contained within the BCP layers.

It would also be worthwhile to combine the hierarchical materials explored in chapter 6 with the photo-alignment processes developed in chapter 4, in order to obtain vertically oriented monodomain structures by exposure to linearly polarized light (Figure 3a). A light-responsive, hydrogen-bonding, ODMS-based liquid crystal such as the one shown in Figure 3b would be suitable; for its combination of benzoic acid moiety (hydrogen bonding), azobenzene moiety (photoalignment), and ODMS (etch contrast).

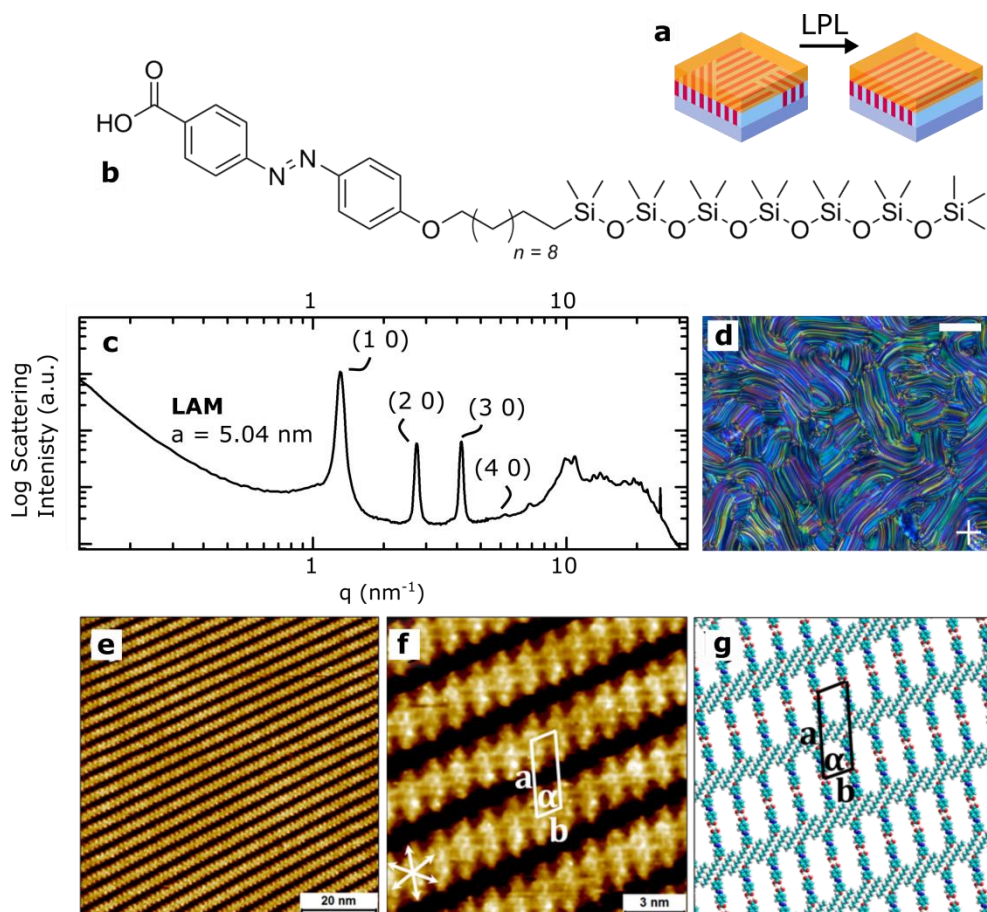


Figure 3. a) Schematic representation of photo-alignment of vertically oriented hierarchically structured thin films using linearly polarized light. b) Chemical structure of a light-responsive hydrogen-bonding ODMS-based liquid crystal. c) X-ray scattering data obtained at room temperature. The assigned lattice and miller indices are indicated in the figure. d) Polarized optical microscopy image obtained at room temperature under crossed polarizers. The polarizer axes are shown in the image. Scale bar: 100 μm . e-f) STM images of a self-assembled monolayer at the solid-liquid interface ($C = 1.0 \times 10^{-4}$ M). The crosses represent the graphite symmetry axes. g) Molecular model showing the arrangement of molecules in the self-assembled monolayer, in which the ODMS chain is omitted for the sake of clarity. The unit cell is overlaid on the STM image and the cell parameters are: $a = 3.9 \pm 0.1$ nm, $b = 1.4 \pm 0.1$ nm and $\alpha = 71.0 \pm 1.0^\circ$.

The material shown in Figure 3b was synthesized and investigated for its bulk phase behavior. As indicated by bulk XRD (Figure 3c), lamellar features with a lattice spacing of $a = 5.04$ nm are formed at room temperature. Since this value is

approximately double the molecular length, it is assumed that hydrogen bonded dimers are formed. While there are some higher-order scatterings in the wide-angle region ($q > 10 \text{ nm}^{-1}$), the typical textures observed in polarized optical microscopy (Figure 3d) indicate that the material is liquid crystalline. The additional reflections are likely due to partial crystallization of the alkyl tail. The self-assembly of the compound was further investigated at the solid-liquid interface of highly oriented pyrolytic graphite (HOPG) using scanning tunneling microscopy (STM) (Figure 3e-f). Large scale STM images (Figure 3e) indicate the formation of large domains (several 100 nm^2) consisting of lamellar features. Molecular resolution STM images such as the one shown in Figure 3f reveal that the bright features arise from rows of rod shaped structures, which always appear in pairs. These rod like features correspond to the aromatic part of the molecules and their pairwise appearance indicates presence of hydrogen-bonded dimers on the surface, as expected from the molecular structure (Figure 3b).

7.2.4. Metrology

The need persists for appropriate metrology tools for the characterization of sub-5 nm patterned thin films where near-atomic resolution is required to accurately image features and defects. It is currently highly challenging to obtain structural information at this length scale using common top-down imaging techniques such as scanning electron microscopy (SEM) and atomic force microscopy (AFM). In brief, SEM is limited by its ability to discriminate individual domains through lack of contrast, while AFM is limited by the dimensions of the probe tip. Scanning tunneling microscopy (STM), has an extremely high lateral resolution ($\sim 0.1 \text{ nm}$), enabling the visualization of individual molecules (Figure 3) or even atoms,^[24] but it is limited to the imaging of conductive monolayers on extremely flat, conductive surfaces. Helium ion microscopy (HIM) is a relatively new technique which could be of significant value in the analysis of sub-5 nm patterns. HIM has a resolution between that of SEM and TEM ($\sim 0.3 \text{ nm}$), and an improved material contrast.^[25-27] The technique has been applied to obtain high resolution BCP images (Figure 4),^[27] but it has not been applied to LC thin films.

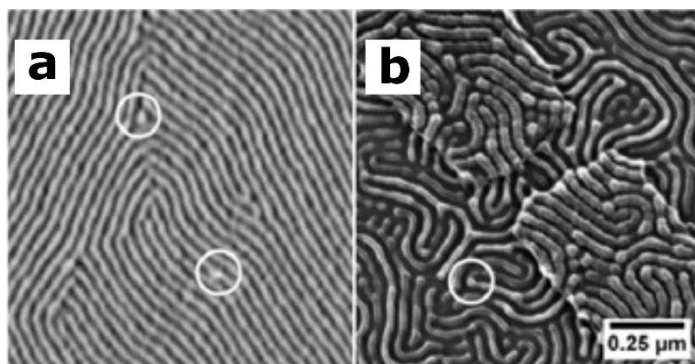


Figure 4. Comparison of SEM and HIM. a) SEM image of a cylinder forming PS-b-PEO. b) HIM image of lamellar PS-b-PMMA showing increased contrast. Both systems have a similar domain spacing (42 nm), and the magnifications are identical.

In order to fully understand the complexity of the thin film structures, it is essential that the 3D morphology is quantified in addition to the 2D surface arrangement. The indirect technique of grazing incidence x-ray diffraction (GIXRD) can be used to probe the average domain structure over large areas (mm^2), but it is relatively insensitive to defects, the domain interfaces, and structural deviations that occur at specific locations within the film (such as at the substrate and air interface). Direct 3D visualization can be achieved by transmission electron microscopy (TEM), but this method is restricted by challenging sample preparation (such as embedding and cross-sectioning). The reliable preparation of LC samples with low viscosity is particularly challenging. From the standpoint of TEM, mechanically stable, glassy morphologies are desirable (as presented in chapter 6).

7.3. Conclusion

In conclusion, the ODMS liquid crystals described in this thesis present unique opportunities for obtaining highly ordered, hybrid organic/inorganic sub-5 nm nanostructured morphologies. Coupled with directed self-assembly for 3D orientational control and large-area alignment, this exciting class of materials could lead to a broad range of impending nanotechnologies, most notably nanopatterning. Given the impact of these technologies, it is foreseeable that this thrilling field will continue to expand at a rapid pace.

7.4. References

- [1] H. Hu, M. Gopinadhan, C. O. Osuji, *Soft Matter* **2014**, *10*, 3867.

- [2] ITRS, **2013**.
- [3] C. Cummins, T. Ghoshal, J. D. Holmes, M. A. Morris, *Adv. Mater.* **2016**, *28*, 5586.
- [4] H. C. Kim, S. M. Park, W. D. Hinsberg, *Chem. Rev.* **2010**, *110*, 146.
- [5] Q. Peng, Y. C. Tseng, S. B. Darling, J. W. Elam, *Adv Mater* **2010**, *22*, 5129.
- [6] Y.-C. Tseng, Q. Peng, L. E. Ocola, D. A. Czaplewski, J. W. Elam, S. B. Darling, *J. Mater. Chem.* **2011**, *21*, 11722.
- [7] M. Ramanathan, Y.-C. Tseng, K. Ariga, S. B. Darling, *J. Mater. Chem. C* **2013**, *1*, 2080.
- [8] L. Yao, L. E. Oquendo, M. W. Schulze, R. M. Lewis, W. L. Gladfelter, M. A. Hillmyer, *ACS Appl. Mater. Interfaces* **2016**, *8*, 7431.
- [9] L. M. Pitet, A. H. M. van Loon, E. J. Kramer, C. J. Hawker, E. W. Meijer, *ACS Macro Lett.* **2013**, *2*, 1006.
- [10] A. Croom, K. B. Manning, M. Weck, *Macromolecules* **2016**, *49*, 7117.
- [11] K. S. Lee, J. Lee, J. Kwak, H. C. Moon, J. K. Kim, *ACS Appl. Mater. Interfaces* **2017**, DOI 10.1021/acsami.6b15885.
- [12] T. Rudolph, F. H. Schacher, *Eur. Polym. J.* **2016**, *80*, 317.
- [13] D. J. Broer, C. M. W. Bastiaansen, M. G. Debije, A. P. H. J. Schenning, *Angew. Chem.-Int. Ed.* **2012**, *51*, 7102.
- [14] S. Kim, P. F. Nealey, F. S. Bates, *Nano Lett* **2014**, *14*, 148.
- [15] S. H. Chen, J. C. Mastrangelo, T. N. Blanton, A. BashirHashemi, K. L. Marshall, *Liq. Cryst.* **1996**, *21*, 683.
- [16] O. Ikkala, G. ten Brinke, *Science* **2002**, *295*, 2407.
- [17] J. Ruokolainen, R. Mäkinen, M. Torkkeli, T. Mäkelä, R. Serimaa, G. ten Brinke, O. Ikkala, *Science* **1998**, *280*, 557.
- [18] M. Muramatsu, T. Nishi, G. You, Y. Saito, Y. Ido, N. Oikawa, T. Tobana, K. Ito, S. Morikita, T. Kitano, in *Proc SPIE 10144*, **2017**, p. 101440Q.
- [19] W. Li, P. F. Nealey, J. J. de Pablo, M. Müller, *Phys. Rev. Lett.* **2014**, *113*, 168301.
- [20] J. Bekaert, J. Doise, R. Gronheid, J. Ryckaert, G. Vandenberghe, G. Fenger, Y. J. Her, Y. Cao, in *Proc SPIE 9658*, **2015**, p. 965804.
- [21] W. Bai, K. Gadelrab, A. Alexander-Katz, C. A. Ross, *Nano Lett.* **2015**, *15*, 6901.
- [22] A. Vora, K. Schmidt, G. Alva, N. Arellano, T. Magbitang, A. Chunder, L. E. Thompson, E. Lofano, J. W. Pitera, J. Y. Cheng, D. P. Sanders, *ACS Appl. Mater. Interfaces* **2016**, *8*, 29808.
- [23] A. Vora, E. Hirahara, J. Cheng, D. Baskaran, O. Polishchuk, M. Tjio, M. Paunescu, D. Sanders, G. Lin, *Block Copolymers with Surface-Active Junction Groups, Compositions and Processes Thereof*, **2016**, WO/2016/131900.
- [24] G. Binnig, H. Rohrer, *Rev. Mod. Phys.* **1987**, *59*, 615.
- [25] *J. Vac. Sci. Technol. B Nanotechnol. Microelectron. Mater. Process. Meas. Phenom.* **2014**, *32*, 020801.
- [26] A. P. Bell, R. SenthamaraiKannan, T. Ghoshal, A. Chaudhari, M. Leeson, M. A. Morris, **2015**, p. 94241R-94241R-13.

- [27] D. Borah, T. Ghoshal, M. T. Shaw, A. Chaudhari, N. Petkov, A. P. Bell, J. D. Holmes, M. A. Morris, *Nanomater. Nanotechnol.* **2014**, 4, 25.

Summary

Directed Self-Assembly of Oligo(dimethylsiloxane) Liquid Crystals for Sub-5 nm Patterning

The exponential downscaling of transistor sizes on integrated circuits over the last half-century, also known as “Moore’s law”, has enabled the onset of personal computers and the advent of today’s powerful mobile devices. During further progression towards a data-driven world with human-level artificial intelligence, the hunger for further scaling according to Moore’s law remains insatiable. While advances in top-down photolithography have traditionally been the driver behind the ability to print smaller features, the design of new photolithography processes is becoming increasingly complex and expensive. Complementary bottom-up patterning technologies based on self-assembly are increasingly attractive avenues by which to extend current processes and ensure the continuation of Moore’s law.

While self-assembly can in principle offer higher feature densities over device-relevant length scales, three grand challenges remain for the adoption of these materials by the semiconductor industry. The first challenge is the alignment of the naturally multi-domain self-assembled patterns into in defect-free thin films with a predetermined orientation. The second challenge is the pattern transfer of the self-assembled morphologies into an inorganic array by selectively etching the respective molecular components. The third challenge relates to the further scaling of the technology in terms of minimum feature sizes. While numerous research groups have focused on the development of novel block copolymer materials, these materials typically run out of steam for self-assembly beyond 10 nm periodicities.

This thesis explores liquid crystals (LCs) as potential materials for sub-5 nm patterning. Chapter one describes the current state-of-the-art with respect to the aforementioned challenges surrounding self-assembly for nanopatterning. Chapter two and three describe the synthesis and characterization of a novel class of oligo(dimethylsiloxane) (ODMS) liquid crystals which form ordered columnar and

lamellar morphologies respectively, at sub-5 nm periodicities in thin films. These materials are able to form inorganic silicon oxides in a single plasma oxidation step, which opens the way to pattern transfer. For the first time, we illustrate the graphoepitaxial alignment of liquid crystal nanopatterns inside topological pre-patterns.

Chapter four describes the direct photo-alignment of the LC nanostructures by actinic light. When exposed to linearly polarized light, an in-plane alignment was achieved. High-resolution AFM imaging indicated the total absence of defects in aligned samples. Time-resolved UV-vis spectroscopy and in-situ grazing-incidence x-ray diffraction experiments revealed that the photo-alignment proceeds most efficiently when performed just under the clearing temperature of the liquid crystal mesophase. We also found that a larger ODMS fraction, while resulting in a lower local order, resulted in a larger temperature window in which fully aligned phases can be obtained. When exposed to unpolarized light, the nanocylinders are aligned out-of-plane. Unfortunately, the out-of-plane morphology was unstable, likely due to the surface energy disparity between the molecular components. Importantly, this result highlights an important difference between BCPs and LCs; while the removal of defects is facilitated by the low glass transition temperature of the LCs, the retention of the metastable out-of-plane morphology is hampered.

Photopolymerization is a well-known method to 'freeze-in' LC order. Chapter five discloses a series of acrylate-terminated ODMS LCs which form cross-linkable lamellar phases. An added benefit of these reactive materials is the possibility for micropatterning by mask polymerization. A second method to 'lock-in' LC order is by cooling through a glass transition. In chapter six, novel hydrogen bonding ODMS LCs are prepared and subsequently mixed with a glassy hydrogen-bond accepting polymer. This approach yields a range of glassy nanoscale morphologies, in which the phase behavior can be controlled by the mixing ratio. Moreover, by mixing the LCs with a block copolymer, oriented hierarchical structures are generated. Importantly, this synergistic co-assembly can be used to realize a 'sandwich' structure in which the LC phase is oriented out-of-plane. Finally, chapter seven discusses the challenges regarding sub-5 nm patterning and discloses novel azobenzene-containing hydrogen-bonding ODMS LCs for the photoalignment of hierarchically oriented structures. By STM, we show that these materials form highly ordered hybrid organic-inorganic monolayers at the solid-liquid interface.

In summary, this thesis describes a novel class of ODMS-based liquid crystals that form ordered hybrid organic-inorganic thin film nanostructures with ultrafine

sub-5 nm dimensions, their directed self-assembly into macroscopically oriented patterns by grapho-epitaxy and photo-alignment, and retention of the patterns by covalent photo cross-linking or cooling through a glass transition.

Acknowledgements

This final part is reserved for my expression of gratitude towards the following people, all of whom have played a fundamental role in the coming together of this thesis:

To Albert Schenning: your infectious enthusiasm and seemingly limitless scientific curiosity, coupled with your laid-back managerial style, have made it a real pleasure to work with you. You've been a true role model for the last four years, and I'm afraid to say, you won't be rid of me just yet. I wish you, and your SFD, all the best as you both continue your transformation into a globally renowned, academic powerhouse.

To the SFD staff members: Dick Broer, Kees Bastiaansen, and Michael Debije, thank you for your guidance over the years. SFD is undoubtedly strengthened by your complementary expertise (and characters, you know who you are). Marjolijn, thank you for the endless support, you've continuously made my life easier. Tom, thank you for the countless orders, equipment fixes, and so on. Having you positioned within reaching distance has certainly been helpful (for me at least).

To the committee members: Dick Broer, Carlos Sanchez-Somolinos, Juriaan Huskens, Bert Meijer, Sander Wuister, and Roel Gronheid. I'm grateful to you all for taking the time to read and comment on my thesis during your summer break, and I look forward to defending my work to you. Carlos, thank you for hosting me at the University of Zaragoza for a week. Thank you, René Janssen, for chairing the PhD defense.

To Tamara Druzhinina, Claire van Lare, Sander Wuister, and Wim van der Zande from ASML: recognizing the volatility of industrial R&D, I am appreciative of the continued support during our regular update meetings. To Jan Doise and Roel Gronheid from KUL/IMEC, thank you for preparing a range of patterned wafers which were fundamental to this research. To Johan Lub, thank you for your assistance with organic synthesis. To Philippe Leclère, thank you for hosting me in Mons. Your

patience and guidance were key to visualizing the intricate structures presented in this thesis.

To all the students I had the pleasure of supervising over the years: Jari Vorstenbosch, Kyle Webb, Rik Sikkema, Daniela Hey, Rob Verpaalen, and Sjoerd Jansma. Thank you all for your contributions to this work. I enjoyed working with you and learned a lot from you, and trust that you will all go on to do great things.

To all former and current colleagues from SFD and carry-ons: Anne-Hélène, Anping, Berry, Danqing, Davey, Dirk-Jan, Ellen, Fabian, Gilles, Hao, Hitesh, Huub, Jeffrey, Jelle, Jeroen, Jody, Jurica, Laurens, Lihua, Marcos, Marina, Monali, My, Paul, Sarah, Shaji, Simon, Stijn, Ting, Tim, Tristan, Wanyu, Wei, Wilson, and Xiao, thank you for your help, discussions, and for making SFD a nice place to be.

To Esther and Sander, Dora and Matthew, Meghan and Dawid, Mariaan and Gerhard, and all the other wonderful people I've woefully forgotten, thank you for helping to make Eindhoven a happier place to be.

To my mom, Sara, and dad, Jos. Thank you for supporting me in the countless ways that you have. Even though we've consistently been separated by large distances, you've made me feel safe to be my own man and make my own mistakes. That's the greatest gift I could have been given, a gift which I hope to pass on one day. To my brothers, Jan and Toon, thank you also for your support.

To Nora and Kevin McMullan, thank you for making the English midlands feel like a home away from home. You may not realize it, but you've done your fair bit to make this thesis a reality: plenty ideas were refined on runs throughout the countryside, words were written on your coffee table, and hardships were consoled by English ales and other comforts.

To Katie. I would need a second thesis to thank you sufficiently, so here's the summary instead: Thank you for curry, beer, bacon, and cuddles. Thank you for loving me as I am, and putting up with me during the more stressful moments in this PhD, including forcing me back to bed on those sleepless nights. I'm lucky to call you my best friend.

Curriculum Vitae



Koen Nickmans was born on October 4th, 1989 in Bonheiden, Belgium. After graduating from high school in Johannesburg, South Africa (high honours), he returned to Belgium to study chemistry. He received his bachelor degree (cum laude) and master degree (magna cum laude) from the University of Louvain (KUL). During his master studies he performed an internship at Philips Research (Eindhoven), working on a topic involving nano-patterning of surfaces for lithography. Inspired by this work, he returned to Eindhoven in 2013 to join the group of Functional Organic Materials and Devices (SFD) at the Eindhoven University of Technology (TU/e) for a Ph.D. under supervision of Prof. Dr. A. P. H. J. Schenning. The most important results of his PhD research are described in this thesis. Concurrently, in 2016, Koen co-founded “Fresh Strips B.V.”, a TU/e spin-off company developing smart expiration labels, and became its Chief Technology Officer (CTO). In the first year, the company has won several business plan competitions, developed prototypes, and raised over 250.000€ in award money.

Publications related to this work

- Nickmans, K., Murphy, J. N., de Waal, B., Leclère, Ph., Doise, J., Gronheid, R., ... Schenning, A. P. H. J. (2016). Sub-5 nm Patterning by Directed Self-Assembly of Oligo(Dimethylsiloxane) Liquid Crystal Thin Films. *Advanced Materials*, 28(45), 10068–10072
- Nickmans, K., Schenning A. P. H. J. (2017). Smectic Hybrid Oligo(Dimethylsiloxane) Liquid Crystal for Nanopatterning. *Proc. SPIE 10125, Emerging Liquid Crystal Technologies XII*, 1012513
- Nickmans, K., Leclère, Ph., Lub, J., Broer, D. J., Schenning, A. P. H. J. (2017) Reactive Oligo(dimethylsiloxane) Mesogens and their Micropatterned Nanostructured Thin Films. *Soft Matter*, 13, 4357 – 4362
- Nickmans, K., Bögels, G. M., Sánchez-Somolinos, C., Murphy, J. N., Leclère, Ph., Voets, I.K., Schenning, A. P. H. J. (2017) Three-Dimensional Orientational Control

in Self-Assembled Thin Films with Sub-5 nm Features by Light. *Small*, 13, 1701043 (*cover article*)

- Nickmans, K., Schenning, A. P. H. J. Directed Self-Assembly of Liquid Crystalline Molecular Building Blocks for Sub-5 nm Nanopatterning. *Advanced Materials*. (*accepted*)
- Nickmans, K., Verpaalen, R. C. P., Murphy, J. N., Schenning, A. P. H. J. Vertically aligned, hybrid organic/inorganic sub-5 nm structured films by hydrogen-bonded oligo(dimethylsiloxane) liquid crystals and polymers. (*submitted*)
- Nickmans, K., Jansma, S. O., Hey, D., Schenning, A. P. H. J. Light-responsive hydrogen-bonded oligo(dimethylsiloxane) liquid crystals and their sub-5 nm structured monolayers. (*in preparation*)

Other Publications

- Shen, L., Nickmans, K., Severn, J. & Bastiaansen, C.W.M. (2016). Improving the Transparency of Ultra-Drawn Melt-Crystallized Polyethylenes. *ACS Applied Materials & Interfaces*, 8(27), 17549-17554

Patents

- A. J. J. Kragt, A. P. H. J. Schenning, D. J. Broer, C. W. M. Bastiaansen, K. Nickmans, M. Moirangthem, *Photonic time-temperature sensor having an embossed interpenetrating network of cholesteric liquid crystalline polymers and a secondary polymer*, PCT/EP2017/070837, Applicant Eindhoven University of Technology, Priority date filing 17-08-2016

Awards

- Best Plenary Lecture Award: Dutch Polymer Days (Mar 2017) - Lunteren
- Best Poster Award: Dutch Polymer Days (Mar 2016) - Lunteren
- Best Lecture Award: Dutch Polymer Days (Mar 2015) - Lunteren
- 1st Place: MIT Enterprise Forum Competition (Jul 2017) - Athens
- Hellenic Entrepreneurship Award (Jul 2017) - Athens
- Poster Award: RSC Emerging Tech (Jun 2017) - Manchester
- Finalist SPIE Startup Challenge (Feb 2017) - San Francisco
- 1st Place: Get in the Ring Competition (Nov 2016) - The Hague
- Merck Displaying Futures Award (Sep 2016) - Merck KGaA, Darmstadt

